Pore network analysis using X-ray microtomography

Paul-Ross Thomson

A thesis submitted in fulfillment

of the requirements for the degree of

Doctor of Philosophy

of

Royal Holloway University of London.

Department of Earth Sciences

Royal Holloway University of London

July 13, 2020

I, Paul-Ross Thomson, confirm that the work presented in this thesis is my own. Where information has been derived from other sources, I confirm that this has been indicated in the work.

Abstract

This thesis investigates the connection threshold of pore space and the bounds on permeability due to the presence of microporosity. Using X-ray microtomographic images from 18 images of natural sedimentary rocks. The pore-space network consists of junctions or pores connected via tubular throats. While numerous laboratory studies have shown that a certain minimum porosity threshold must exist to permit percolation by the establishment of a connected pore network, few studies have incorporated digital techniques to test this concept. 3D pore network models derived from X-ray microtomographic images show that with increasing porosity there is an increase in the pore radius, throat radius, throat length, and the coordination number of pores. Three distinct regimes can be identified from the data in this work. Above 10% total porosity, the connectivity of the pore network is nearly 1:1 between effective and total porosity. Between 3 and 10% total porosity, the connectivity of the pore network is diminished and partially effective. Below 3% total porosity, a porosity threshold is established, and pore connectivity is completely lost. The second aspect of this thesis explores the limit of permeability reduction by the presence of microporosity, pore space consisting of a network characterised by much smaller pore and throat radii and commonly hosted in secondary mineral phases. The upper and lower bounds on permeability are established by assigning 100% pore space and 100% solid grains to the microporosity, respectively. The results from this analysis indicate that the effective permeability of microporous rocks decrease with microporous cement in a nonlinear fashion and becomes 0 at $\sim$5% cement fraction in the lower bound. This work demonstrates the importance of digital rock physics analysis in determining reservoir quality and identifying suitability of future sites

for subsurface carbon capture and storage (CCS).

Acknowledgements

I would like to express my gratitude to Dr Saswata Hier-Majumder for his outstanding supervision. I am extremely grateful for the opportunity and privilege to have worked under his mentorship, which has been both a joy and invaluable to my personal development. Within the porous flow group, thank you to Joe and Ryan, and I wish you all the best in your own battle toward PhD completion. I would also like to thank all collaborators for their support and useful discussion throughout the PhD: Aizhan Aituar-Zhakupova, Alexander Hazel, Mark Jefferd, Brett Clark, Domenico Chiarella, Tom Mitchell, Rory Ellis and Giulio Solferino. This PhD would not have been possible without the joint funding contributions from NERC CDT in Oil and Gas and Royal Holloway so I thank them both. The CDT has been a unique experience which I will never forget. There have been a number of excellent training courses and some truly unforgettable moments shared with other members of the CDT. Many thanks to Anna Clark, Lorna Morrow and John Underhill for organizing it all. Within the department I have many to thank for their help/distraction throughout the years. Nathaniel for his guidance on early PhD life, CDT matters, and terrible dad jokes. Kayode for his unique habits and company during our numerous joint ventures on CDT courses, trips to the gym, and everything football. Alex and Chris for their interesting office conversation, and relaxing trips to Top-Golf. Luigi and Federica for their much needed coffee and trips to the pub during the final push of thesis writing. Special thanks to Kevin for his tutoring, and advice on how to lead a balanced and healthy lifestyle. Thank you to my parents, Kim and Ross, for their continued support, help and guidance. Although I rarely acknowledge it, I really do appreciate everything they have done for me throughout my life.

I would not have made it this far without them. Last but not least, a huge thank you to my Nan for providing for me and putting a roof over my head. I hope I have not been too much a handful to put up with. You might have me for a little bit longer yet...

Contents

1 Introduction **12**

2 Methodology **17**

2.1 Geological background 18

2.1.1 Berea sandstone 18

2.1.2 Fontainebleau sandstone 19

2.1.3 Doddington sandstone 19

2.1.4 Knorringfjellet sandstone 20

2.1.5 Wilcox sandstone 21

2.1.6 Estaillades limestone 21

2.1.7 Massangis Juane limestone 22

2.1.8 Savonniéres limestone 22

2.1.9 Brae Formation sandstone 23

2.1.10 Bentheimer sandstone 23

2.1.11 Gildehauser sandstone 24

2.2 Imaging porous geological media using micro CT 26

2.2.1 X-ray image acquisition 26

2.2.2 Image processing 29

2.3 Measuring rock properties 34

2.3.1 Porosity 34

2.3.2 Pore and grain geometry 37

2.3.3 Permeability 38

3 Image Segmentation and Analysis of Pore Network Geometry in Two Natural Sandstones 40

4 The Influence of Microporous Cements on the Pore Network Geometry of Natural Sedimentary Rocks 55

5 Pore Network Analysis of Brae Formation Sandstone, North Sea 71

6 Microstructural Analysis from X-ray CT Images of the Brae Formation Sandstone, North Sea 110

7 Discussion, Critical Evaluation and Future Work 122

7.1 Digital rock physics - critical evaluation of methodology 122

7.1.1 Sample selection 122

7.1.2 Image filtering 124

7.1.3 Image segmentation 125

7.1.4 Permeability simulation 127

7.2 Pore network connectivity 128

7.2.1 Implications of pore network connectivity 130

7.3 The influence of microporosity 131

7.3.1 Implications of modelling microporous material 133

8 Conclusions 135

Appendix 139

A Supplementary material for the manuscript: Pore Network Analysis of Brae Formation Sandstone, North Sea (Chapter 5) 139

Bibliography 148

List of Figures

2.1 The original core (a) with inset showing the 5 mm diameter cores used in the image acquisition. Scale-bar is 1 cm in length. The top right row from (b) to (e) shows the resultant gray scale images for samples from cored well 16/7b-20. The bottom row, from (f) to (i) shows the images from cored well 16/7b-23. Scale-bar in images (b) to (i) is 700 μm. 28

2.2 Initial steps of the image processing involve (a) sub-volume extraction, which includes the selection of a specific ROI and can help remove coning artifacts of the acquisition process shown in (b) at the top and bottom of the 2D slice. In (c), the 3D volume rendering visualisation of the extracted sub-volume is shown. 29

2.3 2D slices through one of the Brae Formation sandstone samples (Modified from Thomson et al.(2020)). In the top row (a) the data are raw and displays a significant pixelated texture with inset showing high intensity streaks around the edge of high attenuation materials. In the bottom row (b), the data has been filtered using the non-local means method. The image is smoother, high intensity streaks are reduced, and detail is maintained in a higher quality image. . . . 31

2.4 Image segmentation by gray-scale histogram evaluation. The raw slice is shown in panel (a). Panel (b) shows the histogram of image gray-scale intensity and panel (c) shows the segmentation of the pore space. The sample shown here is the Berea sandstone, where (P) is pore space, (Q) is quartz grain and (An) is the mineral ankerite. 33

2.5 3D volume rendering visualization of porosity in sample BFS1. The total porosity (ϕ_T) is shown in (a). Panel (b) shows the 3D ϕ_T with parallel planes at the top and bottom of the sample. Any voxels that do not connect to the main pore network between these two planes are removed by the axis connectivity algorithm. The isolated voxels that form ineffective pores are shown in (c). Panel (d) shows a visual comparison between effective pores in blue and the isolated pores in red. 36

7.1 The ratio between effective and total macroporosity as a function of total macroporosity. Modified from Thomson et al. (2020), showing regions of the plot that require further analysis. 123

7.2 Comparison between three segmentation techniques trialled in this study. Auto-threshold (a), Marker-based Watershed (b), and Interactive (manual) threshold (c). 125

7.3 Volume rendering visualization of effective pore network (a) and pore network model simplified geometry of effective pore network (b). 127

List of Tables

2.1 Characteristics of the data used in this research. Sample names are provided, along with rock type, image resolution and information regarding the source of the data. 27

Chapter 1

Introduction

The interconnected void space or effective porosity of rocks has a significant influence on fluid flow in reservoir rocks. These petrophysical properties have important controls on many geological processes and are vital components in a range of industrial applications, for example, geothermal energy production, groundwater engineering, hydrocarbon production, nuclear waste disposal and carbon sequestration. The analysis and understanding of pore network connectivity is of great concern to reduce uncertainties in these type of projects and to predict their behavior over time.

There are several characteristics that can effect the pore network connectivity of natural sedimentary rocks. The fundamental microstructural controls are grain size, grain packing, grain shape and the organization of grain sizes. The primary pores are those present at the time of deposition and are typically intergranular (between the grains) or intragranular (within a grain or particle). Sandstone rocks are predominantly characterized by intergranular porosity, which can remain intact even after periods of diagenesis (Paxton et al. (2002); Scholle and Ulmer-Scholle (2003)). Carbonate rocks are also known to contain primary intergranular porosity when complex fragments of bioclastic or other material are found in the matrix (Scholle and Ulmer-Scholle (2003)). Secondary porosity forms after deposition, usually as a consequence of dissolution of the primary grains or, less frequently, through dissolution of diagenetic materials such as cements and replaced grains (McBride and EF (1977); Schmidt and McDonald (1979)). Carbonate rocks are more likely to experience diagenesis and have secondary porosity due to the chem-

ical composition of their grain assemblage. Other features that can affect the pore network of natural rocks include cementation and the presence of detrital and authigenic clays (Pittman (1979)). During reactive porous flow, the precipitation of cements from solution causes deposition along and at the edge of grains, occupying valuable space within the primary pore network. While clay-rich rocks have fibrous over-growths which contain significant microporosity and can reduce the primary porosity furthermore. These features play a critical role in pore network connectivity and the establishment of a percolation threshold (a connected regime of through-going paths). With consideration for intergranular porosity (macroporosity), cementation and the presence of microporosity, this thesis aims to provide a better understanding of porosity thresholds in natural sedimentary rocks.

Several empirical studies have shown that a certain minimum porosity threshold must exist before percolation is possible and an effective pore network is established (Gomez et al. (2010); Mavko and Nur (1997); Revil et al. (2014)). The Kozeny-Carman relation of the form $k = k_0\phi^n$, is commonly used to express the relationship between porosity, ϕ, and permeability, k. The empirical study on permeability of clean Fontainebleau sandstones by Bourbié and Zinszner (1985) demonstrated that the Kozeny-Carman model stops working in samples with low porosity ($< 9\%$). Their results indicate that the porosity exponent, n, in the Kozeny-Carman relation varies between 3 and 7, with samples that have high porosity and low porosity, respectively. Introducing a percolation threshold, ϕ_p, Mavko and Nur (1997) modified the Kozeny-Carman equation to $k = k_0(\phi - \phi_p)^n$. Using $\phi_p = 2.5\%$, their model provided a uniform value of $n = 3$ for the entire range of porosities. Later experimental determinations of permeability by Gomez et al. (2010) and Revil et al. (2014) showed that the percolation threshold, ϕ_p, varied between 2.0 and 2.5% based on a fit from the experimental data. The coincident determination of total and effective porosity, and permeability in natural sedimentary rocks allows us to understand the role of pore network connectivity on permeability directly. Although there have been various empirical studies of porosity and permeability, there are relatively few studies that incorporate 3D images of the pore volumes in natural

reservoir rocks.

The work in this thesis aims to bridge the gap between empirical studies of pore connectivity in relatively clean sedimentary rocks and pore network modelling using high resolution X-ray microtomographic images from a variety of natural sedimentary rocks, including the Brae Formation sandstone, from which digital techniques have not previously been tested. In total, 18 sets of images from different sedimentary rock samples are used in the digital analysis. Using 3D pore network models derived from the segmented pore phase of the images, this thesis explores the relationship between increasing porosity and pore geometry, in terms of pore radius, throat radius, throat length, and coordination number (the number of throats attached to individual pores). The second part of this thesis tests the influence of microporosity on pore network connectivity. With the establishment of the upper and lower bounds on permeability, the influence of microporosity can be determined using models that assume 100% pore space and 100% solid respectively. This work aims to demonstrate the significance of digital rock physics techniques in the determination of reservoir quality in potential carbon capture and storage (CCS) subsurface reservoirs.

The objectives of this thesis can be summarized by the following questions:

1. Through reconstruction of 2D X-ray microtomographic images, can 3D models help provide a better understanding of pore network connectivity in natural rocks with varying porosity?

2. Using 3D pore network models is it possible to identify a porosity/percolation threshold across a range of different rock samples?

3. What is the influence of sub-resolution microporosity on pore network connectivity and its ability to permit flow?

This thesis is formed using the alternative format. Some chapters are included as published manuscripts, while others are at different stages in the publication process.

The thesis has the following structure:

Chapter 2 – Methodology. This chapter describes the general methodology used in this work. To avoid repetition, sometimes there is reference to the specific methodology section of manuscripts, particularly when techniques unique to that work are used.

Chapter 3 – Image Segmentation and Analysis of Pore Network Geometry in Two Natural Sandstones (published in Solid Earth Geophysics, a section of the journal Frontiers in Earth Science). This paper compares the pore network connectivity and geometry of two natural sandstones with quite different porosity.

Chapter 4 – The Influence of Microporous Cements on the Pore Network Geometry of Natural Sedimentary Rocks (published in Earth and Planetary Materials, a section of the journal Frontiers in Earth Science). This paper investigates the influence of the microporosity on the pore network of 3 sandstone and 3 limestone samples.

Chapter 5 – Pore Network Analysis of Brae Formation Sandstone, North Sea (second stage of review – submitted to the journal Marine and Petroleum Geology). This paper investigates the pore network connectivity in a set of samples from the Brae Formation sandstone.

Chapter 6 – Microstructural Analysis from X-ray CT Images of the Brae Formation Sandstone, North Sea (published in Earth and Planetary Materials, a section of the journal Frontiers in Earth Science). This paper investigates the influence of the lower bounds of a microporous cement phase on pore network connectivity and permeability.

Chapter 7 – Discussion, Critical Evaluation and Future Work

Chapter 8 – Conclusions

Chapter 2

Methodology

Understanding the role of pore connectivity during porous flow is a difficult problem that requires the three-dimensional (3D) characterization of the pore space. Rocks containing pore space often have a complex microstructure, which can vary at multiple scales, from centimetres to nanometres, introducing a very heterogeneous character. As a result of this complexity and range in scales, the characterization of porous rocks using X-ray computed microtomography (micro CT) is necessary for our understanding of pore scales processes that can not typically be achieved from core experiments and reservoir scale measurements.

The aims of this research focus on the micro scale connectivity of the pore space in a range of different sedimentary rocks. It is duly noted that the methods incorporated in this work can not clarify nor represent the uncertainties that are associated with reservoir scale heterogeneity using a small number of samples of a particular rock type. While it is an interesting challenge, the upscaling from pore to reservoir remains out of scope within this thesis. Potential methods of upscaling have been proposed in the past. The interested reader is referred to articles by Rhodes et al. (2008) and Blunt et al. (2013) who suggest an integrated approach including core scale bench-marking, metre scale transport simulation and finally reservoir scale simulation.

2.1 Geological background

This section provides a brief background to the different carbonate and sandstone samples used in this work. A sedimentological overview and the characteristics of the formations are described for each. Each section also explains why each sample was chosen in this research. The overall aim of sample selection was to achieve a range of porosities across all samples. Ultimately however, this was limited and dependent on the generosity of other authors, enabling open accessibility to their samples. The process of sample preparation and image acquisition remains a fairly time consuming and expensive outlay which limited the number of samples available for use in this thesis.

2.1.1 Berea sandstone

The Berea sandstone, named accordingly from its first major quarry town (now city) of Berea, Ohio in the United States. It outcrops along much of the state and has been extensively quarried for over 200 years. In addition to its use in building thousands of commercial, residential and governmental structures (Hannibal, 2020), as a reservoir rock it has been an important oil and gas play in the state of Kentucky for many decades. Furthermore, the Berea sandstone is one of the most studied sandstones in the world, where it has long been a standard for petroleum related investigations (Churcher et al., 1991; Øren and Bakke, 2003; Valvatne and Blunt, 2004).

The Berea sandstone belongs to the stratigraphic formation named Berea Sandstone. This formation occurs in the Appalachian Basin, a large wedge-shaped Paleozoic basin to the west of the Appalachian Mountains. The rocks were deposited during the Late Devonian transition into the Carboniferous, approximately 359 Ma (Hannibal, 2020). The Berea sandstone is a generally well sorted quartz arenite to sublitharenite, deposited in a fluvial deltaic environment (Ells and Division, 1979).

The Berea sandstone sample used in this work was acquired from the Berea SandstoneTM Petroleum Cores (Ohio, USA) (Madonna et al., 2013). The synchrotron images were acquired at the TOMCAT (TOmographic Microscopy and Coherent rAdiology experimenTs; Stampanoni et al. (2006)) beam-line at the Swiss

Light Source (SLS; Paul Scherrer Institute, Villigen, Switzerland). This sample was chosen because it is a benchmark sample from which we could establish our model and assess the results with those from the literature. In addition to this, the images are very high resolution and openly available for use.

2.1.2 Fontainebleau sandstone

The Fontainebleau sandstone occurs within the central part of the Paris Basin, south of Paris. It is buried to relatively shallow depths ($<$ 100 m) and in some places not greater than a few tens of metres, meaning it is easily quarried. It is considered to be one of the more simplistic forms of porous geological media with a constant and regular pore and grain framework. As such, it is a benchmark sample which has been used in a number of experimental and original digital rock studies (Bourbié and Zinszner, 1985; Doyen, 1988; Fredrich et al., 1993; Lindquist et al., 2000).

The Fontainebleau sandstone was deposited during the early Oligocene, around 27–36 Ma. It is a fine grained, well sorted, quartz arenite which is interpreted as a marine shoreface deposit, overlain by subaerial aeolian dune-bedded sands (Alimen, 1936). It has also been recognised that the Fontainebleau sandstone has a variety of porosity and permeability (Bourbié and Zinszner, 1985).

The Fontainebleau sandstone sample images used in this research were acquired at the TOMCAT (TOmographic Microscopy and Coherent rAdiology experimenTs; Stampanoni et al. (2006)) beam-line at the Swiss Light Source (SLS; Paul Scherrer Institute, Villigen, Switzerland) (Madonna et al., 2013). This particular sample was chosen because it has a low porosity, which permitted the pore network analysis and comparison between two quite different sandstones (Chapter 3).

2.1.3 Doddington sandstone

The Doddington sandstone presumably obtains its name from the village Doddington in Northumberland, UK, near to which it is quarried. More generally, the Doddington sandstone belongs to the Fell Sandstone Group. This group was deposited during the Lower Carboniferous (Visean), approximately 346.7 Ma. The sandstone deposits form part of a fluvial deltaic sequence found within the Northumberland

Basin and the smaller Tweed Basin. Generally, the sandstones are medium grained, mature and well sorted quartz arenites or sub-litharenites (Turner et al., 1993). The Doddington sandstone is mostly composed of quartz (95% silica by weight) with some minor micas and feldspars (Santarelli and Brown, 1989).

The Doddington sandstone images were initially acquired as part of the study by Shah et al. (2016). The Doddington sandstone has also been used in other research, which include studies by Andrew et al. (2014); Alyafei and Blunt (2016); Alhashmi et al. (2016). The set of Doddington sandstone sample images from Shah et al. (2016) was used in this research because it represents a sandstone that has a high proportion of effective porosity (23%) (Santarelli and Brown, 1989). It adds to the 3D pore network analysis of sandstones which possess a range of porosities. The Doddington sandstone images were obtained from the BGS website, which are openly available for use.

2.1.4 Knorringfjellet sandstone

This sample is a tight sandstone from the Knorringfjellet Formation on Spitsbergen, Svalbard. The Knorringfjellet Formation can generally be divided into two members, both of which consist of mudstones and sandstones in varying proportions (Rismyhr et al., 2019). The subdivision occurs due to the presence of a major unconformity (Mørk et al., 1999), separating the lower Tverrbekken member (Late Triassic) and the overlying Teistberget member (Early Jurassic). Forming part of the Wilhelmoya Subgroup, the Knorringfjellet Formation is a concentrated section of textually mature sandstones, deposited on coastal plains and in deltaic to shallow marine environments (Van Stappen et al., 2014).

It is of particular interest because it has been under consideration as a possible CO_2 storage reservoir (Van Stappen et al., 2014). In addition to this, and in relation to this work, the Knorringfjellet sandstone sample has a relatively low porosity (approximately 7.5%) and secondary (micro) porosity associated with illite clay (Bultreys et al., 2016b). The Knorringfjellet sandstone sample images are available upon request from the authors (Bultreys et al., 2016b).

2.1.5 Wilcox sandstone

The Wilcox sandstone sample belongs to the Wilcox Formation. This particular sample is considered an unconvertional tight gas sandstone reservoir rock. The Wilcox Formation is Paleogene in age and was deposited in a fluvial-deltaic environment (Dutton and Loucks, 2010). The Wilcox sandstone sample is a plagioclase arkose with low proportions of macroporosity and slightly higher proportions of microporosity. Thin section analysis by Mehmani et al. (2015) indicated that the rock had primary porosity of 2.8% and secondary porosity of 3.1% present as microporous clay clasts and dissolved feldspars.

The Wilcox sandstone sample images are easily accessed from the Digital Rocks Portal, a repository for porous media images. This particular sandstone was of interest in this work because of its low macroporosity and high secondary porosity content.

2.1.6 Estaillades limestone

The Estaillades limestone is a natural analog for a carbonate reservoir. The samples are obtained from the Oppéde quarry in the south of France and have been extensively studied as a benchmark rock for pore scale modelling of carbonates with a bimodal pore size distribution (Youssef et al., 2008; Bauer et al., 2012; Blunt et al., 2013; Bultreys et al., 2015). The Estaillades limestone is a monomineralic, calcitic grainstone. It has a porosity around 25% with intragranular micropores present in fossil grains (Youssef et al., 2008).

Since the Estaillades limestone is well established in studies involving geological porous media, the images are available from a number of sources. The images used in this study were obtained directly from Tom Bultreys (Bultreys et al., 2015, 2016b), however they are also available online from the Digital Rocks Portal. The Estaillades sample was chosen in this work because the image data are readily available and display characteristics of both macroporosity and microporosity.

2.1.7 Massangis Juane limestone

The Massangis Juane variety of the Massangis limestone is also quarried in France, from the Massangis commune in the North-Central region. It is Middle Jurassic in age and is an ooid-dominated grainstone containing fragments of micrite and bioclastic material (De Muynck et al., 2011). The porosity within the bulk of this rock is quite varied, with some random zones of significant microstructure and lower porosity (Boone et al., 2014). Interparticular moldic macropores exist as a result of dedolomitization and this can influence whether or not the macropores permit fluid flow (Bultreys et al., 2016b). Regions of partially dissolved dolomite which line mold and local ooids contain microporosity.

The Massangis limestone sample was chosen in this research because it forms an analog to carbonate reservoirs with variable quantities of both macro and microporosity. Similarly to other samples, the Massangis is also readily available and can be downloaded from the Digital Rocks Portal.

2.1.8 Savonniéres limestone

The Savonniéres limestone is another quarried example from France and forms an analog carbonate reservoir. It is Upper Jurassic in age and is characterized as a monomineralic, layered, oolithic grainstone which displays a range of porosity between 22% and 40% (De Muynck et al., 2011; Derluyn et al., 2014). It has a range of porosity types which include: intergranular and microconnected macroporosity (unfilled ooids), partnered by intergranular, and intraooidic microporosity (Bultreys et al., 2016b). Empty ooids are only connected to other macropores by microporosity in the ooid shells (Roels et al., 2001).

Similarly to the other limestone samples the Savonniéres was chosen because of its diverse pore structure, with a range in examples of both micro and macroporosity. Furthermore, the images are readily available and can be downloaded from the Digital Rocks Portal.

2.1.9 Brae Formation sandstone

The Brae Formation sandstone samples in this work originate from the United Kingdom Continental Shelf (UKCS) Miller Field. This is a former producing oil field located along the western margin of the South Viking Graben. The sandstone reservoir rocks of the Brae Formation are composed of Late Jurassic submarine fan deposits which were derived from the Fladen Ground Spur (Devonian basement) to the west of the north-south orientated half-graben (Rooksby, 1991; Gluyas et al., 2000). The Brae Formation sandstone is characterised as a homogeneous, quartzose sandstone (Gluyas and Coleman, 1992). The sandstones are cemented by quartz with some minor amounts of calcite and clay minerals (Garland, 1993). Parts of the Brae Formation sandstone remain completely free of quartz cement due to the fact that they lie within calcite concretions which precipitated soon after deposition of the sand, and preserve the natural fabric (Gluyas et al., 2000).

The Brae Formation sandstone samples were chosen in this study because they are the reservoir rocks of the Miller field, which is an ideal analog for the long-term fate of CO_2 during engineered storage (Lu et al., 2011). It is important to improve our understanding of pore network connectivity and how this can affect fluid flow during such projects. The sandstones are reported to have an average porosity in the range 13-17%, with upper parts of the reservoir having higher porosities between 18-22% (Garland, 1993). This range in porosities makes these rocks a good candidate to assess the variation of pore network connectivity with porosity. In addition to this, the cored sandstone intervals from wells 16/7b-20 and 16/7b-23 are readily available at the Royal Holloway University of London rock store. Four sandstone samples were selected from each well at varying depth intervals. The samples were selected based on visual inspection, targeting zones of clean sandstone. Further details of the sample preparation is outlined in section 2.2.1.2.

2.1.10 Bentheimer sandstone

The Bentheimer sandstone is one of the two varieties of the Bentheim Sandstone. The Bentheim Sandstone outcrops as a ridge roughly 9 km in length and 400 m in width, between Gildehaus and Suddendorf in Germany close to the border with

the Netherlands (Dubelaar and Nijland, 2016). The Bentheimer example is characterised by its darker appearance and occurrence to the east of Bad Bentheim. Like many of the other samples used in this work, it has been quarried for many years. The sandstone is Lower Cretaceous in age and was deposited in a shallow marine environment in the western region of the Lower Saxony Basin. It forms the reservoir rock of several oil and gas fields in northwest Germany and northeastern Netherlands (Füchtbauer, 1963; De Jager and Geluk, 2007; Dubelaar and Nijland, 2015).

The characteristics of the Bentheimer sandstone have been studied in great detail for a number of years (Bakke et al., 1997; Bultreys et al., 2013; Peksa et al., 2015; Gao et al., 2017). For this reason, the sample images are readily available and easily accessible. The images in this work were obtained from (Gao et al., 2017). The Bentheimer sandstone is also characterized by a very high quartz composition (usually greater than 90%, sometimes as high as 97%), and relatively low proportions of feldspars and clay material. As a result, porosity values are usually in excess of 20% (Peksa et al., 2015), which makes the Bentheimer sample an ideal candidate for pore network connectivity analysis at the higher end of the porosity spectrum.

2.1.11 Gildehauser sandstone

The Gildehauser sandstone is the other variety of the Bentheim Sandstone. The Gildehauser sandstone gets its name from the town of Gildehaus, near to where it is quarried. This particular variety of the Bentheim Sandstone is similar to the Bentheimer sandstone but appears more of an 'off-white' cream colour which makes it more popular for use as a building stone (Dubelaar and Nijland, 2015). The Gilderhauser sandstone forms part of the Bentheim Sandstone, deposited during the Lower Cretaceous in a shallow marine environment. Much like the Bentheimer sandstone variety, it has an average porosity of 20% with low clay content and a narrow pore distribution (Berg et al., 2016).

The Gildehauser sandstone sample was chosen in this work because of its clean character and relatively high porosity. It is an ideal sample for the analysis of pore

network connectivity in rocks with good porosity. It has also been a popular sample for studies in the past (Berg et al., 2016; Rücker et al., 2015; Alpak et al., 2018), which means that the sandstone images have been made more accessible for other researchers. The images used in this work were downloaded from the Digital Rocks Portal.

2.2 Imaging porous geological media using micro CT

The last two decades has seen a great rise in the popularity of micro CT providing a new method to analyze a variety of research problems in many different fields of geoscience research. Micro CT provides 3D visualization and internal structural information of geologic materials without damaging or invading the material under consideration. The technique is based on the attenuation of X-rays as they move through the geologic sample. As the sample is positioned and rotated between a source and detector, an array of information is collected at the detector following the penetration of the material. The intensity of the X-rays reaching the detector are controlled by samples thickness, composition and density. This data are converted and transformed into a stack of 2D images with a range of gray scale intensity values. The 2D images are combined and transformed to produce 3D volumes for analysis. For more detailed information on the micro CT technique and its use in geoscience research, the reader is referred to the excellent review papers by Cnudde and Boone (2013); Ketcham and Carlson (2001); Wildenschild and Sheppard (2013); Bultreys et al. (2016a).

2.2.1 X-ray image acquisition

2.2.1.1 Data

The data used in parts of this research was sourced externally. Table 2.1 summarizes the sample name, rock type, image resolution and source of data used in this research. In Chapter 3, this includes very high resolution images of the Berea and Fontainebleau sandstones acquired at the TOMCAT (TOmographic Microscopy and Coherent rAdiology experimenTs; Stampanoni et al. (2006)) beam-line at the Swiss Light Source (SLS; Paul Scherrer Institute, Villigen, Switzerland). For more information on these samples, the reader is referred to Madonna et al. (2013). In Chapter 4, this includes images of the Doddington, Knorringfjellet and Wilcox sandstones, and the Estaillades, Massangis Jaune and Savonniéres carbonate samples. Further information on these six samples can be found from Shah et al. (2016); Mehmani and Prodanović (2014); Prodanović et al. (2014); Bultreys et al. (2016b);

Sample name	Rock type	Image resolution (voxel size)	Data source
Berea	Sandstone	$(0.7\ \mu\text{m})^3$	Madonna et al. (2013)
Fontainebleau	Sandstone	$(0.7\ \mu\text{m})^3$	Madonna et al. (2013)
Doddington	Sandstone	$(6.4\ \mu\text{m})^3$	Bultreys et al. (2016b)
Knorringfjellet	Sandstone	$(2.8\ \mu\text{m})^3$	Bultreys et al. (2016b)
Wilcox	Sandstone	$(2.7\ \mu\text{m})^3$	Bultreys et al. (2016b)
Estaillades	Limestone	$(3.1\ \mu\text{m})^3$	Bultreys et al. (2016b)
Massangis Jaune	Limestone	$(4.5\ \mu\text{m})^3$	Bultreys et al. (2016b)
Savonniéres	Limestone	$(3.8\ \mu\text{m})^3$	Bultreys et al. (2016b)
BFS1	Sandstone	$(3.9\ \mu\text{m})^3$	Thomson et al. (2020)
BFS2	Sandstone	$(3.9\ \mu\text{m})^3$	Thomson et al. (2020)
BFS3	Sandstone	$(2.0\ \mu\text{m})^3$	Thomson et al. (2020)
BFS4	Sandstone	$(2.0\ \mu\text{m})^3$	Thomson et al. (2020)
BFS5	Sandstone	$(2.0\ \mu\text{m})^3$	Thomson et al. (2020)
BFS6	Sandstone	$(3.9\ \mu\text{m})^3$	Thomson et al. (2020)
BFS7	Sandstone	$(2.0\ \mu\text{m})^3$	Thomson et al. (2020)
BFS8	Sandstone	$(3.9\ \mu\text{m})^3$	Thomson et al. (2020)
Bentheimer	Sandstone	$(6.0\ \mu\text{m})^3$	Gao et al. (2017)
Gildehauser	Sandstone	$(4.4\ \mu\text{m})^3$	Rücker et al. (2015)

Table 2.1: Characteristics of the data used in this research. Sample names are provided, along with rock type, image resolution and information regarding the source of the data.

Boone et al. (2014). In Chapters 5 and 6, the micro CT images of the Brae Formation sandstone are unique and were acquired as part of this research (see below). Two additional samples were used in Chapter 6. These include the Bentheimer and Gildehauser sandstone. More information on these samples can be found in work by Rücker et al. (2015); Berg et al. (2016) and Gao et al. (2017).

2.2.1.2 Sample preparation

Prior to image acquisition, eight 5 mm diameter cores of the Brae Formation sandstone were drilled and/or ground from sections of original 15 cm core (Figure 2.1(a)) of two North Sea wells (16/7b-20 and 16/7b-23) originating from the Miller oil field. Four 5 mm diameter cores were taken from each cored well, collected between an interval of $\sim$5 m and $\sim$4 m in well 16/7b-20 and 16/7b-23, respectively.

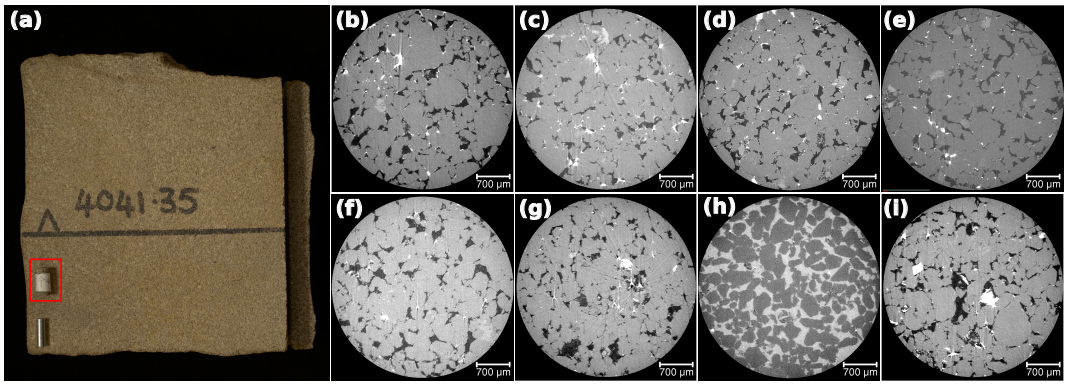

Figure 2.1: The original core (a) with inset showing the 5 mm diameter cores used in the image acquisition. Scale-bar is 1 cm in length. The top right row from (b) to (e) shows the resultant gray scale images for samples from cored well 16/7b-20. The bottom row, from (f) to (i) shows the images from cored well 16/7b-23. Scale-bar in images (b) to (i) is 700 μm.

Using a straw tube holder, the samples were stacked and separated by small foam buffers to allow clear identification of each sample. The stack of samples were loaded into the scanner and positioned between the source and detector. A preliminary scan of each sample was completed to assess and record the best parameters for high quality images.

2.2.1.3 Image scanning

The complete stack of 5 mm diameter core samples were scanned on a Zeiss Xradia Versa 520 scanner at the Imaging and Analysis Centre at The London Natural History Museum. A voltage between 80 and 100 kV was used to optimize the X-ray transmission. This voltage was varied, depending on the rock type - its composition and grain size. Samples that required a higher voltage were processed with a camera binning of 2×2 in order to increase the signal to noise ratio and improve overall image contrast. To minimize the reconstruction artifacts a full 360 degree rotation was used to collect 3201 projections for each scan. The image resolution was varied between 2 μm^3 voxels and 3.9 μm^3 voxels, with two samples of each resolution acquired from each cored well (16/7b-20 and 16/7b-23). Figure 2.1(b) to (e) and (f) to (i) shows examples of the 2D slices obtained from the image scanning in samples from cored well 16/7b-20 and 16/7b-23, respectively. Detailed information on the image acquisition is outlined in the methodology section of Chapter 5.

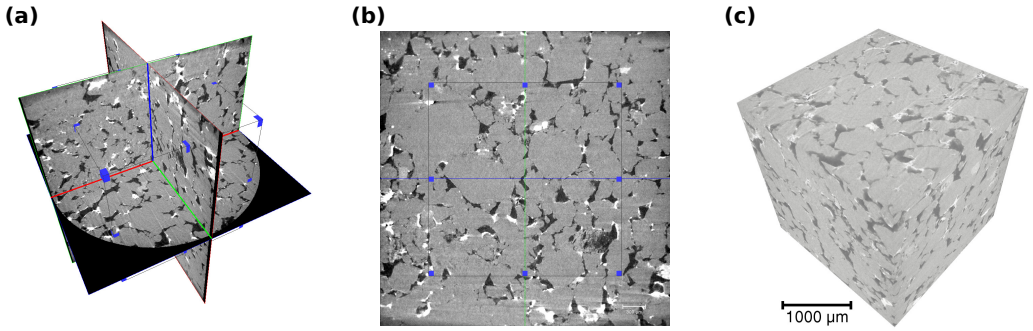

Figure 2.2: Initial steps of the image processing involve (a) sub-volume extraction, which includes the selection of a specific ROI and can help remove coning artifacts of the acquisition process shown in (b) at the top and bottom of the 2D slice. In (c), the 3D volume rendering visualisation of the extracted sub-volume is shown.

2.2.2 Image processing

The image processing and analysis was performed using the software PerGeos - from Thermo Fisher Scientific. Image processing is necessary because there are a number of different image artifacts frequently encountered due to the imperfections of the image acquisition process (Ketcham and Carlson, 2001; Wildenschild et al., 2002). The most common examples of image noise are due to the low count of X-rays received at the detector, image blur caused by movement, hardware restrictions, or poor quality image reconstruction (Schlter et al., 2014). Some samples in this study have shown evidence of ring artifacts and beam hardening, displaying streaks around high attenuation materials and intensity variation between the edge and middle of the sample. Most commonly, the raw images had a speckled pixelated texture that was more easily filtered. Somewhat thankfully, none of these impairments caused the significant loss of detail in the analyzed images.

The image segmentation also plays a key role in image analysis, as this determines the accuracy and reliability of subsequent results. There are two key types of image segmentation, global thresholding and local segmentation. These two categories are briefly outlined in the following sections. While a small number of methods are compared in this work, the detailed review of numerous segmentation techniques does not form a part of this research. If the reader is interested in different image segmentation methods and would like a detailed overview, they are

referred to papers by Iassonov et al. (2009) and Schlter et al. (2014).

The following sections primarily describe the image filtering, segmentation and pore/grain separation techniques specific to this research.

2.2.2.1 Image filtering

The first step of image filtering is the extraction of a sub-volume (Figure 2.2(a)). During this process the raw stack of images are reduced in volume to generate a new volume or region of interest (ROI). This extraction can also act as a first stage effort to increase image quality. As Figure 2.2(b) shows, there is often a coning effect at the top and bottom of the sample where low intensity voxels are prominent. These areas can create problems during image segmentation so are effectively removed by the new ROI. Figure 2.2(c) shows a 3D volume rendered image of the selected ROI with consistent gray scale values. The macropores are represented by the darkest gray or black voxels, while the lighter shades of gray and white belong to quartz grains and other higher density materials, respectively.

In this work, the non-local means filter was the filter of choice to enhance image quality and maintain detail of the microstructure in all samples. Where other less common methods of filtering have been used, these are outlined in more detail in the relevant chapter. For example, in Chapter 3 additional filtering was used to help reduce the impact of high phase-contrast fringes found at the edge of grains. To avoid excessive unnecessary repetition, this section will not cover all filtering techniques but focuses on the non-local means filter.

The non-local means filter is extremely effective for noisy images. The filter is capable of running in 3D but this dramatically increases the processing time. In this work, the images were processed in 2D to avoid needless computation. The algorithm behind the filter deploys a search window, which can be manually varied to increase or decrease the search area of voxels. Naturally, the larger the search area, the better the results usually are. However, this again comes at a consequence of greater processing time. A search window of 21 voxels diameter was used, as recommended within the PerGeos user instructions. Finally, the algorithm compares the neighbors of all voxels in the search window with the current voxel and

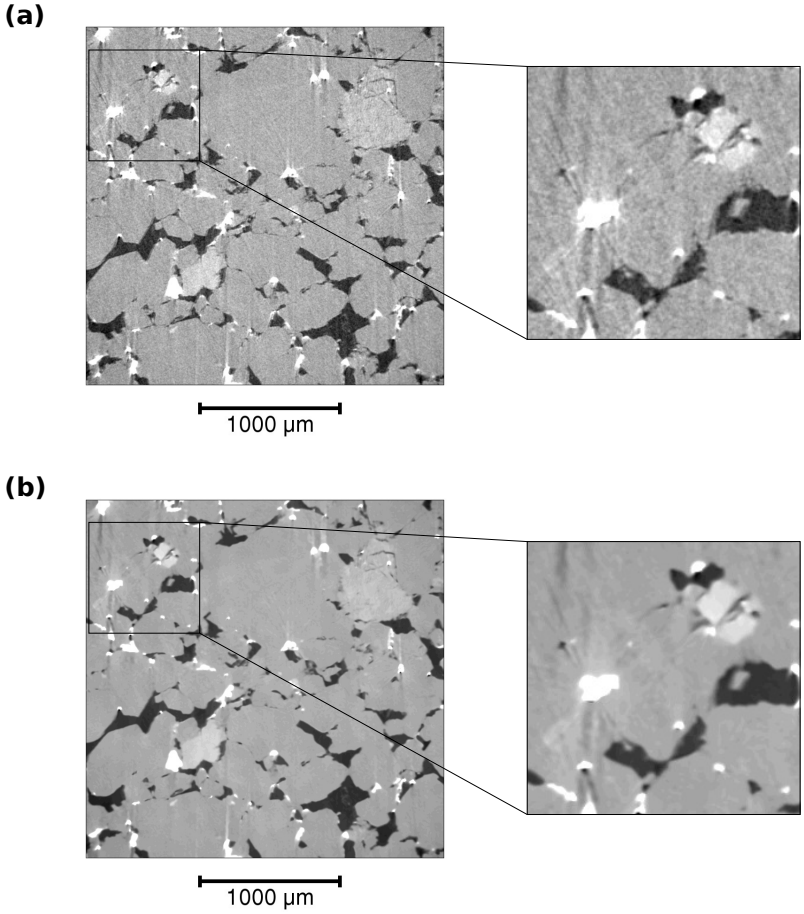

Figure 2.3: 2D slices through one of the Brae Formation sandstone samples (Modified from Thomson et al.(2020)). In the top row (a) the data are raw and displays a significant pixelated texture with inset showing high intensity streaks around the edge of high attenuation materials. In the bottom row (b), the data has been filtered using the non-local means method. The image is smoother, high intensity streaks are reduced, and detail is maintained in a higher quality image.

the similarity between those neighbors determines the weight with which the value of those voxels influence the new value of the current voxel. Figure 2.3(a) shows a 2D slice of the raw gray scale image from a sample of the Brae Formation sandstone. In this image, the affects of beam hardening are evident as streaks around the high intensity white material. Additionally, the center of grains and pores have a speckled appearance which can affect the image segmentation process. Figure 2.3(b) highlights the results of the non-local means filter on this same 2D slice. As the inset highlights, the streaks are reduced and the grains and pores have a much improved smooth texture. Importantly, no detail of the microstructure is removed

during the filtering process.

For more information specific to the non-local means filter, the reader is referred to papers by Buades et al. (2005, 2008). A good overview of the non-local means and other image filtering techniques are also provided by Schlter et al. (2014).

2.2.2.2 Image segmentation

The process of image segmentation is an important step in any image analysis work. It is crucial to separate the pore phase accurately so that a true representation of the rock is achieved and subsequent analysis is reliable.

There are a variety of image segmentation techniques, which can broadly be separated into two key groups: global thresholding and locally adaptive thresholding. Global thresholding is the most popular method for image segmentation, based on the approach where voxels within a specific gray-scale interval are assigned to labels by histogram evaluation. The limitation of this approach is the lack of consideration for how gray values are spatially arranged within the volume of interest, particularly when voxels of a certain material phase have gray-scale value that do not fall in the same histogram range. Despite this limitation, manual thresholding is still one of the most commonly performed methods.

In contrast to global thresholding, locally adaptive segmentation methods take some account for neighborhood gray-scale assignment. These techniques have been known to produce smooth object boundaries, avoid noise or consider local intensity changes (Schlter et al., 2014). Local segmentation techniques can result in more satisfying results (Iassonov et al., 2009). However, review papers from Sezgin and Sankur (2004) and Iassonov et al. (2009) have also shown that of the many automatic techniques in existence, it is often still necessary to provide manual assistance during the segmentation process. When high quality images, displaying good contrast are used, the user controlling the segmentation process can generate excellent data, and reliable results (Bultreys et al., 2016a).

In this work, the interactive (manual) threshold segmentation technique was the primary method used to separate the individual material phases within the im-

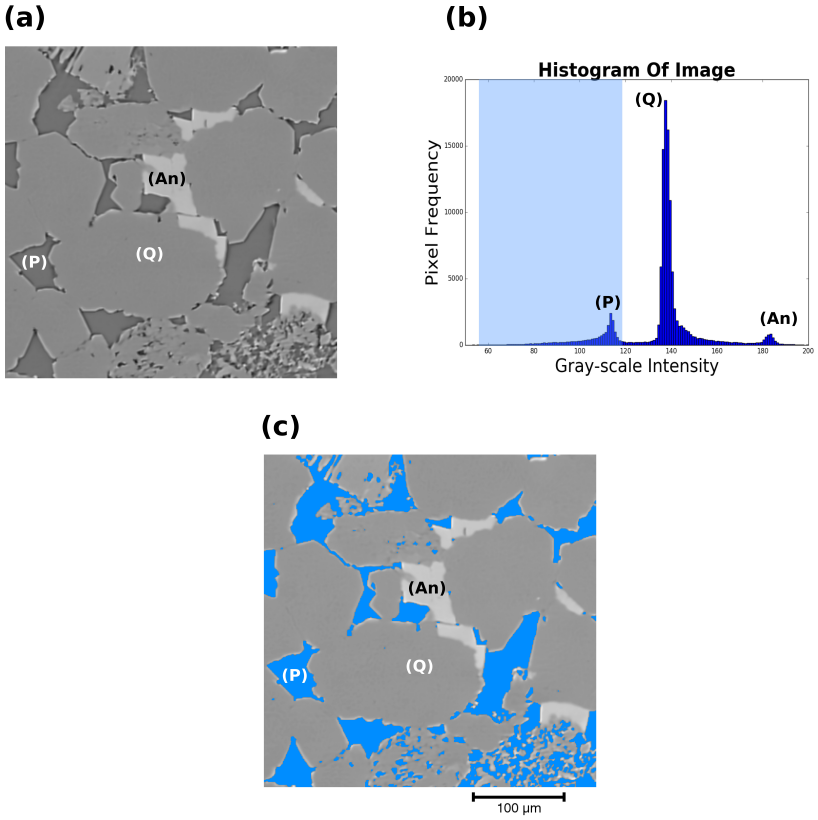

Figure 2.4: Image segmentation by gray-scale histogram evaluation. The raw slice is shown in panel (a). Panel (b) shows the histogram of image gray-scale intensity and panel (c) shows the segmentation of the pore space. The sample shown here is the Berea sandstone, where (P) is pore space, (Q) is quartz grain and (An) is the mineral ankerite.

ages. This method allowed thresholds to be selected manually based on their specific gray-scale intensity. Figure 2.4(a) shows a 2D slice of the Berea sandstone sample with three key materials: (P) is pore space, (Q) is quartz grain and (An) is the mineral ankerite. The properties of the material phase effect the gray-scale intensity, which is a direct consequence of X-ray attenuation. Materials that are more easily penetrated by X-rays have a low attenuation, while materials that have high attenuation only allow a relatively short distance of penetration. At the darker end of the spectrum (values closer to 0), the pore space (P) has less attenuation to the X-ray beam, resulting in the first peak shown within the image histogram in Figure 2.4(b). The quartz grains (Q) are more abundant in the sample and have more attenuation to the X-ray beam, displaying a much larger peak in the histogram and higher gray-scale intensity, respectively. The mineral ankerite (An) is the least prominent

material in the sample which is shown by a small peak in the histogram. Ankerite (An) does however have the highest gray-scale intensity (high X-ray attenuation), shown by the histogram peak location close to the far right end of the spectrum. The histogram in Figure 2.4(b) also shows a blue shaded region that approximately equates to the pixels that are representative of the pore space (P) phase. Assigning the pixels in this region to one label allows the segmentation of the pore space (P) phase. The results of this segmentation for this particular 2D slice are shown in Figure 2.4(c). This technique produced acceptable results within all data used in this work. Where additional segmentation was required, this is outlined in the relevant chapter. See for example, Chapter 3, section 2.1 and Figure 4 within for more information on the necessary image processing procedures in these particular samples.

2.3 Measuring rock properties

The rock properties are measured directly using the 3D images acquired as a result of the image processing and segmentation stage. In the following sections, information is provided that outlines the processes involved in the identification and measurement of porosity, measurement of pore and grain geometries, and simulation of absolute permeability.

2.3.1 Porosity

Primary porosity is porosity that is preserved during deposition of the original sediment. This usually exists as interparticle pores, forming a macro network between the grains. Though the identification and analysis of macropores is relatively straightforward, the resolution of micro CT limits the analysis of micropores, which can form secondary porosity as a consequence of mechanical deformation and/or geochemical processes. Nevertheless, it was possible to separate the pore space into macropores and more crudely, the micropores. Depending on the nature of the rock type (e.g. clean sandstones, tight sandstones, and carbonates) microporosity was present in various forms. In Chapter 4 the carbonate samples display intraparticle microporosity, where bioclastic and/or grain material is thought to have been

partially dissolved. The tight sandstones in Chapter 4 also seem to contain higher proportions of microporosity, which may be linked to their texture (e.g. grain size and sorting) and depositional history. The cleaner sandstones like the Doddington and Brae Formation sandstones used in Chapter 4 and Chapters 5 and 6, respectively, display evidence of microporosity in the form of cementation and detrital and/or authigenic clays found along pore and throat contacts.

While the accurate quantification of microporosity is not possible at the resolution of the images used in micro CT analysis, simplified pore network models can provide some insights into the influence of microporous material and pore space connectivity. To incorporate the micropores into 3D micro CT analysis it was possible to create simple models which allowed the evaluation of the influence of micropores on reservoir quality. One approach is to consider the microporous phase as completely void, therefore meaning that it is completely permeable, forming part of the macropore network and contributes to fluid flow through the entire sample. The alternative approach is to consider the opposite, that microporosity is completely impermeable. Using these scenarios, two end-member models are generated to better understand pore network connectivity. The first approach was used to create a pore network model assuming pore space before cementation and the second to model pore network connectivity following cementation.

Using the stack of 2D binary slices produced as an outcome of the image segmentation (as described in Section 2.2.2.2), the pore volumes are calculated. The pore spaces are assigned to either total porosity (ϕ_T), or separated into macro and microporosity, (ϕ_M) and (ϕ_m), respectively. To calculate the volume fraction of total porosity (ϕ_T), the 2D slices representative of total porosity are reconstructed to form a 3D volume (Figure 2.5(a)). The combined number of voxels in the 3D total porosity volume (Tp_v) are divided by the total number of voxels in the 3D whole sample volume (Ws_v) using the equation,

$$\phi_T = \frac{Tp_v}{Ws_v}. \tag{2.1}$$

Similarly to Equation 2.1, to calculate the volume fraction of ϕ_M and ϕ_m, the voxels

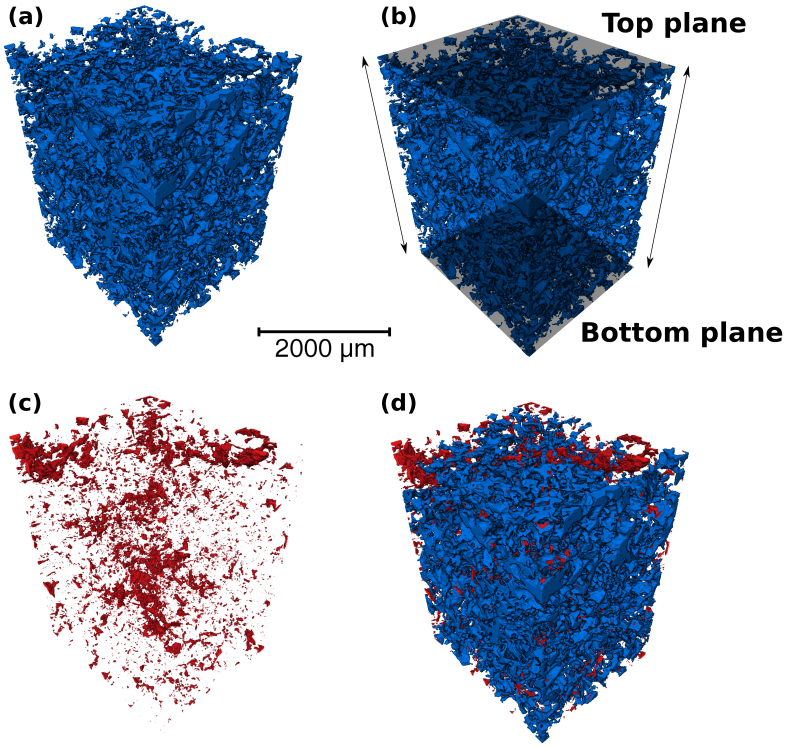

Figure 2.5: 3D volume rendering visualization of porosity in sample BFS1. The total porosity (ϕ_T) is shown in (a). Panel (b) shows the 3D ϕ_T with parallel planes at the top and bottom of the sample. Any voxels that do not connect to the main pore network between these two planes are removed by the axis connectivity algorithm. The isolated voxels that form ineffective pores are shown in (c). Panel (d) shows a visual comparison between effective pores in blue and the isolated pores in red.

in the 3D macroporosity volume (Mp_v) and 3D microporosity volume (mp_v) are divided by the total number of voxels in the 3D whole sample volume (Ws_v). This can be expressed as,

$$\phi_M = \frac{Mp_v}{Ws_v}, \tag{2.2}$$

and

$$\phi_m = \frac{mp_v}{Ws_v}. \tag{2.3}$$

The total porosity (ϕ_T) is the addition of all voxels that represent the macroporosity (ϕ_M) and microporosity (ϕ_m), given by,

$$\phi_T = \phi_M + \phi_m. \tag{2.4}$$

To obtain the effective or connected porosity, the 3D porosity volume of interest is processed using an axis connectivity algorithm. This was performed along the Z-axis (Figure 2.5(b)), where given two parallel planes at the top and bottom of the 3D binary image, the algorithm generates a new 3D binary image containing only voxels that form paths connecting the two planes. Figure 2.5(c) shows isolated voxels that do not form part of the effective pore network between the two parallel planes, and are subsequently removed during the process. To visualize the proportion of isolated pores, the 3D volumes must be further processed using a subtract image algorithm. The effective porosity volume is subtracted from the total porosity volume to produce a 3D binary image containing voxels that represent the isolated pores. 3D volume rendered images provide useful visual comparisons between the proportion of effective and isolated porosity. Figure 2.5(d) shows a visualization of the pore network, where total effective porosity is shown in blue and isolated pores are displayed in red.

2.3.2 Pore and grain geometry

To measure the dimensions of the pores, throats and grains through 3D micro CT images it is necessary to generate network models. While these are more commonly used to quantify the geometry of the pore space, they can also be used to measure individual grains. The outcome of these models provides useful information, including coordination number (number of throats connected to each pore), pore and throat radius, throat length, and the length and width of grains.

The PerGeos software has a built in extension which allows the generation of network models. The algorithm used in this extension is similar for both the pore space and grains, with a few minor exceptions. A pore network model (PNM) is generated using a hybrid algorithm which is detailed more comprehensively by Youssef et al. (2007). The key steps describing the algorithm are provided below:

- Initially, a segmented pore volume is selected and the algorithm extracts a one-voxel thick skeleton from the 3D pore image that preserves the natural geometry.

- To do this, the shortest distance of each point of the foreground (pore space) is computed to the background (grain). A distance map is created which guides the thinning process during skeleton generation.

- Next, the distance map is used to mark each point of the skeleton with the minimum distance to the boundary of the pore space. The algorithm then calculates the length and connectivity of each line.

- The radius, also obtained from the distance map, is used to classify pores and throats. If the radius of a line is larger than its length, then the line is designated as a pore. If the radius is shorter than the length of the line, then it is a throat.

- Finally, the one-voxel line skeleton is expanded in separate pores and throats to allow the calculation of the radius of an equivalent sphere, the length and equivalent hydraulic radius of the throats.

The approach to grain separation and measurement follows a similar step by step progression. However, to avoid repetition, the additional steps are not reported here. Instead, the reader is referred to Chapter 6, section 2.4 where there is a more detailed description of the processes involved.

2.3.3 Permeability

To assess the influence of pore connectivity on permeability, the 3D pore volume images are used to simulate the flow of fluid directly through the effective pore network. Absolute permeability measurements are obtained using the finite volume solver in the petrophysics module of PerGeos. The flow of water through the 3D effective pore network can be described by the Stokes equation,

$$\nabla \cdot \boldsymbol{u} = 0, \tag{2.5}$$

$$-\nabla P + \mu \nabla^2 \boldsymbol{u} = 0, \tag{2.6}$$

where $\boldsymbol{u}$ is the fluid velocity vector, P is the pressure and $\mu = 1 \times 10^{-3}$ Pa.s is viscosity of water. Equations (2.5) and (2.6) are solved with a set of specified boundary conditions. The boundary conditions are kept constant for all permeability simulations in this research. These are described in more detail in Chapter 3, section 2.2.2.

Chapter 3

Image Segmentation and Analysis of Pore Network Geometry in Two Natural Sandstones

Description. This chapter is presented in manuscript format and is published in Solid Earth Geophysics, a section of the journal Frontiers in Earth Science. This work compares the pore geometry of two sandstones with quite variable porosity. A multiple stage technique is used to filter and segment the CT images before analysis of the pore geometries. As porosity increases from 4 to 16%, the median coordination number (connectivity of each pore and throats) of pores increases from 2 to 6. This was attributed to the pore network characteristics where the low porosity Fontainebleau sandstone has fewer, larger pores ($\sim$4.5 um radius) and throats ($\sim$3.8 um radius), while the Berea sandstone has a denser framework of numerous smaller pores ($\sim$2.7 um radius) and throats ($\sim$1.3 um radius).

Author contribution. Paul-Ross Thomson performed the image filtering and segmentation, conducted the image analysis, interpreted the data, generated most figures and wrote most of the manuscript.

Reference. Thomson, P.R., Aituar-Zhakupova, A. and Hier-Majumder, S., 2018. Image Segmentation and Analysis of Pore Network Geometry in Two Natural Sandstones. Frontiers in Earth Science, 6, p.58.

frontiers in Earth Science

ORIGINAL RESEARCH
published: 08 June 2018
doi: 10.3389/feart.2018.00058

Image Segmentation and Analysis of Pore Network Geometry in Two Natural Sandstones

*Paul-Ross Thomson, Aizhan Aituar-Zhakupova and Saswata Hier-Majumder**

Department of Earth Sciences, Royal Holloway University of London, Egham, United Kingdom

We report the results of pore-network analysis of high resolution synchrotron microtomographic images of Fontainebleau and Berea Sandstones. We segment the gray-scale images of the rocks into constituent phases, and analyze the geometry of the pore network. The network consists of pores situated at the corner of grains and serve as the junction between elongated throats along grain edges. Our analysis indicates that the number of pores, their median coordination number, and fraction of connected pore space increases with an increase in porosity. In contrast, the width and length of throats decrease with an increase in total porosity. In each sample, the coordination number of pores is directly related to the radius of the pores, while the length of throats are also positively correlated with the throat radius. The permeability determined from the images increase with the total connected porosity of the samples and there is a change in the modeled permeability for each sample with flow direction. We observe that the dimensionless coefficient of variation of the throat lengths in all samples are nearly uniform around an average value of 0.64. The coefficient of variation of throat radii are generally higher than that of the radius of pores.

Keywords: digital rock physics, porosity, sandstone, microfluid, petrophysics

OPEN ACCESS

Edited by:
Marie Estelle Solange Violay,
École Polytechnique Fédérale de Lausanne, Switzerland

Reviewed by:
Beatriz Quintal,
Université de Lausanne, Switzerland
Jessica M. Furrer,
Benedict College, United States

****Correspondence:***
Saswata Hier-Majumder
saswata.hier-majumder@rhul.ac.uk

Specialty section:
This article was submitted to Solid Earth Geophysics, a section of the journal Frontiers in Earth Science

Received: *26 February 2018*
Accepted: *07 May 2018*
Published: *08 June 2018*

Citation:
Thomson P-R, Aituar-Zhakupova A and Hier-Majumder S (2018) Image Segmentation and Analysis of Pore Network Geometry in Two Natural Sandstones. Front. Earth Sci. 6:58. doi: 10.3389/feart.2018.00058

1. INTRODUCTION

The flow of fluid in porous rocks is strongly controlled by both the total and interconnected porosity of the rock. In tight, low-porosity reservoirs, the issue of connected pore space becomes crucial while estimating the permeability and reservoir quality. A large number of studies on 2D and 3D image analysis and numerical models indicate that for a given pore volume, the degree of connectivity within a pore network plays a fundamental role in determining the effective transport and elastic properties of porous rocks (Von Bargen and Waff, 1986; Doyen, 1988; Lindquist et al., 2000; Bernabé et al., 2010; Wimert and Hier-Majumder, 2012; Miller et al., 2015).

Traditionally, porosity of reservoir rocks are estimated from laboratory experiments or various well logs such as sonic, resistivity, bulk porosity, and neutron porosity logs. While these logs can provide information about the total pore space in the reservoir, the extent of connectivity of pore space can not be calculated directly from these logs (Ellis and Singer, 2007; Rider and Kennedy, 2011). To estimate the extent of connected porosity and its effect on the permeability, rigorous characterization of pore-scale microstructure is necessary. A number of previous studies attempted to characterize the microstructure of rocks from high resolution 2D SEM images (Doyen, 1988; Yoshino et al., 2005). While useful in characterizing the dihedral angle of the fluids-solid junctions, these studies are unable to quantify the connectivity and distribution of the pore network in three dimensions.

The effectiveness of fluid transport in a porous rock depends both on the total porosity and the pore geometry. Pore space in rocks can be grouped into two entities, pores and throats (Lindquist et al., 2000; Youssef et al., 2007; Bernabé et al., 2010; Alyafei et al., 2013). The degree of connectivity of these entities in the network can be quantified by the coordination number, defined as the number of throats connected to a given pore (**Figure 1d**) (Lindquist et al., 2000). In addition, the width of the throats control the effective hydraulic radius of the rock. While these characteristic geometric features of the pore network can depend on a number of factors such as total porosity, degree of cementation, and the dihedral angle of the wetting fluid, it is desirable to identify universal traits of pore geometry which can be used to calculate effective physical properties of porous rocks (Bernabé et al., 2010). Detailed statistical analysis of three dimensional pore network geometry can identify such fundamental parameters describing these traits.

In rock physics, the role of pore network geometry is often addressed through empirically determined parameters, such as tortuosity. Often determined from fits to experimental data, such parameters lack a direct integration of measurable geometric properties of the pore space. Recent advances in

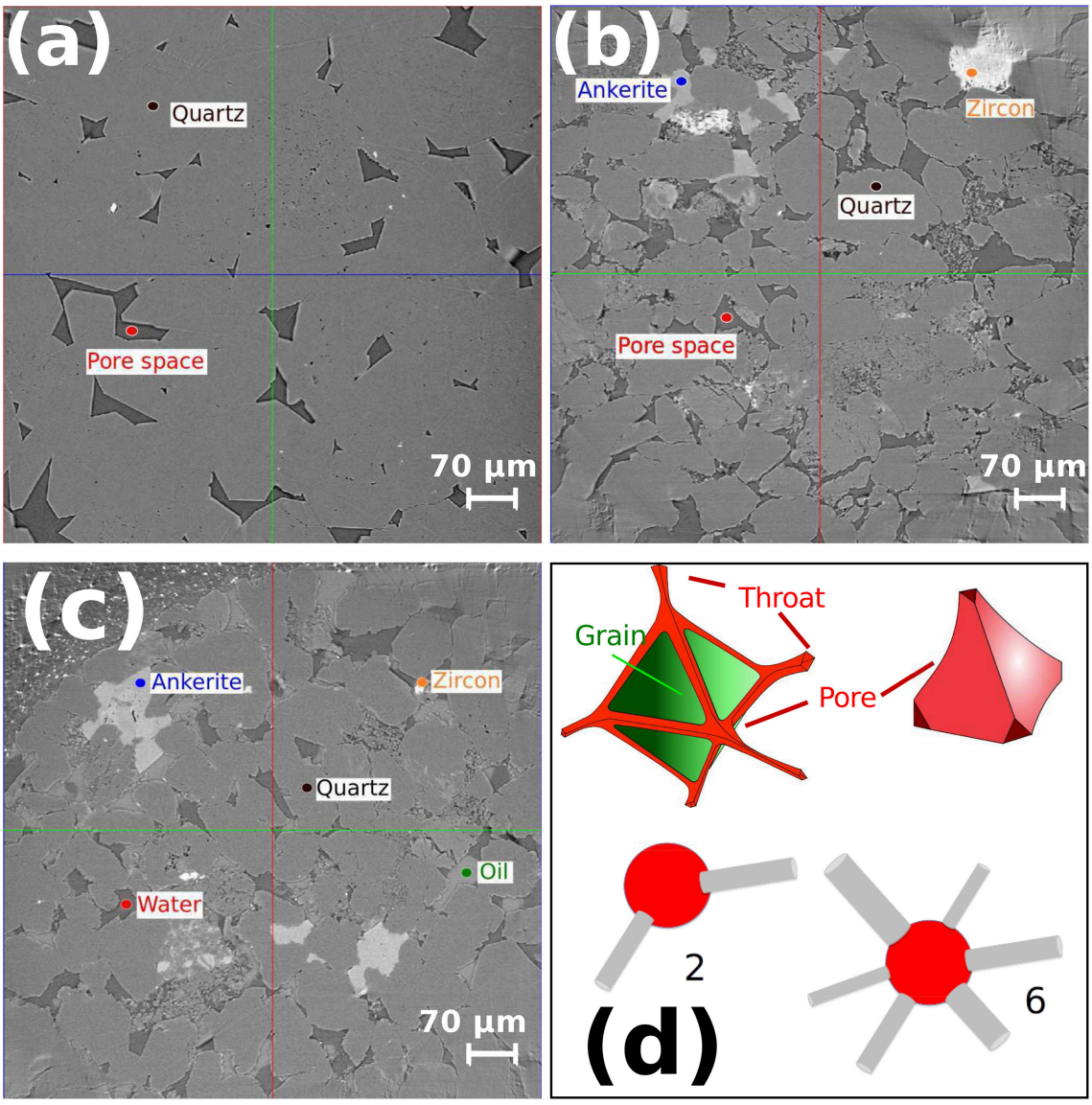

FIGURE 1 | Microtomographic images of the slices of **(a)** dry Fontainebleau, **(b)** dry Berea, and **(c)** saturated Berea sandstones. The key mineral phases in each sample are clearly identified. **(d)** Simplified representations of the pore and throat geometry relationship. Throats are located along the edge of grains, while pores are located at the junction of grain to grain contacts. The spheres (pores) and cylinders (throats) represent an idealized model for the coordination number. As an example, we have shown here a coordination number of 2 and 6.

synchrotron-based X-ray tomography allows a way to address this issue by characterizing pore network geometry from high resolution 3D images (Alyafei et al., 2013; Andrä et al., 2013; Madonna et al., 2013; Sharqawy, 2016). In one work, Bernabé et al. (2010) prescribe a "universal relationship" between the permeability of sandstones and the coordination number of pores. Such prescription of physical property in terms of pore geometry not only directly incorporates microstructural constraints but also allows calculation of permeability for problems such as migration of silicate melts in the Earth's mantle, where geometric parameters are available, but permeability experiments are not viable (Miller et al., 2015). Establishment of such quantitative relations can be developed in two steps: (a) Identifying the relations among parameters such as coordination number, pore and throat radii, throat length, and porosity and (b) quantifying a physical property, such as permeability over a large range of variations of these parameters to establish and test the quantitative relation.

In this article, we address the first part of this approach by providing a detailed recipe for image processing, characterizing pore network geometry, and determining the permeability through connected pore space. An earlier work of Lindquist et al. (2000) used synthetic and low resolution (5.7 μm voxel) tomographic images to characterize pore network geometry. Since throat radii often vary between 1 and 5 microns, proper identification of the smaller pores and throats and the statistical variations of these parameters was beyond the scope of their study. Later studies (Andrä et al., 2013; Madonna et al., 2013) used higher resolution microtomographic images, focusing on the effective physical properties of sandstone. Characteristics and variations in the parameters of pore network geometry was not addressed in these studies. In this article, we bridge the gap by carrying out a detailed analysis of pore network geometry using high resolution (0.74 μm voxel) images of sandstones used by Madonna et al. (2013).

An important step in characterizing the small scale microstructure is segmentation of microtomographic images. Efficient segmentation requires that meaningful regions of the image are extracted accurately. The goal of accurate segmentation is independent separation of phases of interest, in terms of similar brightness or color. It is important to segment key phases of the image correctly because the outcome can generate imprecise or wrong results. The literature reports numerous classical approaches to image segmentation, however there is not one single technique that is equally good for all types of image (Kaestner et al., 2008). We chose a simple yet popular method for image segmentation, with the use of thresholding.

In this work, we address the issue of how the fraction of connected pore space varies with total porosity, quantify the connectivity of the pores and throats as a function of total porosity, and quantify the permeability of these rocks. We take three different sandstone data sets to compare their porosities and absolute permeabilities. All samples were obtained using synchrotron radiation X-ray tomographic microscopy (SRXTM) after Madonna et al. (2013). **Table 1** summarizes the characteristics of the raw data for all three cases.

TABLE 1 | Characteristics of raw data.

Case	Size of data cube	Voxel size
1. Dry Fontainebleau	1,024 × 1,024 × 1,024	$(0.74\ \mu m)^3$
2. Dry Berea	1,024 × 1,024 × 1,024	$(0.74\ \mu m)^3$
3. Oil and Water Saturated Berea	1,024 × 1,024 × 1,024	$(0.74\ \mu m)^3$

In section 2 we detail the methodology behind our work. We outline the filtering and segmentation stages of image preparation in section 2.1. We provide a description of the methods used to analyze the pore space in section 2.2. We define the fundamentals behind the Absolute Permeability Simulations in section 2.2.2. In section 3 we present the results from our work. We describe results from porosity analysis in section 3.1, pore network modeling in section 3.2, and permeability in section 3.3. In section 4 we discuss the outcome and relevance of our results. Finally, we summarize our work in section 5.

2. METHODS

We use the open source tomographic images from Madonna et al. (2013) for the analysis in this work. The microtomographic images were acquired at the TOMCAT (TOmographic Microscopy and Coherent rAdiology experimenTs; Stampanoni et al., 2006) beam-line at the Swiss Light Source (SLS; Paul Scherrer Institute, Villigen, Switzerland). The tomographic volumes were reconstructed using a highly optimized algorithm based on Fourier methods (Marone et al., 2009). For detailed experimental parameters, refer to (Madonna et al., 2013).

We carried out a two-step analysis of the scanned microtomographic images. First, we filtered the 3D volume of gray scale images to remove artifacts and isolate the individual phases within the volume by the process of segmentation. We then analyzed the filtered and segmented images to determine the connectivity and characteristics of the pore network and simulate the flow of pore fluid through the interconnected pore spaces. The image analysis and simulation was carried out in the commercial software PerGeos, from Thermo Scientific. In section 2.1 we outline the details of the first step. In section 2.2 we present a detailed discussion about the methods used to analyze the pore space.

2.1. Image Preparation

The unprocessed image in **Figure 1** displays a number of unwanted artifacts and noise, including streaks, brightness non-uniformity and phase-contrast fringes at the grain edges. As individual phases (minerals and pore fluids) are segregated based on gray scale values, these artifacts can be erroneously ascribed to other phases or designated as new phases during segmentation. In order to avoid these errors, the artifacts need to be removed from 3D volume stack of unprocessed images. We extracted a sub volume of the data from the original volume reducing the number of image cube elements from 1,024 × 1,024 × 1,024 to 500 × 500 × 500. Selection of such a region of interest allows computational efficiency for detailed image filtering and

simulations. We then processed the data with noise filtering and image segmentation.

We used the Interactive Top Hat (ITH) threshold filter in PerGeos to highlight the bright phase-contrast fringes found at the quartz grain boundaries. The process of selection of the fringes is outlined in **Figure 2a**. The final filtered image ($\mathcal{I}_{\mathcal{F}}$) is shown at different resolutions in **Figures 3b,e**. This filter detects the dark or white areas, which correspond to the valleys or peaks of the threshold histogram. We chose the White Top Hat option in PerGeos to select the bright fringes and assign the fringes a value of 1 in a resultant binary image, shown in **Figure 2b**, where all other regions were assigned a value of 0.

Once the binary image map of the bright fringes, $\mathcal{B}$, is created in **Figure 2b** we use it to subtract the excess brightness $\Delta\mathcal{I}$ from the unprocessed image, $\mathcal{I}$, to obtain the filtered image, $\mathcal{I}_{\mathcal{F}}$, using the formula,

$$\mathcal{I}_{\mathcal{F}} = \mathcal{I} - \mathcal{B} \times \Delta\mathcal{I}. \quad (1)$$

The filter defined in the equation above is carried out as an element-wise matrix operation on each 2D image in the 3D volume stack. We use a constant value of $\Delta\mathcal{I} = 5,000$, the difference between the median gray scale values of the interior of the quartz grains and the rim, derived from the unprocessed image. The image in **Figure 3a** shows $\mathcal{I}$, the unprocessed image, while the image in **Figure 3c** zooms inside the red rectangle in **Figure 3a**. The image in **Figure 3d** shows the same region from the image $\mathcal{I}_{\mathcal{F}}$, with the bright fringe removed.

While the filter discussed above removes the bright rim, interior of the grains and pore spaces can contain specular noise. We chose the Non-Local Means (NLM) filter (Buades et al., 2008, 2010) to reduce this noise and smooth the images. This algorithm compares the neighborhoods of all voxels in a given search window with the neighbors of the current voxel in order to determine the new value for the current voxel. The similarity between the neighbors determines the weight with which the value of a voxel in the search window will influence the new value of the current voxel. The final weights are determined by applying a Gauss kernel to the similarity values. The resulting image contains less noise without significant loss of details. The images in **Figures 3b,e** show the result of processing the image, $\mathcal{I}_{\mathcal{F}}$, with the NLM filter. The zoomed image in **Figure 3e** illustrates the uniform gray-scale values in the grain interior after application of the NLM filter.

Following the process of the filtering outlined above, there is now a clear contrast in brightness and color between key phases in the images (e.g., grain and water-saturated pore; **Figure 3e**). To segment the image, we manually selected the individual phases based on their gray-scale values. The image in **Figure 4a** outlines an example where the pore space is highlighted in blue after thresholding. **Figure 4b** shows the histogram plot for the gray scale range used to manually select the key phases in the image. Although the filter process is efficient and clear cut-offs can be derived based on the gray-scale values, a level of uncertainty still exists with thresholding as the selection of histogram ranges is dependent upon our own interpretation of each phase in the image (Saxena et al., 2017). To address this issue, we compared the output from another segmentation method, a semi-automatic threshold algorithm, the Marker-Based Watershed technique. We found that this algorithm provided an overestimation of one or more of the key phases in the image. Over segmentation is a common problem of watershed techniques (Haralick and Shapiro, 1985; Beucher, 1992), particularly when using data such as ours that has had significant beam hardening leading to significant image noise. In an attempt to counter this issue, the Marker-Watershed algorithm from PerGeos first generates a gradient from the original image as part of preprocessing before

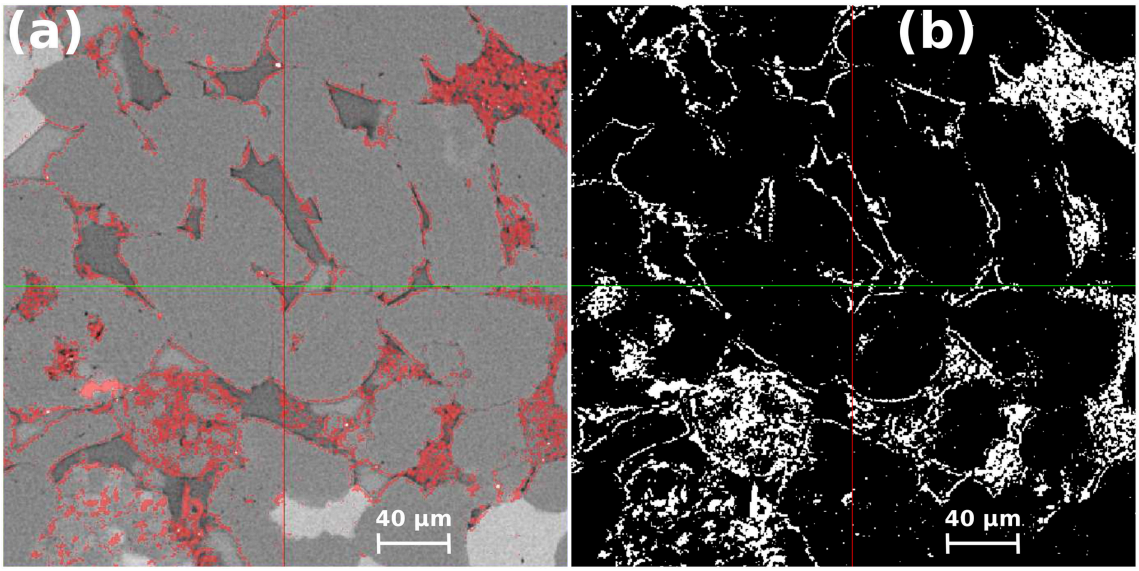

FIGURE 2 | The ITH threshold filter on saturated Berea sandstone image slices 2D. **(a)** Selection of the bright phase-contrast fringes at the quartz grain boundaries. **(b)** Resultant binary image showing the bright fringes with a value of 1.

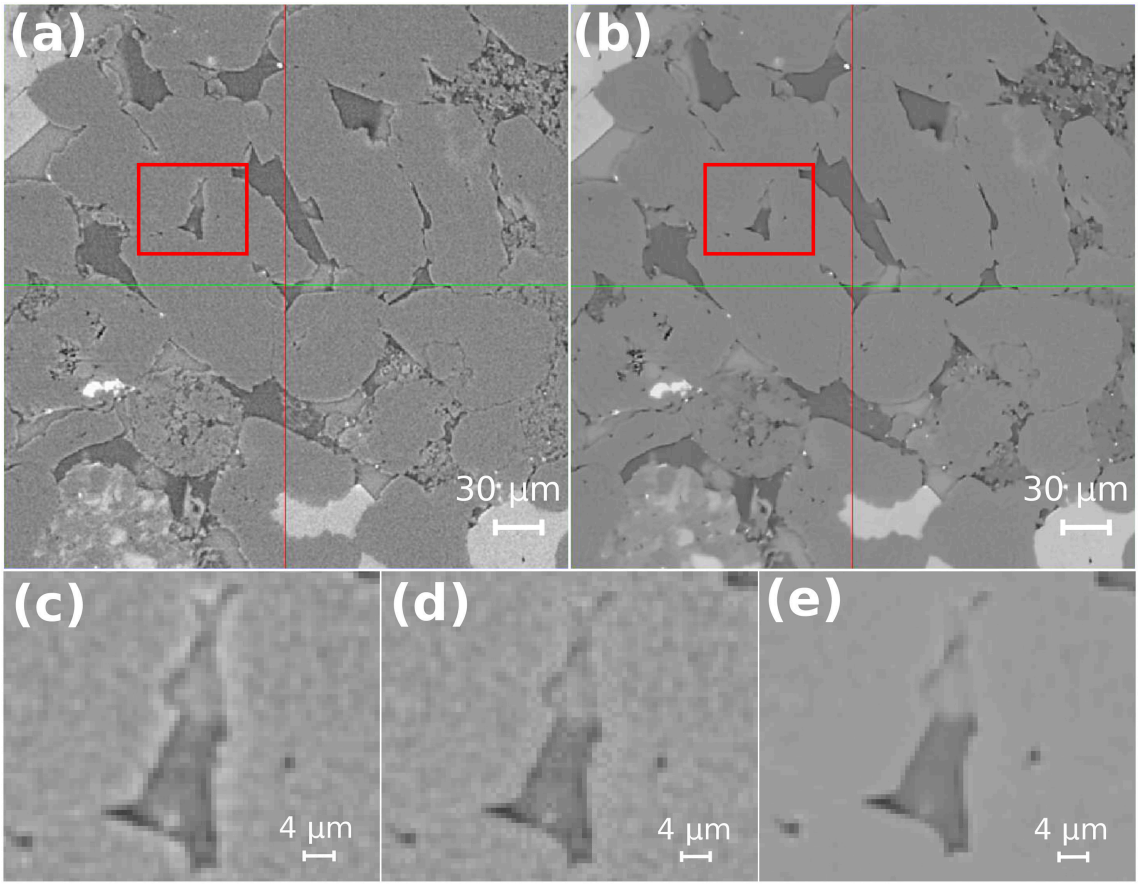

FIGURE 3 | Noise filtering on saturated Berea sandstone image slice 2D. **(a)** Uncleaned image, **(b)** filtered image, **(c)** focused zoom of uncleaned image outlining bright fringes at grain boundaries, **(d)** focused zoom of uncleaned image showing the reduced brightness at grain boundaries and **(e)** focused zoom of filtered image showing little or no phase-contrast at quartz grain boundaries and reduced specular noise at grain interiors.

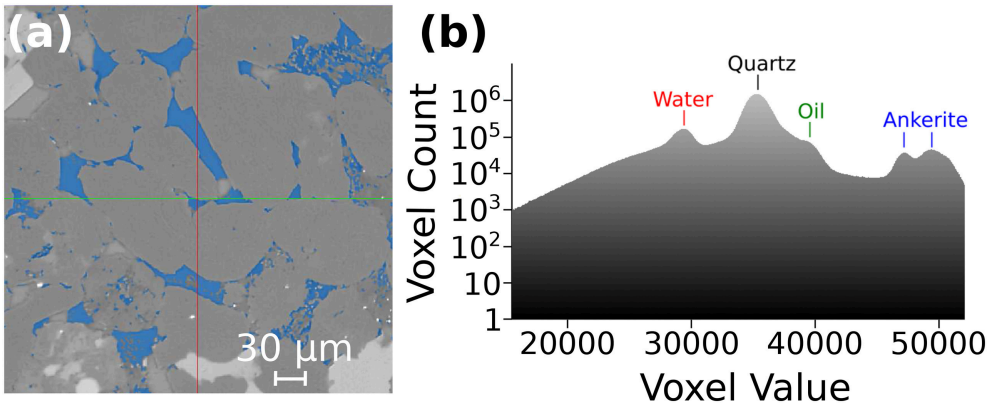

FIGURE 4 | Interactive Threshold segmentation on saturated Berea sandstone filtered image slice 2D. **(a)** The selection of the pore space phase is shown here highlighted in blue. **(b)** The histogram range for the filtered image used to select separate phases.

filling the pre-determined markers to complete the segmentation of all phases in the image. When comparing the segmentation results for the pore space volume in the saturated Berea sample, we found that the watershed technique overestimated the pore volume by 5% (24% compared to 19%). Our filtering and threshold segmentation results for the pore space volume

matched closely with helium density and mercury porosimetry experiments carried out by Madonna et al. (2013) on the same rock sample. For this reason, we used the manual segmentation method throughout this work.

While filtering and thresholding allowed smoothing, identification, and segmentation of individual phases, there were additional artifacts such as intragranular pits, which are incorrectly identified as pore space due to similar gray scale values. This feature was especially dominant in the sample of Fontainebleau sandstone. We carried out further thresholding of the Fontainebleau images to manually filter out these artifacts brushing noisy voxels slice by slice. Careful consideration was required to ensure that we did not remove voxels that were representative of the true pore space.

2.2. Image Analysis

The primary objective of this article is to identify connected porosity, quantify the relationship between the attributes of pore geometry such as area and volume of pores, and calculate the permeability from the 3D volume stacks of filtered and segmented images. The first set of tasks are carried out by pore network modeling. After extracting the connected pore space by pore network modeling, we carried out numerical simulations of fluid flow through the 3D images of the connected pore space. Details of these two steps are discussed next.

2.2.1. Pore Network Model

Once the 3D image stacks are segmented into appropriate phases, we extract the pore phase for further analysis. Since the goal of this analysis is to quantify the geometry of the water-saturated pore, in the oil-bearing Berea sandstone, we selected only the water-saturated part of the pore space for further analysis. We discuss more about this issue in section 3.1. The pore network consists of two major components, pores and throats. In this model, linear throats are distributed along three grain junctions and connect with each other through the grain corner pores, which act as junctions. To identify the connected pore volume fraction and quantify the geometric parameters of the throats and pores, we used the pore network model (PNM) extension in PerGeos.

The PNM extension is based on a hybrid algorithm, detailed extensively by Youssef et al. (2007). The first step involves generating a one-voxel thick skeleton of the entire pore space. The skeletonization algorithm is developed from work involving micro-vascular network analysis (Fouard et al., 2004), and involves calculating the shortest distance of each point of the foreground (void space) to the background. The distance map (e.g., Fontainebleau sandstone, **Figure 5a**) is used to uniformly erode the pore-grain interface until the skeleton shown in **Figure 5b** is obtained. Next, the algorithm calculates the length and connectivity of each line. If an extreme radius (known from the distance map) of a line is larger than its length, then the line is classified as a pore, otherwise the line is designated as a throat (Youssef et al., 2007). At this stage, we calculate the coordination number —the number of throats connected to a given pore— for each pore, and identify the throats associated with each pore. Isolated pores and throats are grouped as unconnected pore space. The one voxel wide image is then expanded to fit the boundary of each pore and throat. During the expansion, we calculate the radius of a sphere that can fit within a pore and the length and equivalent hydraulic radius of each throat. The outcome of this process is two sets of data: (1) the coordination number, radius, area, and volume of each pore and (2) the radius and length of each throat. The labeled image in **Figure 5c** outlines the outcome of this process, with individual pores and throats colored differently.

2.2.2. Absolute Permeability Simulation

We calculate the permeability of the rock by simulating flow of water directly through the 3D images of the connected pore space

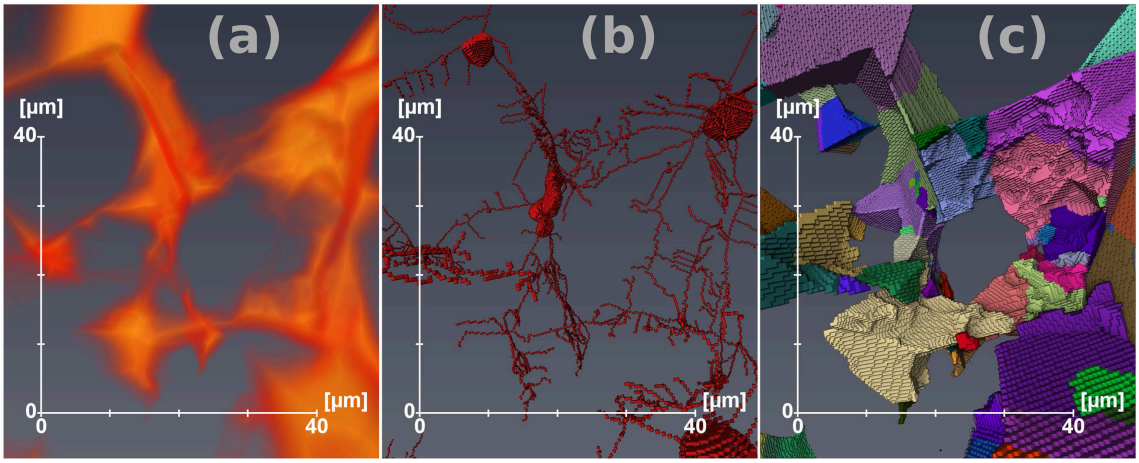

FIGURE 5 | Steps involved in the generation of pore network models, shown here using the Fontainebleau pore network. **(a)** Distance map used to guide the thinning process. **(b)** One-voxel thick skeleton of the pore space. **(c)** Separated pore space image with individual pores and throats colored differently.

obtained from the steps described above. Within the connected pore space, the flow of water can be described by Stokes equation,

$$\nabla \cdot \boldsymbol{u} = 0, \quad (2)$$

$$-\nabla P + \mu \nabla^2 \boldsymbol{u} = 0, \quad (3)$$

where $\boldsymbol{u}$ is the fluid velocity vector, P is the pressure and $\mu = 1 \times 10^{-3}$ Pa.s is viscosity of water.

We used the Absolute Permeability Experiment Simulation module in PerGeos to solve Equations (2) and (3), with a set of specified boundary conditions: a no-slip condition at fluid-solid interfaces, one voxel wide plane of a solid phase (with no-slip condition) is added on the faces of the image that are not perpendicular to the main flow direction, allowing isolation of the sample from the outside, and no flow out of the system. Experimental setups are added on the faces of the image that are perpendicular to the main flow direction, designed in a manner that creates a stabilization zone where pressure is quasi static, and the fluid can freely spread on the input face of the sample. Finally, two among the following three conditions can be chosen by the user, the third being estimated from the chosen two: input pressure, output pressure, flow rate.

We used a finite volume solver in the petrophysics module of PerGeos to solve for the unknowns, P and $\boldsymbol{u}$. The governing partial differential equations are discretized on a staggered grid for pressure and velocity nodes, allowing a better estimation of the no-slip boundary condition. Pressure unknowns are located at the voxels center, whilst the velocity unknowns are decomposed at the faces of the voxels. The voxels are assumed isotropic (cubic) in the discretization scheme. We carried out a total of 27 numerical simulations for the three samples, varying the input pressure (P input) between 130, 150, and 200 kPa, while keeping the output pressure at a constant value of 100 kPa, to assess the influence of pressure gradient on permeability for three different flow directions (x, y, z).

3. RESULTS

We compare the porosity, PNMs and permeability for the three different sandstones. We show the total porosity and the difference between connected (effective) and unconnected (isolated) porosity for all examples. We also present the pore network of each sandstone, to compare and contrast characteristics of pores and throats. Finally, we highlight the results from absolute permeability simulations on each case and identify the preferential flow pathways through the samples.

3.1. Porosity

Filtering, segmentation, and pore network analysis provides us with the volume fraction of constituent phases while separating connected porosity from isolated pore space. The 3D visualizations in **Figure 6** demonstrate the results for the three cases. In **Figure 6a** we highlight the segmented phases in the saturated Berea sandstone by the color scheme: quartz (black), water (red), ankerite (blue), and oil (green). This visualization provides a representative view of the proportion of each phase in the sample. As the visualization demonstrates, quartz is the dominant phase, followed by water in the pore space. **Table 2** lists the volume fraction of key phases in all samples. In the

TABLE 2 | Summary of the volume fraction of key phases in Fontainebleau, dry Berea, and saturated Berea sandstone.

Case	Volume Fraction					
	Pore	Quartz	Ankerite	Zircon	Clay	Oil
1. Fontainebleau	0.038	0.962	–	–	–	–
2. Dry Berea	0.199	0.734	0.024	0.004	0.033	–
3. Saturated Berea	0.158*	0.756	0.050	3.33×10^{-4}	–	0.035**

*Water in pore space.
**Oil in pore space.

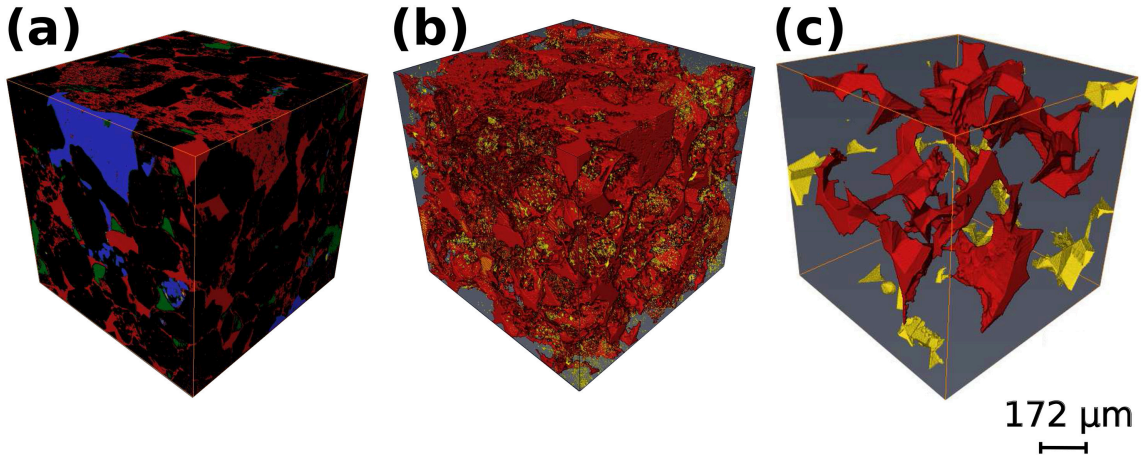

FIGURE 6 | 3D volume rendering visualization of **(a)** saturated Berea sandstone with all phases: quartz (black), water (red), ankerite (blue), and oil (green). **(b,c)** Represent the connected (in red) and unconnected (in gold) pore spaces in the saturated Berea sandstone and Fontainebleau sandstone, respectively.

oil-bearing Berea sandstone, the pore-space contained two fluid phases, oil and water. Since our permeability simulation assumes the presence of only one fluid occupying the pore space, and we are interested in quantifying the connectivity of a single phase network, we only used the water-saturated porosity of this sample. The total physical porosity of this sample was 0.188, while the volume fraction of water-saturated porosity is 0.158. We report the latter porosity in **Table 3**, and use this water saturated pore space in the PNM analysis. Porosity and other pore-geometry related parameters for all three of these samples are described in **Table 3**.

Connectivity of the pore space depends strongly on the total porosity. The two visualizations in **Figures 6b,c** depict the connected (in red) and unconnected (in gold) pore spaces in the dry Berea sandstone and the Fontainebleau sandstone, respectively. While only 0.3 vol% of the total of 20 vol% pore space of the Berea sandstone is isolated, the proportion of isolated to connected pore space is substantially higher in the Fontainebleau sandstone. Nearly a quarter (0.8 vol%) of the total porosity (3.8 vol%) in the Fontainebleau sandstone is isolated. As evidenced by the contrast in the size of the gold-colored pores between **Figures 6b,c**, the isolated pores in the Fontainebleau sandstone are fewer and larger compared to the Berea sandstone. This observation is similar to numerical models of synthetic pore network connectivity, where an increase in the pore volume leads to a reduction of isolated pore spaces (Von Bargen and Waff, 1986; Wimert and Hier-Majumder, 2012). We summarize the results of our porosity analysis in **Table 3** with total, connected and unconnected porosity for all three sandstone examples.

3.2. Pore Network Modeling

The PNM segments the total pore space into a network of pores and throats. The pores, situated at the corner of four or more grains, act as junctions for throats, which are distributed typically along the contact between three grains. The visualizations in **Figure 7** outline the pore network geometry for the two Berea sandstones and the Fontainebleau sandstone as a ball and stick model. In these visualizations, red spheres represent pores and gray cylinders represent the throats.

The visualizations in **Figure 7** demonstrate a clear difference between the Fontainebleau (**Figure 7a**) and Berea sandstones (**Figures 7b,c**). The pore network of Fontainebleau sandstone is less dense, owing to the lower porosity, and consists of fewer larger throats connecting the pores. The network of both Berea sandstones are characterized by a dense mesh of smaller throats.

We compare the characteristics of the pore geometry for the three different sandstone cases: Fontainebleau, dry Berea, and saturated Berea in **Figure 8**. The probability distribution plots in **Figures 8a–c** depict the distributions of coordination number, throat length, and throat radius for the three cases, respectively. We report the median values for all three of these parameters in **Table 3**. The median coordination number for

TABLE 3 | Summary of pore network analysis of the three samples.

Case	ϕ	ϕ_c	ϕ_u	Coordination number	Pore radius (μm)	Throat radius (μm)	Throat length (μm)
1. Fontainebleau	0.038	0.030	0.008	2	4.54	3.82	22.49
2. Dry Berea	0.199	0.196	0.004	6	2.72	1.29	7.64
3. Saturated Berea*	0.158	0.154	0.009	6	2.72	1.32	7.34

The columns contain values for total porosity ϕ, connected porosity (ϕ_c), unconnected porosity (ϕ_u), median values of coordination number of pores, throat radius, and throat length.
**Water bearing porosity.*

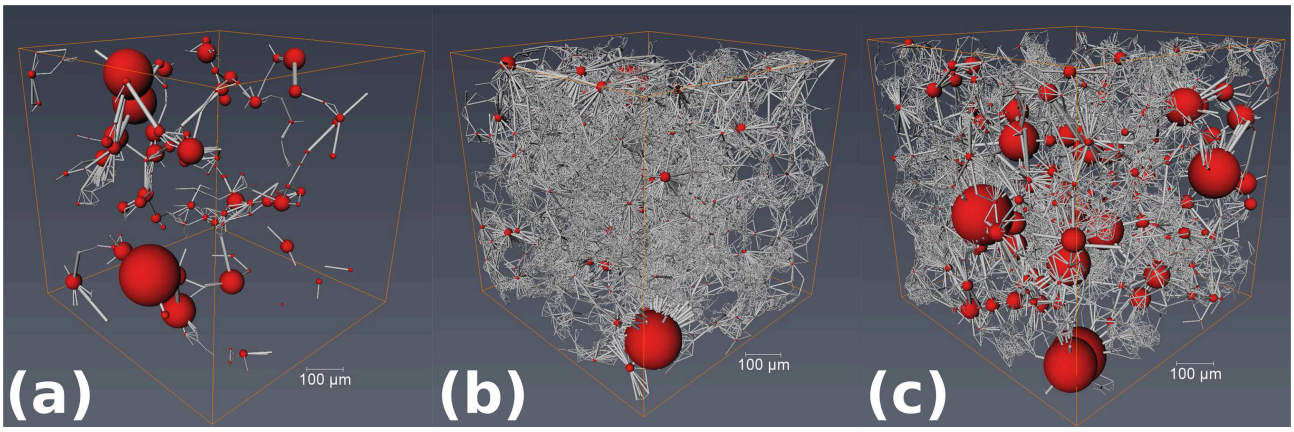

FIGURE 7 | PNM visualization of the three different sandstones. Red spheres represent pores scaled with pore volume, while gray cylinders represent pore throats scaled with length. **(a)** Fontainebleau sandstone, **(b)** dry Berea sandstone, and **(c)** saturated Berea sandstone.

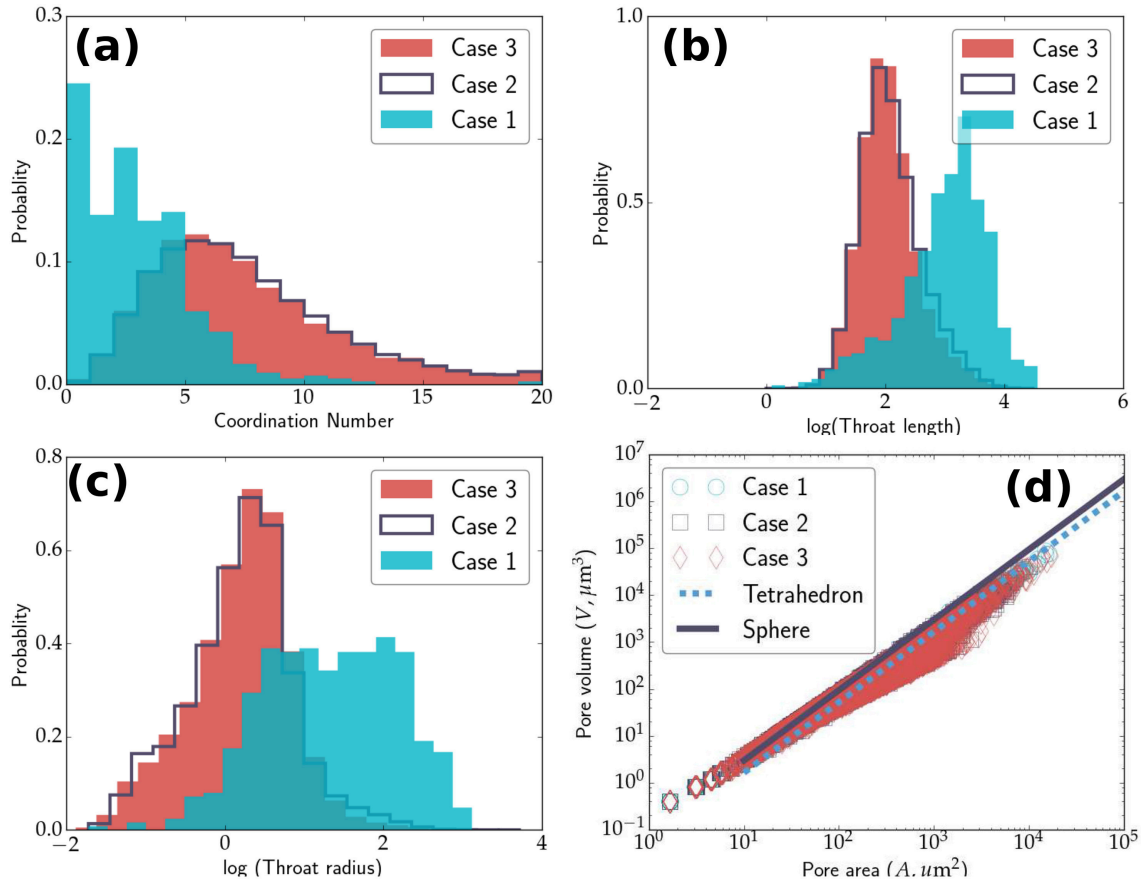

FIGURE 8 | Plots comparing the PNM data for the three different sandstones. Fontainebleau (Case 1), dry Berea (Case 2), and saturated Berea (Case 3). **(a)** Probability distribution plot of coordination number of pores for the two Berea sandstone samples and the Fontainebleau sandstone sample. The median coordination number for both samples of Berea sandstones is 6, while that for Fontainebleau is 2. Probability distribution plots of throat length **(b)** and throat radius **(c)** for the same samples. **(d)** The relationship between the area and volume of all pores in all three samples. The surface area of majority of pores is larger than a sphere or tetrahedron, as expected.

pores in both samples of the Berea sandstone is 6, compared to the median coordination number of 2 for the Fontainebleau sandstone. In addition, the pore network in both samples of the Berea sandstone consists of throats typically 1 μm in radius and 7–8 μm in length. In contrast, the pore network of Fontainebleau sandstones consists of larger throats, with a median radius of 4 μm and a length of 22 μm. The increase in median coordination number and decrease in median throat length with an increase in porosity in our samples agrees quite well with a similar trend observed by Lindquist et al. (2000).

The quantitative analysis of the throat geometry provides an important insight into the capacity of fluid transport by the pore network. The volumetric rate of fluid flow, Q, through a tube of radius r is, $Q \propto r^4$. As the results in **Figures 8b,c** indicate, the presence of such large throats gives the Fontainebleau sandstone a higher permeability, despite the relatively low porosity.

The plot in **Figure 8d** demonstrates the relationship between the area and volume of pores in all three samples. We also plot the volume-area relation for spheres and tetrahedra for comparison. For a given pore volume, the surface area of majority of the pores is larger than a sphere or a tetrahedron. This result is expected, as the sphere is the shape with the minimum surface area for a given volume, and pores are rarely spherical in shape. The departure of the data points from the tetrahedral geometry depicts that the shape of pores are also quite different from tetrahedra as often assumed in microstructure literature (Von Bargen and Waff, 1986).

To understand the nature of pore space connectivity, it is important to quantify the relation between major attributes of the pore geometry obtained from pore network modeling. The plots in **Figure 9** outline the relationship between key parameters associated with pores and throats. To obtain these plots, we divided the data from each sample (for example, 22,224 pores and 91,604 throats from dry Berea sandstone) into 10 bins. The median values of each of these bins are then plotted, with the standard deviation within the bin as the error bar. The plot in **Figure 9a** display a clear positive correlation between the pores radius and coordination number, indicating that larger pores are connected to more throats. Comparison between the two rocks indicate that the slope of the plot is different. In

Figure 9b throat length and radius in Berea sandstone also displays a clear correlation, indicating that longer throats are wider. This correlation, however, is less clear in the sample from the Fontainebleau sandstone, which shows a relatively lower variability in throat length, despite variations in the throat radius.

3.3. Permeability

We show here a visual representation of the absolute permeability simulations for each of the sandstones cases. **Figure 10** displays streamlines, colored by the magnitude of dimensionless fluid velocity, of fluid percolation through the connected pore space. Results of the absolute permeability simulations have been summarized in **Table 4**. We simulated a total of 27 experiments, varying the boundary condition input pressure (P input) between 130, 150, and 200 kPa to assess the influence of gradient change to permeability in all flow directions (x, y, z). Results confirm that there was no change to permeability with increased input pressure. Interestingly, there is a change to permeability for each sample with flow direction. The simulation results for permeability in Fontainebleau sandstone measure at 21.57, 11.02, and 14.80 mD, in the x, y and z flow directions respectively. We observe a permeability decrease of 49 and 31% in the y and z directions when compared to the x direction for this sample. The dry Berea sandstone shows a similar trend with permeability values in the x, y, z, directions of 166.9, 156.4, and 132 mD. This sample also shows a decrease in permeability when comparing flow in the x direction to y and z, with a reduction of 6 and 21% respectively. Our saturated Berea sample has differing permeability results when compared to our other sample of the same rock, the dry Berea. Simulation results in the x, y and z

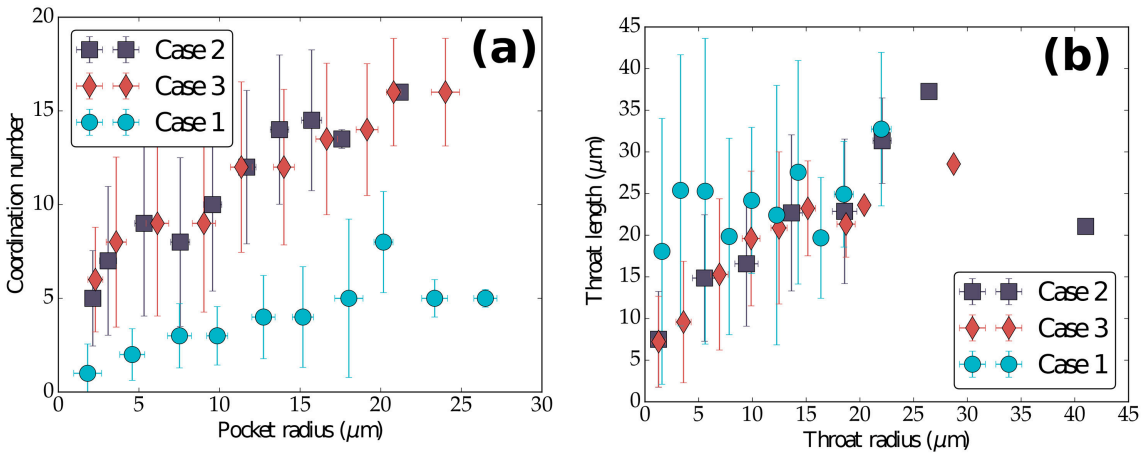

FIGURE 9 | (a) Plot of pore coordination number as a function of pore radius, and **(b)** throat length as a function of throat radius. Each data point represents the median value of binned data. The error bars in the plots correspond to the standard deviation of the data in each bin. Fontainebleau (Case 1), dry Berea (Case 2), and saturated Berea (Case 3).

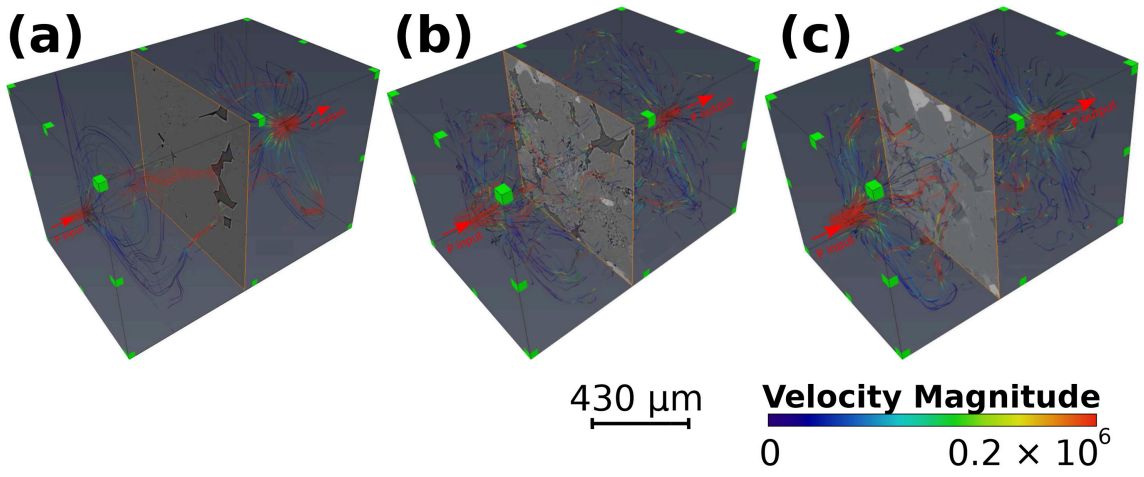

FIGURE 10 | Absolute permeability simulations through **(a)** Fontainebleau sandstone, **(b)** dry Berea sandstone, and **(c)** saturated Berea sandstone. Areas with increased velocity are shown with red streamlines and are interpreted as preferential fluid flow pathways, whilst areas of reduced velocity magnitude are shown in blue.

flow directions for this sample are 68.03, 61.48, and 116.3 mD. We note a similar reduction in permeability in the y direction compared to the x direction, with a decrease of 10%. However, there is an increase in permeability observed in the z direction, with a 71% change compared to the x direction.

In the following section, we discuss the implications of our results and compare them with the results from previous studies on image analysis and laboratory experiments.

4. DISCUSSION

4.1. Pore Network Geometry

Our results on coordination number of pores agree well with previous studies involving image analysis and simulated microstructures. The plot in **Figure 9A** demonstrates that the coordination number of pores increase with the radius of the pore. Lindquist et al. (2000) carried out a similar pore network analysis on core samples of the Fontainebleau sandstone with porosities between 0.07 and 0.22. While the image resolution, segmentation, and skeletonization algorithm in their work was different from ours, they also observed an increase in average coordination number with an increase in pore radius and an increase in the median coordination number with porosity. As the pore volume fraction increases, the volume occupied by the pores also increases. Numerical simulations of pore geometry using level set methods (Ghanbarzadeh et al., 2015), surface tension minimization (Von Bargen and Waff, 1986), and steady-state microstructure (Wimert and Hier-Majumder, 2012) support this observation.

Another key feature of our observation involves the variations in length and radius of the throats. First, we note that the Fontainebleau sandstone is characterized by only 520 throats compared to more than 80,000 throats in each of the two samples of the Berea sandstone. While much fewer in number, the throats in the Fontainebleau sandstone are much wider and longer than those in the Berea sandstone, as shown in **Table 3**. In addition, the subvolume of Fontainebleau sample contains only 420 pores, while those of the Berea sandstone contains over 20,000 pores. Combined together, this result indicates that there are fewer junctions between the network of large conduits in the Fontainebleau sandstone, while the Berea sandstone consists of dense network of short, narrow throats, frequently joined by pores. This distinction between the two networks, visible in **Figure 9**, is also strongly supported by previous studies in image analysis (Lindquist et al., 2000) and numerical models (Von Bargen and Waff, 1986; Wimert and Hier-Majumder, 2012; Ghanbarzadeh et al., 2015).

One way of normalizing differences in results arising from image resolution and experimental errors is to identify dimensionless characteristic parameters of pore geometry. As these parameters are independent of methods of measurement, they are universal in nature. The generic relationship between these parameters and effective physical properties can be applied to a large variety of porous or fluid saturated multiphase aggregates. Such dimensionless parameters can be extremely useful in quantifying transport properties of deep mantle rocks containing partial melt, where the only estimate of pore fluid fraction can be obtained from seismic signals (Hier-Majumder and Revenaugh, 2010; Hier-Majumder, 2014; Miller et al., 2015; Hier-majumder and Tauzin, 2017).

Lindquist et al. (2000) presented a detailed study of various elements of pore geometry and their probability distribution. In a later work, Bernabé et al. (2010), expanded on this concept and identified two key dimensionless, universal parameters: coordination number of pores and the coefficient of variation of pore radius, $\sigma_r/\langle r\rangle$. The data in **Table 5** lists the coefficients of variation for pore and throat radii and throat length. We also calculated the hydraulic radius as the average of the maximum and minimum throat radii. The results from our PNM agree well with the compilation of Bernabé et al. (2010). For example, Bernabé et al. (2010) calculate $\sigma_r/\langle r\rangle$ in the ranges 0.4–0.6 for pores and 0.7–0.8 for throats from the measurements of Doyen (1988) and Lindquist et al. (2000). With the exception of $\sigma_r/\langle r\rangle$ for pores in the Fontainebleau sandstone, our other results are in good agreement with their finding. We also find a nearly uniform value of $\sigma_l/\langle l\rangle$ for the throats in all samples. Despite the variations in porosity and mineral composition, the similarity between these values indicate that the coefficient of variation can act as a dimensionless, universal descriptor of pore geometry. Bernabé et al. (2010) identify that the permeability of porous rocks can be described as a function of coordination number of pores, hydraulic radius, and $\sigma_r/\langle r\rangle$ from PNMs. These estimates can serve as an independent measure of permeability. Future work in characterizing such relations will be beneficial in digital rock physics analysis of permeability of porous crustal rocks as well as deep mantle rocks containing small amounts of melt.

Finally, an important outcome of our analysis is the relationship between total porosity and isolated porosity. As results in **Table 3** indicate, nearly 26% of the pore space in the Fontainebleau sandstone is unconnected, while the unconnected porosity in the Berea sandstone samples vary between 2 and 6%.

TABLE 4 | Porosity and permeability values of the samples analyzed.

Case	ϕ	k_x (mD)	k_y (mD)	k_z (mD)
1. Fontainebleau	0.038	21.57	11.02	14.80
2. Dry Berea	0.199	166.9	156.4	132.0
3. Saturated Berea	0.158	68.03	61.48	116.3

The columns contain values for total porosity ϕ and permeability in mD, calculated for flow normal to the three faces of the 3D volume.

TABLE 5 | Coefficients of variation for pore and throat radii and throat lengths for the three samples.

Case	$\sigma_r/\langle r\rangle$ Pore	$\sigma_r/\langle r\rangle$ Throat	$\sigma_l/\langle l\rangle$ Throat	Hydraulic radius (μm)
1. Fontainebleau	0.92	0.80	0.63	11.37
2. Dry Berea	0.60	0.83	0.64	20.60
3. Saturated Berea	0.57	0.74	0.65	14.44

The hydraulic radius was calculated from throat radius using the formula $r_H = (r_{max} + r_{min})/2$.

Due to the presence of short grain edge throats, the grain corner pores in the higher porosity samples become better connected. This observation of higher pore connectivity at higher porosity strongly supports the theoretical models of pore networks using fluid mechanical and geometrical models (Von Bargen and Waff, 1986; Wimert and Hier-Majumder, 2012; Ghanbarzadeh et al., 2015).

4.2. Permeability

The results from our permeability calculations are in agreement with the previous digital rock physics analysis by Andrä et al. (2013) and Sharqawy (2016). Both of these results also display general agreement with the experimental measurements by Yale (1984). As the plot in **Figure 11** indicates, however, the numerical measurements from synchrotron microtomographic images (squares) can differ from experimental measurements (plotted as dots, Bourbié and Zinszner, 1985; Doyen, 1988; Gomez et al., 2010; Revil et al., 2014). One source of the disagreement between the numerical models and the experimental data can be the sample scale. Owing to the high resolution of the synchrotron microtomographic images, the volume for porous flow modeling is small. As a result, the volume used for permeability calculations from synchrotron images may not represent the full extent of heterogeneity in the rocks. From our results for the Fontainebleau sandstone we observe that the data lies to the left of the general trend for experimental data. A similar disagreement between numerical and experimental data has been highlighted in other work (Alyafei et al., 2013; Andrä et al., 2013), where their results show that lower-permeability sandstones, with more poorly connected pore networks, have simulated permeabilities that are much higher than the experimental core measurements for the same rock. This supports what we see from our PNM analysis of the Fontainebleau sandstone and helps provide a possible explanation for the location of the results in the plot (**Figure 11**). As this technique continues to develop, further future studies are needed to reconcile this disagreement between experimental measurements and digital rock physics analysis using high resolution images.

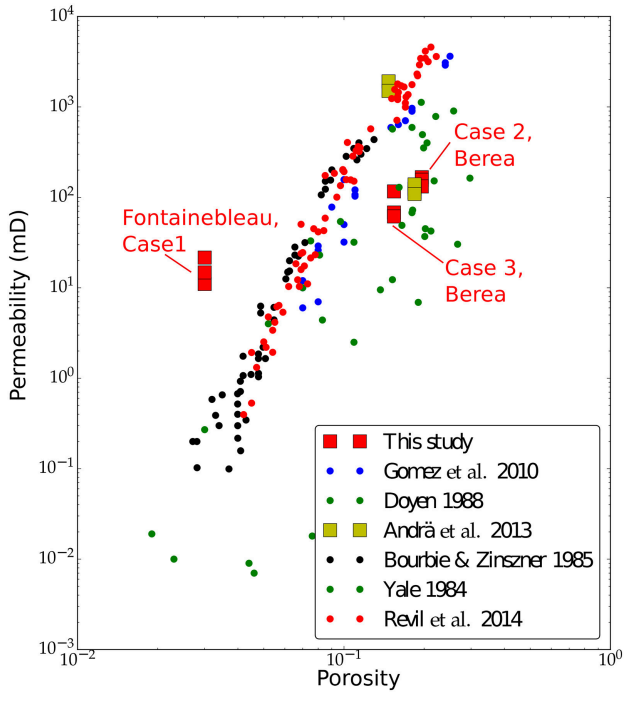

FIGURE 11 | Log-log plot of permeability as a function of total porosity from our measurements with numerical models of Andrä et al. (2013), and experimental measurements of Doyen (1988), Bourbié and Zinszner (1985), Yale (1984), and Gomez et al. (2010). Data points corresponding to the three cases studied here are annotated in the figure. Numerical values of the data points from this study are provided in **Table 4**.

Our results also demonstrate anisotropic permeability, which is observed in all of our samples. Knowledge of such variation with flow direction is crucial for reservoir engineering and hydrocarbon recovery applications. We see that our results share some similarities with other work looking at the multidirectional variation of permeability (Clavaud et al., 2008; Peyman and Apostolos, 2017). However, we also note from our results that the difference in permeability with flow direction differs from results obtained by Peyman and Apostolos (2017) on the same Berea sandstone. Their results indicate a permeability decrease in the y and z-directions of 23 and 21%, respectively. From our simulations we have permeability reductions in the y and z-directions of 6 and 21% for the dry Berea. Whilst the saturated Berea shows a decrease in the y-direction with a 10% drop, the z-direction shows a percentage increase of 71%. Our samples may be more or less heterogeneous in particular flow directions, which is one possible reason behind this variation in permeability. The voxel resolution can also produce relatively large variation in flow properties (Saxena et al., 2017), which may also explain what we see when comparing our results to other work. It has been pointed out in previous work by Wright et al. (2006), that a possible explanation for anisotropic permeability in sandstones is due to the orientation of mineral grains and pores. We suggest future work using numerical methods to evaluate the influence of grain and pore orientation on permeability in different flow directions.

Our results have implications for the production of hydrocarbons in the oil and gas industry. Although the size of our data samples are small and therefore may not represent the true reservoir heterogeneity, permeability results give an indication to overall preferential flow direction. A study involving the acquisition and processing of numerous samples from various horizons in the reservoir would provide useful information to evaluate the permeability anisotropy at a larger scale. As techniques in digital rock physics continue to develop, further work is required to investigate the relationship between grain/pore orientation and anisotropic permeability. A comparison using numerical methods, combined with samples at a range of different resolutions would provide valuable information to this line of research. This will aid in our understanding of reservoir heterogeneity and will help researchers assess the most efficient techniques for comparison to traditional experimental and well test measurements.

5. CONCLUSIONS

We find that our combination of image filtering and threshold segmentation methods provide meaningful and acceptable results for pore geometry analysis and single phase fluid flow modeling using micro tomographic images with multiple phases and significant noise. As the porosity increases from 4% to 16%, the median coordination number of pores increases from 2 to 6. The lower porosity Fontainebleau sandstone is characterized by fewer, larger pores and throats (pore radius 4.5 μ m and throat radius 3.8 μ m). In contrast, both samples of the Berea sandstone are characterized by a dense network of numerous smaller pores ($\sim$2.7 μm radius) and throats ($\sim$1.3 μm radius). We also observe a decrease in isolated pore space with an increase in porosity, resulting in a higher coordination number of the Berea sandstone. Fluid flow simulations highlight anisotropic permeability which is probably due to heterogeneity in the sample, more than likely caused by the variation in orientation of grains and pores in each direction.

DATA AVAILABILITY STATEMENT

The raw 3D Images used in this work were downloaded from the ETH Zürich Rock Physics Network. The pore network modeling data sets GENERATED for this study can be found in the Zenodo repository (Thomson et al., 2018a). Segmented images of the pore network GENERATED for this study can be found in the Figshare repository (Thomson et al., 2018b).

AUTHOR CONTRIBUTIONS

P-RT carried out the image segmentation and permeability simulations in all samples. AA-Z carried out initial segmentation, permeability calculation, and pore network modeling in samples for the Fontainebleau and dry Berea sandstones. SH-M and P-RT jointly carried out the final pore-network modeling and statistical analysis. All three authors contributed to writing and revision of the manuscript.

FUNDING

P-RT acknowledges support from a NERC Oil and Gas CDT graduate fellowship (grant number NE/M00578X/1).

ACKNOWLEDGMENTS

AA-Z was funded by the Bolashak scholarship from the Kazakhstani Government. Financial support for this research was provided by RHUL internal funding.

REFERENCES

Alyafei, N., Ic, I. C., Gharbi, O., Raeini, A. Q., and Yang, J. (2013). *IPTC 16600 Influence of Micro-Computed Tomography Image Resolution on the Predictions of Petrophysical Properties* (Beijing).

Andrä, H., Combaret, N., Dvorkin, J., Glatt, E., Han, J., Kabel, M., et al. (2013). Digital rock physics benchmarks-Part I: imaging and segmentation. *Comp. Geosci.* 50, 25–32. doi: 10.1016/j.cageo.2012.09.005

Bernabé, Y., Li, M., and Maineult, A. (2010). Permeability and pore connectivity: a new model based on network simulations. *J. Geophys. Res. Solid Earth* 115, 1–14. doi: 10.1029/2010JB007444

Beucher, S. (1992). "The watershed transformation applied to image segmentation," in *Proceedings of the 10th Pfefferkorn Conference on Signal and Image Processing in Microscopy and Microanalysis*, 299–314.

Bourbié, T., and Zinszner, B. (1985). Hydraulic and acoustic properties as a function of porosity in Fontainebleau Sandstone. *J. Geophys. Res.* 90, 11524–11532. doi: 10.1029/JB090iB13p11524

Buades, A., Coll, B., and Morel, J. M. (2008). Nonlocal image and movie denoising. *Int. J. Comput. Vis.* 76, 123–139. doi: 10.1007/s11263-007-0052-1

Buades, A., Coll, B., and Morel, J. M. (2010). Image denoising methods. A new nonlocal principle. *SIAM Rev.* 52, 113–147. doi: 10.1137/090773908

Clavaud, J. B., Maineult, A., Zamora, M., Rasolofosaon, P., and Schlitter, C. (2008). Permeability anisotropy and its relations with porous medium structure. *J. Geophys. Res. Solid Earth* 113, 1–10. doi: 10.1029/2007JB005004

Doyen, P. M. (1988). Permeability, conductivity, and pore geometry of sandstone. *J. Geophys. Res.* 93:7729. doi: 10.1029/JB093iB07p07729

Ellis, D., and Singer, J. (2007). *Well Logging for Earth Scientists*. Dordrecht: Springer.

Fouard, C., Malandain, G., Prohaska, S., Westerhoff, M., Cassot, F., Mazel, C., et al. (2004). "Skeletonization by blocks for large 3D datasets: application to brain microcirculation," in *2004 2nd IEEE International Symposium on Biomedical Imaging: Macro to Nano (IEEE Cat No. 04EX821)* 2, 89–92. doi: 10.1109/ISBI.2004.1398481

Ghanbarzadeh, S., Hesse, M. A., and Prodanović, M. (2015). A level set method for materials with texturally equilibrated pores. *J. Comput. Phys.* 297, 480–494. doi: 10.1016/j.jcp.2015.05.023

Gomez, C. T., Dvorkin, J., and Vanorio, T. (2010). Laboratory measurements of porosity, permeability, resistivity, and velocity on Fontainebleau sandstones. *Geophysics* 75:E191. doi: 10.1190/1.3493633

Haralick, R. M., and Shapiro, L. G. (1985). Image segmentation techniques. *Comput. Vis. Graph. Image Process.* 29, 100–132. doi: 10.1016/S0734-189X(85)90153-7

Hier-Majumder, S. (2014). Melt redistribution by pulsed compaction within ultralow velocity zones. *Phys. Earth and Planet. Int.* 229, 134–143. doi: 10.1016/j.pepi.2014.01.004

Hier-Majumder, S., and Revenaugh, J. (2010). Relationship between the viscosity and topography of the ultralow-velocity zone near the core-mantle boundary. *Earth Planet. Sci. Lett.* 299, 382–386. doi: 10.1016/j.epsl.2010.09.018

Hier-majumder, S., and Tauzin, B. (2017). Pervasive upper mantle melting beneath the western US. *Earth Planet. Sci. Lett.* 463, 25–35. doi: 10.1016/j.epsl.2016.12.041

Kaestner, A., Lehmann, E., and Stampanoni, M. (2008). Imaging and image processing in porous media research. *Adv. Water Resour.* 31, 1174–1187. doi: 10.1016/j.advwatres.2008.01.022

Lindquist, W., Venkatarangan, A., Dunsmuir, J., and Wong, T. (2000). Pore and throat size distributions measured from synchrotron X-ray tomographic images. *J. Geophys. Res. Solid Earth* 105, 21509–21527. doi: 10.1029/2000JB900208

Madonna, C., Quintal, B., Frehner, M., Almqvist, B. S. G., Tisato, N., Pistone, M., et al. (2013). Synchrotron-based X-ray tomographic microscopy for rock physics investigations. *Geophysics* 78, D53–D64. doi: 10.1190/geo2012-0113.1

Marone, F., Hintermuller, C., McDonald, S., Abela, R., Mikuljan, G., Isenegger, A., et al. (2009). X-ray tomographic microscopy at TOMCAT. *J. Phys. Conf. Ser.* 186, 5–8. doi: 10.1088/1742-6596/186/1/012042

Miller, K. J., Montési, L. G., and Zhu, W.-l. (2015). Estimates of olivine-basaltic melt electrical conductivity using a digital rock physics

approach. *Earth Planet. Sci. Lett.* 432, 332–341. doi: 10.1016/j.epsl.2015.10.004

Peyman, M., and Apostolos, K. (2017). "SPE-185720-MS DyMAS: a direct multi-scale pore-level simulation approach," in *SPE Western Regional Meeting* (Society of Petroleum Engineers), 1–15

Revil, A., Kessouri, P., and Torres-Verdín, C. (2014). Electrical conductivity, induced polarization, and permeability of the Fontainebleau sandstone. *Geophysics* 79, D301–D318. doi: 10.1190/geo2014-0036.1

Rider, M., and Kennedy, M. (2011). *The Geological Interpretation of Well Logs*. Rider-French.

Saxena, N., Hofmann, R., Alpak, F. O., Dietderich, J., Hunter, S., and Day-Stirrat, R. J. (2017). Effect of image segmentation & voxel size on micro-CT computed effective transport & elastic properties. *Mar. Petrol. Geol.* 86, 972–990. doi: 10.1016/j.marpetgeo.2017.07.004

Sharqawy, M. H. (2016). Construction of pore network models for Berea and Fontainebleau sandstones using non-linear programing and optimization techniques. *Adv. Water Resour.* 98, 198–210. doi: 10.1016/j.advwatres.2016.10.023

Stampanoni, M., Groso, A., Isenegger, A., Mikuljan, G., Chen, Q., Bertrand, A., et al. (2006). *Trends in Synchrotron-Based Tomographic Imaging: The SLS Experience*. International Society for Optics and Photonics.

Thomson, P.-R., Aituar-Zhakupova, A., and Hier-Majumder, S. (2018a). Pore Network Modeling Data for Fontainebleau and Berea Sandstones. *Zenodo* 25:1184144. doi: 10.5281/zenodo.1184144

Thomson, P.-R., Aituar-Zhakupova, A., and Hier-Majumder, S. (2018b). *Segmented Image Data for Fontainebleau and Berea Sandstones*. Zenodo. Available online at: https://figshare.com/articles/Segmented_Image_Data_for_Fontainebleau_and_Berea_Sandstones/6154811

Von Bargen, N. and Waff, H. S. (1986). Permeabilities, interfacial areas and curvatures of partially molten systems: results of numerical computations of equilibrium microstructures. *J. Geophys. Res.* 91, 9261–9276. doi: 10.1029/JB091iB09p09261

Wimert, J., and Hier-Majumder, S. (2012). A three-dimensional microgeodynamic model of melt geometry in the Earth's deep interior. *J. Geophys. Res.* 117:B04203. doi: 10.1029/2011JB009012

Wright, H. M., Roberts, J. J., and Cashman, K. V. (2006). Permeability of anisotropic tube pumice: model calculations and measurements. *Geophys. Res. Lett.* 33, 2–7. doi: 10.1029/2006GL027224

Yale, D. (1984). *Network Modeling of Flow, Storage, and Deformation in Porous Rocks*. Ph.D. thesis, Stanford University.

Yoshino, T., Takei, Y., Wark, D. A., and Watson, E. B. (2005). Grain boundary wetness of texturally equilibrated rocks, with implications for seismic properties of the upper mantle. *J. Geophys. Res. B Solid Earth* 110, 1–16. doi: 10.1029/2004JB003544

Youssef, S., Rosenberg, E., Gland, N., Kenter, J., Skalinski, M., and Vizika, O. (2007). "High resolution CT and pore-network models to assess petrophyscial properties of homogeneous and heterogeneous carbonates," in *PE/EAGE Reservoir Characterization and Simulation Conference* (Society of Petroleum Engineers).

Conflict of Interest Statement: The authors declare that the research was conducted in the absence of any commercial or financial relationships that could be construed as a potential conflict of interest.

Chapter 4

The Influence of Microporous Cements on the Pore Network Geometry of Natural Sedimentary Rocks

Description. This chapter is presented in manuscript format and is published in Earth and Planetary Materials, a section of the journal Frontiers in Earth Science. This paper investigates the influence of the microporosity on the pore network of 3 sandstones and 3 limestone samples. At the resolution of micro CT images, it remains challenging to accurately identify and quantify microporosity. However, the presence of this phase can provide an insight into the nature of fluid flow through the pore network of different rocks. Two end-member models are generated to assess the influence of microporous phases before and after cementation. Before cementation, the microporous phase is considered part of the total pore network and fully permits fluid flow. After cementation, the microporous phase is considered impermeable and forms part of the rock matrix, meaning fluid flow is only permitted through the macropore network. By using this method, it is demonstrated that the fraction of connected pores and permeability decrease sharply with microporous cement volume fraction and eventually the connectivity of the macropore network is cut-off around 4% cement volume fraction.

Author contribution. Paul-Ross Thomson performed most of the image filtering and segmentation, conducted the image analysis, interpreted the data, generated most figures and wrote most of the manuscript.

Reference. Thomson, P.R., Hazel, A. and Hier-Majumder, S., 2019. The Influence of Microporous Cements on the Pore Network Geometry of Natural Sedimentary Rocks. Front. Earth Sci, 7, p.48.

frontiers in Earth Science

ORIGINAL RESEARCH
published: 22 March 2019
doi: 10.3389/feart.2019.00048

The Influence of Microporous Cements on the Pore Network Geometry of Natural Sedimentary Rocks

*Paul-Ross Thomson, Alexander Hazel and Saswata Hier-Majumder**

Department of Earth Sciences, Royal Holloway University of London, Egham, United Kingdom

We investigate the pore network geometry and permeability of six natural sandstones and carbonate rocks. Using 3D microtomographic images, we segment each rock sample into three phases: Solid matrix of grains, macropores containing void spaces, and a third microporous phase containing nanometer-sized pores beyond the resolution of the image. In the majority of our samples, the microporosity exists inside cements deposited as a secondary phase along the surface of grains. Within the macropores, the pore radius, coordination number, throat radius, and throat length display a power law relation with porosity. We also find that the permeability of the aggregate depends on the porosity following the relation $k = k_0\phi^{3.32}$, where $\log k_0 = 5.52$ (mD). The fraction of connected porosity shows a strongly non-linear reduction with an increase in the volume fraction of microporous cement.

Keywords: digital rock physics, porosity, sandstone, microfluid, petrophysics, micro CT, carbonate

OPEN ACCESS

Edited by:
Alejandro Fernandez-Martinez, Centre National de la Recherche Scientifique (CNRS), France

Reviewed by:
Qinhong Hu, University of Texas at Arlington, United States
Martin Charles Wilding, Sheffield Hallam University, United Kingdom

****Correspondence:***
Saswata Hier-Majumder
saswata.hier-majumder@rhul.ac.uk

Specialty section:
This article was submitted to Earth and Planetary Materials, a section of the journal Frontiers in Earth Science

Received: *10 December 2018*
Accepted: *28 February 2019*
Published: *22 March 2019*

Citation:
Thomson P-R, Hazel A and Hier-Majumder S (2019) The Influence of Microporous Cements on the Pore Network Geometry of Natural Sedimentary Rocks. Front. Earth Sci. 7:48. doi: 10.3389/feart.2019.00048

1. INTRODUCTION

Carbonates and sandstones form important reservoirs for hydrocarbons and can act as potential sinks for the future storage of anthropogenic green-house gases by carbon capture and sequestration. The nature of the pore space in these rock types can be complex, often resulting from a combination of depositional and diagenetic processes. The pore geometry of carbonates is commonly more tortuous due to millimeter scale macroporosity, which may include interparticle, intercrystal, moldic and vuggy porosity (Choquette and Pray, 1970), and microporosity (submicron porosity), typically intraparticle, including partially dissolved bioclastic and/or grain material, and cementation found along the pore and throat grain contacts. Clean sandstones display a simplistic pore geometry, with macroporosity forming a more uniform intergranular network and microporosity forming from detrital and authigenic clays (Pittman, 1979). "Tight" (low porosity) sandstones, however, can demonstrate characteristics that lead to a more complicated pore network. Such features include variable grain size, grain packing, sorting, clay distribution and after burial compaction (Marquez et al., 2014; Teles et al., 2016). Additionally, primary pore geometry in these sandstones can be reduced by cementation, rendering them "tight." Consequently, determination of petrophysical properties of these sandstones are often as challenging as carbonate rocks.

Conventional relationships used to predict petrophysical properties are restricted by the presence of microporosity found in many carbonates and tight sandstones. Such relationships include Archie's law for resistivity, the Carman–Kozeny permeability estimate and the

Brooks–Corey parameterization of relative permeability, which were all originally designed for more simplistic rocks with intergranular pores. When considering these classic models for complex carbonates and tight sandstones, the results are inaccurate due to the greater range in pore-size distributions and interconnectivity of different pore types (Jennings and Jerry Lucia, 2003).

The use of X-ray computed microtomography (micro CT), high resolution, three-dimensional (3D) images of porous geological media have become greatly popular over the past two decades (Valvatne and Blunt, 2004; Andrä et al., 2013a,b; Madonna et al., 2013; Prodanović et al., 2014; Bultreys et al., 2016a). This non-invasive technique allows 3D pore geometries to be evaluated quantitatively, whilst preserving the integrity of the original sample. The other great advantage of a digitized pore space network reconstruction is the ability to simulate a multitude of different transport properties. Porous flow, in particular, has several applications to many important geological fields, including hydrology, the recovery of oil and gas, and carbon sequestration. Recent studies related to the storage of anthropogenic CO_2 in the subsurface highlight the *in situ* process of dissolution and its effects on porosity and permeability of different carbonates by means of experiment performed with lab-based micro CT scanner visualization (Menke et al., 2015, 2016). Numerical models of single and multiphase fluid flow have also been used to predict absolute and relative permeability for a variety of different rock type. The use of traditional computation fluid dynamics, which incorporates finite difference, finite volume and finite element (Mostaghimi et al., 2013; Raeini et al., 2014), and the lattice-Boltzmann method (Ramstad et al., 2010; Shah et al., 2016) have proven popular in recent years. For more detail on the use of micro CT and its applications to geoscience, the reader is referred to a number of recent review papers (Cnudde and Boone, 2013; Bultreys et al., 2016a; Berg et al., 2017).

Other studies have shown that micro CT can provide useful insights into the key processes occurring at the pore scale within unconventional resources such as shale oil and shale gas. Ma et al. (2016) successfully combined micro CT and scanning electron microscopy (SEM) to identify and quantify four different types of porosity within the Bowland Shale, UK. Their results indicated that porosity was unconnected at scales greater than 20 nm, whilst organic matter and clay minerals at scales of less than 20 nm was found to be connected and offered potential diffusion transport pathways for gas. A similar study by Saif et al. (2017) on the Green River oil shale (USA) highlighted the evolution of an interconnected fracture network and increased porosity due to the breakdown of kerogen into hydrocarbon fluids during pyrolysis. Such insights are powerful tools which can be used to estimate the petrophysical properties of many rocks for modeling and designing production processes.

Microporosity typically exists at a resolution below that from which clear segmentation can not be achieved. This results in an intermediate phase, that can neither be assigned to void space nor solid in conventional micro CT. To accurately visualize and represent microporosity in 3D it is possible to combine SEM with various reconstruction techniques (Øren and Bakke, 2003; Okabe and Blunt, 2005), or more recently, with the use of focused ion beam scanning electron microscopy (FIB-SEM) (Bera et al., 2011; Jiao et al., 2014). The variation in pore sizes between micro and macroporosity means that not all pores can be incorporated in one single imaging experiment. It remains challenging to combine data from multiple experiments because the necessary resolution of such a model is influenced by the finest pores, while the minimal size of the model is controlled by the representative elementary volume of the sample (Bultreys et al., 2016a). The joint modeling of such different scales results in a difference of several orders of magnitude, which often presents computational limitations. The use of a pore network model (PNM) reduces the computational expense, which at present are probably the best suited technique for dual scale porosity simulations (Jiang et al., 2012, 2013; Mehmani and Prodanović, 2014; Bultreys et al., 2015).

Despite the challenges in identifying and quantifying microporosity, their presence can provide an insight into the nature of fluid flow through a connected, intergranular macroporous network. In this article, we distinguish microporosity arising from two different sources: microporosity in primary rock-forming grains and microporosity within secondary phases. An example of the former includes fossils in carbonate rocks while an example of the latter includes microporous cement deposited as secondary phases along the walls of a pore network. Recent work by Bultreys et al. (2015) discussed the effective transport properties combining imaged macroporosity and models of microporosity. We refer the reader to this work for physical properties involving microporosity and focus on (a) the pore network geometry of the connected macro pore space, macroporosity, and (b) the way development of secondary microporosity, or cement, affect the connectivity of the primary porosity.

We segment and analyze the micro CT images of six natural sandstones and carbonates into three phases (microporosity, macroporosity and matrix) to quantify their volume fraction and to evaluate the nature of their pores and throats using pore network models. We further analyze each rock type by selecting one or more smaller regions of interest (ROI) to assess sample heterogeneity and perform error analysis. We compare the results between three different sandstones, the Doddington, Knorringfjellet, and Wilcox, and three different carbonates, the Estaillades, Massangis Jaune, and Savonnières. The characteristics of the raw data for all six samples is summarized in **Table 1**.

2. METHODS

All data used in this work was sourced externally. The Doddington and Wilcox sandstone data sets were acquired online from the British Geological Society's (BGS) National Geoscience Data Centre (Shah et al., 2016) and the Digital Rocks Portal (Mehmani and Prodanović, 2014; Prodanović et al., 2014), respectively. Images for the Knorringfjellet sandstone and three

TABLE 1 | Characteristics of raw data.

Sample	Raw volume (voxels)	Volume used in study (voxels)	Voxel size
Doddington	576×596×590	325×325×500	$(6.4\ \mu m)^3$
Knorringfjellet	1,600×1,600×1,726	950×950×1,600	$(2.8\ \mu m)^3$
Wilcox	924×915×910	500×500×600	$(2.7\ \mu m)^3$
Estaillades	2,000×2,000×1,725	600×600×700	$(3.1\ \mu m)^3$
Massangis Jaune	912×910×634	440×460×630	$(4.5\ \mu m)^3$
Savonnières	1020×968×1680	600×600×700	$(3.8\ \mu m)^3$

carbonate samples, Estaillades, Massangis Jaune (Boone et al., 2014), and Savonnières were kindly provided by Tom Bultreys (Bultreys et al., 2016b) (Imperial College London).

We filtered the gray scale images to reduce noise and remove unwanted artifacts. We then segmented the filtered image into microporosity, macroporosity and matrix by thresholding. Next, we analyzed the proportion of microporosity and macroporosity in each sample, using a series of ROI to assess the influence of sample heterogeneity. Pore network modeling and absolute permeability simulations were then carried out to characterize the nature of the pore geometries in all samples and to quantify the effect of microporosity on single phase fluid flow. We used the commercial software PerGeos, from Thermo Fisher Scientific, to prepare images, to perform network modeling, and to simulate fluid flow through the segmented 3D images.

2.1. Image Processing

We filtered the micro CT images to reduce spurious features that occur from the image acquisition process (Ketcham and Carlson, 2001; Wildenschild et al., 2002) and to amplify the contrast between key phases. Firstly, we extracted a subvolume from the original raw data for computational efficiency in filtering and simulations at a later stage. The sub volume characteristics are highlighted in **Table 1**. Next, we applied various filters including anisotropic diffusion, non-local means, and despeckle to reduce salt and pepper noise at the center of grains, whilst maintaining detail at the boundaries between pores and solid matrix.

The process of segmentation in micro CT images is a crucial step which can induce operator bias and subsequently affect the quality of all other image analyses (Wildenschild and Sheppard, 2013; Schlüter et al., 2014). A wide variety of segmentation techniques exist, which can broadly be separated into two groups. Global thresholding includes all methods where labels are assigned to voxels by histogram evaluation only, without thought for how the gray values are spatially arranged in the image. Such techniques have been reviewed extensively in the past by many authors (Pal and Pal, 1993; Trier and Jain, 1995; Sezgin and Sankur, 2004; Iassonov et al., 2009), only to conclude that none of the methods are particularly good for all segmentation challenges. Local segmentation techniques make up the other popular class and these take account of neighborhood statistics enabling smoother boundaries, avoidance of noise objects, and compensation for local intensity changes. This greater flexibility and often more satisfying segmentation results is what differentiates the local segmentation methods from global thresholding (Iassonov et al., 2009; Wang et al., 2011).

In this work we used manual thresholding to segment the volume into three phases: microporosity, macroporosity and matrix. Whilst the classification for labeling the macroporosity and matrix were fairly simple, the microporosity existed as an intermediate phase, which created a more challenging interpretation. This intermediate phase included voxels of a particular gray scale that could often be identified in contact with macroporosity at the edges of grains (cementation), and sometimes occurring as whole or part of grains. This observation suggests that some microporosity exists as partially dissolved grains and/or bioclastic material in most of the samples. Although our chosen technique was user dependent and was likely to result in a certain degree of uncertainty, we manually adjusted the thresholds to produce results that we considered visually correct. To further reduce this uncertainty we benchmarked our results where possible with those found in previous studies (Boone et al., 2014; Derluyn et al., 2014; Mehmani and Prodanović, 2014; Alyafei and Blunt, 2016; Bultreys et al., 2016b). The micrographs in **Figure 1** show the segmented gray scale images from the six samples analyzed in this study.

2.2. Pore Network Model (PNM)

Following segmentation, pore-based PNM are extracted using a hybrid method described in Youssef et al. (2007). This method employs a medial-axis algorithm guided by a distance map which progressively erodes the pore-grain interface until a one-voxel thick skeleton of the entire pore space is achieved. The algorithm then calculates the length and connectivity of each line and designates each one as either pore or throat based on a known extreme radius. The intersection between two or more lines is marked as a node. A segment of the skeleton is marked as a pore if the extreme radius of the segment is larger than its length, whilst throats are classified as segments with length that do not exceed their extreme radius. The subsequent expansion of the one-voxel thick skeleton in these pores and throats allows the calculation of the radius of sphere (able to fit in each pore) and the length and equivalent hydraulic radius of each throat. The output of this algorithm results in the coordination number (number of throats connected to each pore), radius, area and volume of every pore, and the radius and length of each throat.

We test a simple model to evaluate the effects of microporosity on the pore geometry using two different scenarios. Initially, we generate the PNM using only the connected pore space (where possible) of macroporosity. Following this, we generate a second PNM where we assume that microporosity is made up of 100% void space, thus describing the pore network prior to cementation. To do this, we simply created a separate binary image for the total porosity case which incorporated both the microporosity and macroporosity. In samples where microporosity occurs within the cement, this step allows us to compare the reduction of pore connectivity and permeability due to cementation. All PNM simulations reported here are derived only from the macropores. The PNM analysis of micropores is an interesting topic for research involving high resolution nano-CT.

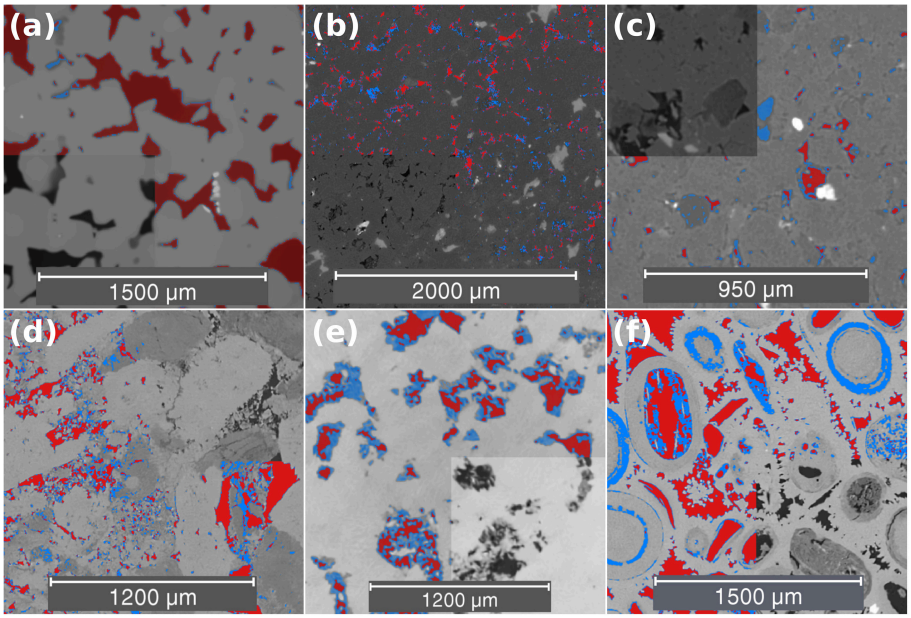

FIGURE 1 | From top, left to right: **(a)** Doddington sandstone, **(b)** Knorringfjellet sandstone, **(c)** Wilcox sandstone, **(d)** Estaillades limestone, **(e)** Massangis Jaune limestone, and **(f)** Savonnières limestone. Single slice view of each sample. A quarter of the image is represented in gray scale only. The remaining voxels display macroporosity in red, and microporosity in blue.

2.2.1. Porosity

Using the smaller sub-sampled volumes of each rock, we generated new label fields for microporosity and macroporosity in each volume. Microporosity was assigned to the voxels deemed to be associated with the primary rock-forming material (e.g., fossils in carbonates that may have been affected by secondary dissolution) and cement phases found along the walls of the pores. Typically these phases appear as a lighter shade of gray compared to macroporosity. The macroporosity was assigned with much less difficulty based on a dark black or gray color (**Figure 1**). The volume fraction of porosity was calculated in each of these by measuring the number of voxels assigned to the void space, compared to those making up the remaining background voxels in each sub-sample. The macroporosity and microporosity proportion was calculated for each of the different samples by using the phase segmented data and calculating the volume of the total number of macroporosity and microporosity voxels to the total number of voxels in the complete sample. The total porosity was simply calculated by adding the macroporosity and microporosity. The volumes used for the calculations of the entire sample are highlighted in **Table 1**, whilst the volume fraction of porosity is summarized in **Table 2**.

We took the porosity analysis a step further and separated each sample down into further divisions to assess the heterogeneity at this scale. All samples were subsampled along the Z-axis into divisions of three, with the exception of the Knorringfjellet sandstone (8 subvolumes). **Figure 2** shows a volume rendering representation of each sample and their subdivisions. The data from this analysis is summarized in the **Supplementary Material**.

It is important to note that microfractures can contribute toward the connectivity of pores in many rocks. These microfractures may be natural or induced during the sample preparation stage. With the images used in this study we found no evidence to suggest the presence of microfractures, so focus on the primary porosity that can be observed in all images. The connectivity of the macroporosity in each subsample volume was assessed along the Z-axis. Volumes found to have a connected network that passes a percolation threshold from top to bottom were classified as having a connected porosity. Voxels that belong to the initial porosity but do not make up part of the connected network are determined as isolated pores and are removed from the resulting binary image. To fully evaluate the heterogeneity of each rock we generated a combined (microporosity and macroporosity) label field to test the total porosity case and assess whether or not the microporosity had any effect on the connectivity of each sub-sample volume.

2.2.2. Permeability Simulation

We performed absolute permeability simulations on each rock to calculate the flow of fluid directly through the connected pore space of the 3D micro CT images. We used a finite volume solver in the petrophysics module of PerGeos to calculate the flow of water given by Stokes equation,

$$\nabla \cdot \boldsymbol{u} = 0, \tag{1}$$

$$-\nabla P + \mu \nabla^2 \boldsymbol{u} = 0, \tag{2}$$

where $\boldsymbol{u}$ is the fluid velocity vector, P is the pressure and $\mu = 1 \times 10^{-3}$ Pa.s is viscosity of water. Each simulation was set up with

TABLE 2 | Volume fraction of total porosity (ϕ_T), macroporosity (ϕ_M), microporosity (ϕ_m), total connected porosity (ϕ_{T_C}), connected macroporosity (ϕ_{M_C}), and connected microporosity (ϕ_{m_C}) of total smple volumes.

Sample	Total porosity ϕ_T (%)	Macro porosity ϕ_M (%)	Micro porosity ϕ_m (%)	Total connected porosity ϕ_{T_C} (%)	Connected macro porosity ϕ_{M_C} (%)	Connected micro porosity ϕ_{m_C} (%)
Doddington	18.6	16.7	1.9	18.5	16.6	0
Knorringfjellet	7.7	4.3	3.4	6.1	1.2	2.7
Wilcox	7.1	3.2	3.9	0	0	0
Estaillades	19.1	11.7	7.4	18.4	10.8	6.9
Massangis Jaune	16.1	4.9	11.2	15	0	10.4
Savonnières	32.5	20.9	11.6	28.8	17	9.9

Analysis performed on volumes described in ***Table 1****.*

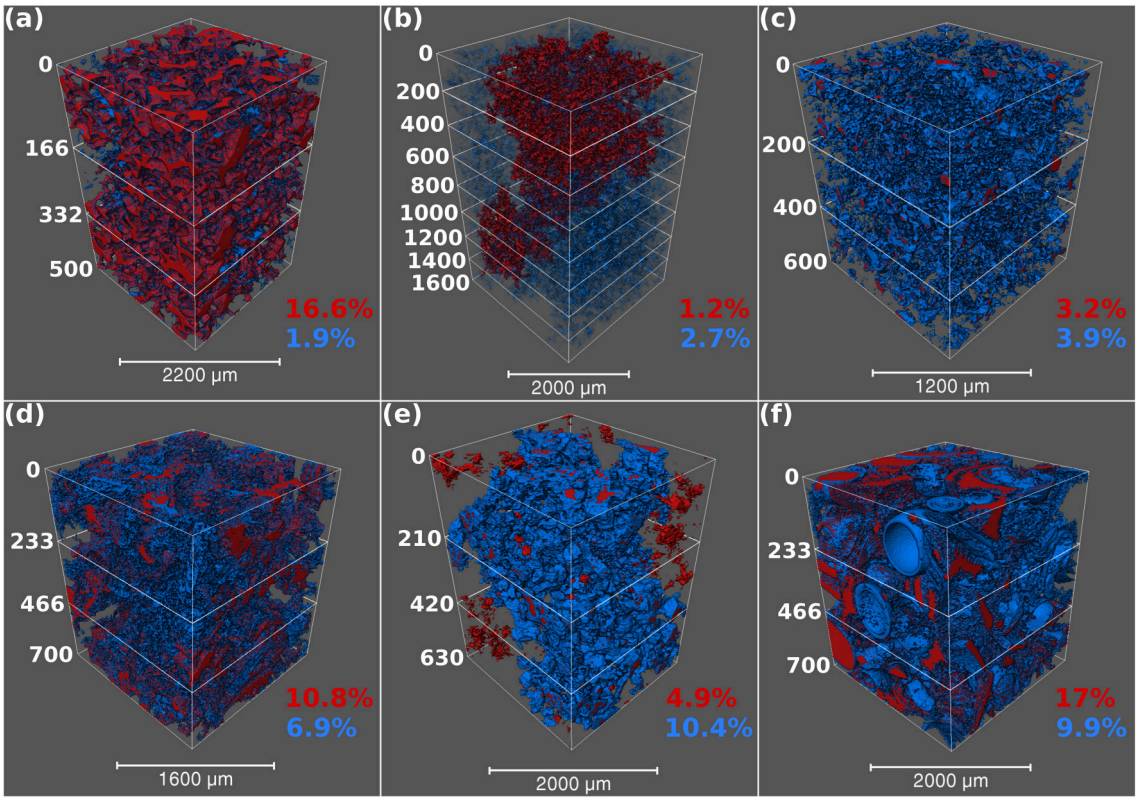

FIGURE 2 | Volume rendering visualization of the six different samples. From top, left to right: **(a)** Doddington sandstone showing connected macroporosity and total microporosity, **(b)** Knorringfjellet sandstone showing connected macroporosity and connected microporosity, **(c)** Wilcox sandstone showing total macroporosity and total microporosity, **(d)** Estaillades limestone showing connected macroporosity and connected microporosity, **(e)** Massangis Jaune limestone showing total macroporosity and connected microporosity, and **(f)** Savonnières limestone showing connected macroporosity and connected microporosity. For each volume the macroporosity is shown in red and microporosity in blue. **Table 2** summarizes the volume fractions of porosity observed in all samples. Subdivisions are also shown here, from which the subvolume porosity analysis was performed.

a series of specified boundary conditions described in Thomson et al. (2018). Parameters were kept constant for all simulations, with the exception of the 3D micro CT input image.

We carried out numerical simulations on the connected pore network derived from both the total pore space and the macro pore space for all samples except for the Wilcox sandstone and Massangis Jaune carbonate. In the former, a connected pore network could not be established using the method described above. In the latter, a connected network was absent in macropores, but existed in micropore and total pore space. Samples in which micropores occur within the cement phase, we define the normalized permeability $k^* = k_M/k_T$, where k_M is the permeability derived from the macro pore network and k_T is the permeability derived from the total pore space (e.g., both macro and micro pores combined together). In section 4 we show the variations in k^* with cement volume fraction (volume fraction of micropores).

We first carried out permeability simulations in samples with a connected porosity across the entire volume, evaluating both k_M and k_T, to assess the changes to permeability with the addition of

microporosity permitting total flow. Next, we followed a similar approach to assess the influence of heterogeneity within the microtomographic images. We selected small regions of interest in each volume along their Z-axis. Each subvolume was 200 slices (voxels) in length. We then calculated the total porosity and connected porosity, when possible, in each sub-sample. Volumes found to have connected porosity were used to simulate permeability. Variations in porosity within the small subvolumes are shown in **Figures 3B,D** for Doddington and Knoringfjellet sandstones.

The numerical value of permeability, determined from the simulations, depends strongly on the convergence criterion for the simulation. The convergence criterion or error, ϵ, is defined as the maximum change in the value of an unknown variable (e.g., velocity and pressure) per time step. Equations (1) and (2) describe a steady-state, i.e., the calculates values of x, y, and z components of velocity and pressure should not change on subsequent iterations. As a result, we can define,

$$\epsilon = max\left(\frac{v_x(n) - v_x(n-1)}{\delta t}, \frac{v_y(n) - v_y(n-1)}{\delta t}, \frac{v_z(n) - v_z(n-1)}{\delta t}, \frac{P(n) - P(n-1)}{c^2 \delta t}\right) \tag{3}$$

where n is the current iteration, v_i are components of the velocity vector, P is the pressure, t is the time step and c^2 is a compressibility coefficient used in the simulation.

We carried out a series of numerical experiments (**Figures 3A,C**), by terminating the simulations when a prescribed value of ϵ is reached. The results in **Figures 3A,C)** show the sensitivity of the permeability to the value of ϵ. While a high value of ϵ, such as 10^{-3}, reduces the computation time, the computed permeability is significantly higher than those obtained for a lower value of ϵ. For example, in **Figures 3A,C**, the calculated permeability remained nearly constant for $\epsilon \leq 10^{-5}$. After performing this initial series of sensitivity tests on Doddington and Knoringfjellet sandstones, we set the value of ϵ between 10^{-5} and 10^{-6} for the remaining permeability simulations.

3. RESULTS

For each sample we compare the porosity, PNM characteristics and permeability. We show the total porosity, the proportion of macroporosity and microporosity, and the volume of connected (effective) porosity for each of these. The PNM attributes highlight the variation in the characteristics of pores and throats. Lastly, we compare the results of permeability simulations using a macroporosity only model and a total porosity (micro and macro) model through the samples.

3.1. Porosity Analysis

The Doddington and Knorringfjellet sandstones are both potential CO_2 sequestration target reservoirs with quite different porosity characteristics. The Doddington sandstone has a higher total porosity of 18.6%, which is largely shared by macroporosity, contributing to 89.8% of the pore space, whilst only a small fraction of microporosity makes up the remaining network. Overall, the Doddington sandstone has good effective porosity with total connected porosity at 18.5% and connected macroporosity at 16.6%. Conversely, the Knorringfjellet sandstone has a much lower total porosity of 7.7%. The macroporosity and microporosity in this sample are 4.3 and 3.4%, respectively, indicating that the microporosity occupies a larger proportion (44.2%) of the total pore network compared to that observed in the Doddington sandstone (10.2%). The total connected porosity observed in the Knorringfjellet sandstone is 20% reduced compared to its overall total porosity, significantly more compared to that seen in the Doddington sandstone.

The unconventional Wilcox sandstone is a tight gas target with similar porosity characteristics to the Knorringfjellet sandstone. The Wilcox also has a low total porosity of only 7.1%, separated by 3.2% macroporosity and 3.9% microporosity. In this sample the microporosity contributes toward 54.9% of the total pore space, providing the highest proportion of microporosity observed in all the sandstone samples that we analyzed. As indicated in the data in **Table 2**, we failed to detect an interconnected pore network in this sample.

The Doddington sandstone shows very minimal variation across the three volumes with a range in total porosity from 18 to 19.2%. The total porosity is reduced by an average of 0.7% when assessing the connectivity of the total pore volume. The Knorringfjellet sandstone however, shows greater variation across the eight volumes that were analyzed. This sample has a range in total porosity from 7 to 8.8%, whilst the proportion of connected total porosity is reduced by 20% on average. The Wilcox sandstone follows a similar trend with increasing heterogeneity. This sample has a total porosity range from 6.6 to 7.4%, and a significant reduction in the proportion of the total porosity when considering the connectivity of the network. On average, the total connected porosity is reduced by 66%. Interestingly, this is only observed in the sub-volume analysis, whilst zero connected porosity was identified using the whole volume.

The three limestone samples are from outcrop in France. The Estaillades limestone has a total porosity of 19.1%, which is largely occupied by macroporosity, 61.3% of the total pore volume. The microporosity makes up only 7.4% of the total sample volume, the lowest proportion observed in all three of the carbonates analyzed. The connectivity of the total porosity is high, with only a 3.7% reduction compared to the total pore volume. The Massangis Jaune carbonate has the lowest total porosity of all three carbonates, with 16.1% total pore volume. Of this, the macroporosity makes up only 30.4%, the lowest proportion observed in the carbonates. This sample is also the only one to have a microporosity fraction that exceeds that of the macroporosity. The total porosity is well-connected, with microporosity seemingly contributing almost entirely toward this. The complete absence of connectivity in macroporosity supports this observation. The Savonnières carbonate is composed largely of ooliths and some complete and partial shell fragments. This composition provides the highest total porosity observed in all of the samples (32.5%). The macroporosity has a 64.3% share of the total pore volume, which appears as intergranular and moldic porosity. Microporosity fulfills the remaining pore space as partially dissolved ooliths and

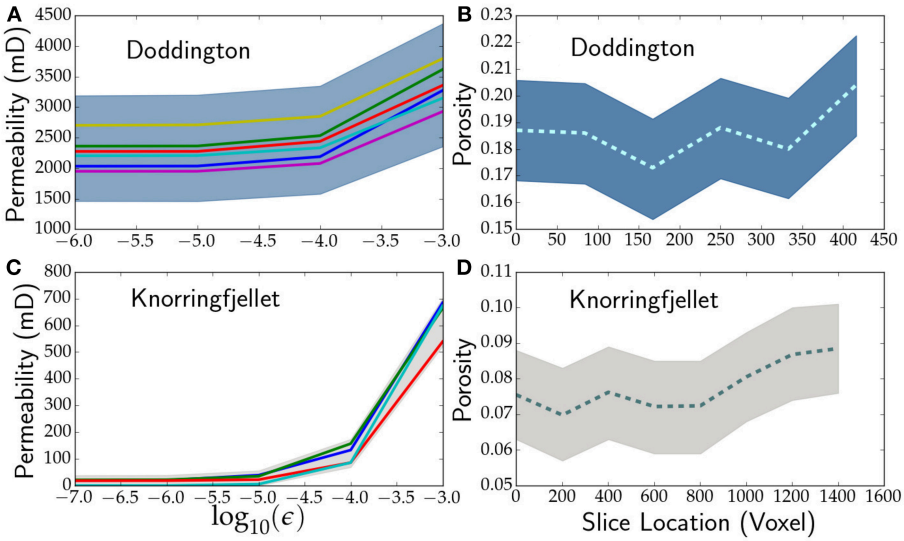

FIGURE 3 | (A) Plot of calculated permeability as a function of the residual from permeability simulations in Doddington Sandstone. **(B)** Variation of porosity measured within subvolumes of a sample of Doddington. **(C,D)** Same as in panels **(A,B)** respectively, from Knorringfjellet. The shaded region indicates the maximum and minimum values obtained from each subvolume.

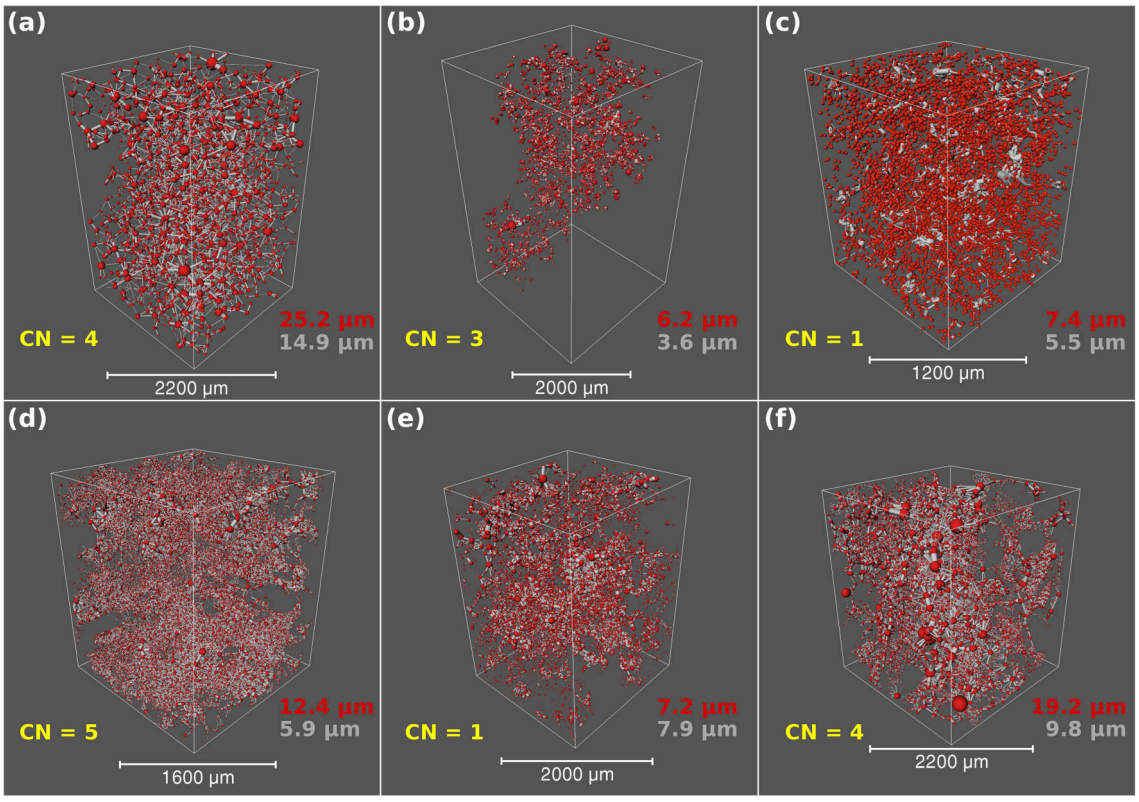

FIGURE 4 | Pore network model visualization of the six samples using the macroporosity network only. From top, left to right: **(a)** Doddington sandstone, **(b)** Knorringfjellet sandstone, **(c)** Wilcox sandstone, **(d)** Estaillades limestone, **(e)** Massangis Jaune limestone, and **(f)** Savonnières limestone. In this schematic the pores are displayed as red spheres and the throats are gray cylinders. CN = mean coordination number, whilst the red text represents the median pore radius and the gray text represents the median throat radius.

shell material. The total porosity is well-connected, represented by 28.8% of total sample volume.

The Estaillades limestone shows the widest range in total porosity, with values from 18.6 to 22.7%. This porosity is reduced by an average of 3.9% when we take the connectivity of each pore volume. This is the lowest reduction in porosity observed between the three carbonate samples. The Massangis Jaune sample had a range in total porosity from 15.2 to 17.2% across the sub-volumes. The total connected porosity was 9.7% less on average compared to the total pore volume when analyzed. This sample has a huge variation in the connectivity of the macroporosity, with a range from 47.8 to 93.8%. This is interesting as zero connected macroporosity is observed when considering the whole sample volume. The Savonnières limestone has a total porosity range from 31.7 to 33.2%. The connected proportion of this porosity is reduced by 12.6% on average.

3.2. Pore Network Model Characteristics

The PNM uses the macroporosity of each sample to generate an idealized network of pores and throats, represented by red spheres and gray cylinders, respectively (**Figure 4**). The visualizations shown in **Figures 4a–f** highlight the contrast between the nature of the pore networks when the models have been scaled to show the same characteristics (pore and throat radius).

We compare the characteristics of the macropore geometry for the three different sandstone samples: Doddington, Knorringfjellet, and Wilcox in **Figures 4a–c**. The pore network of Doddington sandstone (**Figure 4a**) is dense and well-connected, due to higher porosity and generally larger pores and throats. The mean coordination number for pores is 4, whilst the median pore radius, throat radius and throat length is 25.2, 14.9, and 158.6 μm, respectively. The pore network shown in the Knorringfjellet sandstone (**Figure 4b**) is significantly less dense, and appears to have a more isolated confined nature compared to the other two sandstones. The mean coordination number is 3, whilst the dimensions of the network in the Knorringfjellet sandstone are the smallest observed in all three sandstones, with median pore radius of 6.2 μm, throats of radius 3.6 μm and throat length of 33.8 μm. The Wilcox sandstone (**Figure 4c**) has the lowest connectivity with a mean pore coordination number of 1. The

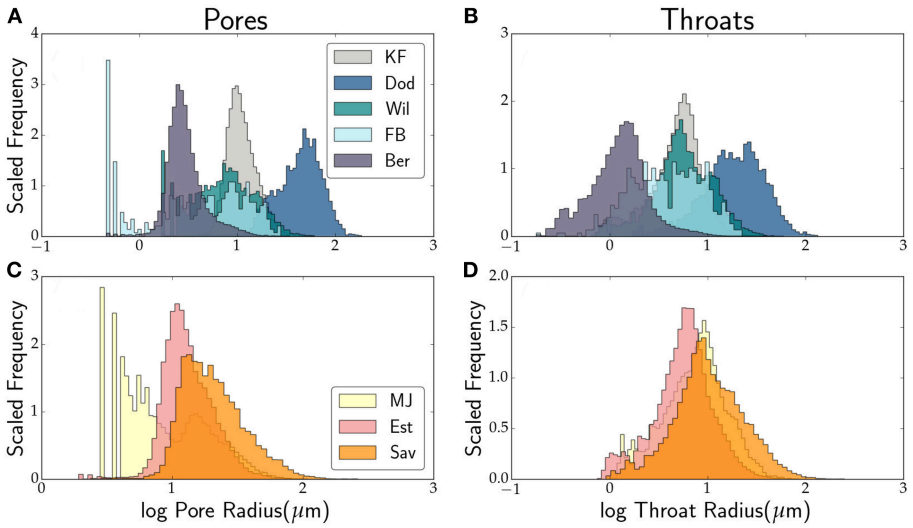

FIGURE 5 | Log normal distribution of the pore and throat geometry in sandstones **(A,B)** and limestones **(C,D)**. The left column illustrate the distribution of pore radii, while the right column displays the distribution of throat radii. Six samples from this study (KF, Knorringfjellet; Wil, Wilcox; Dod, Doddington; MJ, Massangis Jaune; Sav, Savonnières; Est, Estaillades) and two samples (FB, Fontainebleau; Ber, Berea) from Thomson et al. (2018).

TABLE 3 | Pore network model characteristics for the macroporosity and permeability results.

Sample	Coordination number	Pore radius (μm)	Throat radius (μm)	Throat length (μm)	Macro permeability K_M (mD)	Total permeability K_T (mD)
Doddington	4	25.2	14.9	158.6	3013	3725
Knorringfjellet	3	6.2	3.6	33.8	7	60
Wilcox	1	7.4	5.5	37.1	0*	0*
Estaillades	5	12.4	5.9	40.4	259	601
Massangis Jaune	1	7.2	7.9	53.4	0*	612
Savonnières	4	19.2	9.8	66.7	1408	3990

Showing mean values of coordination number, and median pore radius, throat radius, and throat length.
** Zero connected porosity to perform permeability simulation.*

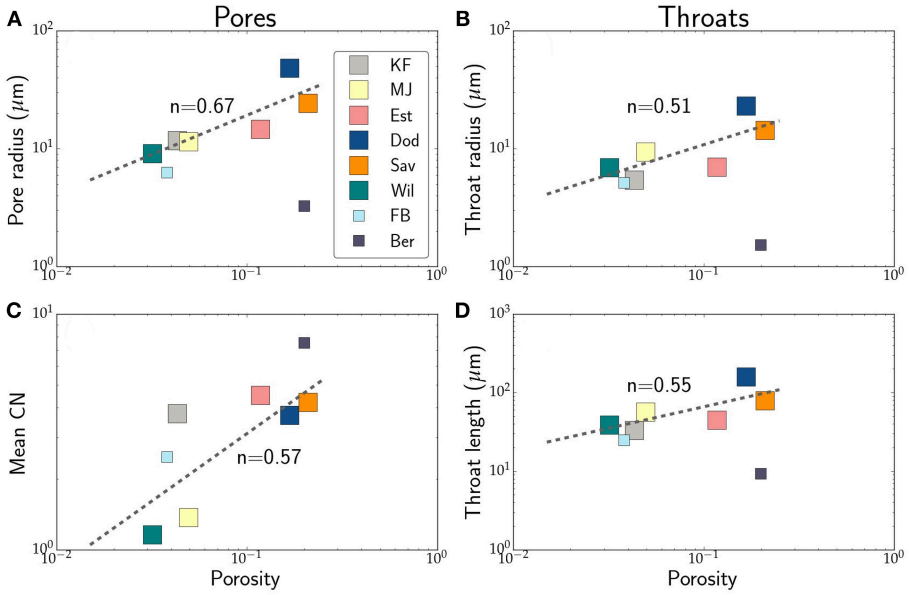

FIGURE 6 | Macropore network characteristics of the six samples from this study (KF, Knorringfjellet; Wil, Wilcox; Dod, Doddington; MJ, Massangis Jaune; Sav, Savonnières; Est, Estaillades) and 2 samples (FB, Fontainebleau; Ber, Berea) from Thomson et al. (2018). The panels display log-log plots of **(A)** pore radius, **(B)** throat radius, **(C)** mean coordination number, and **(D)** throat length as a function of macroporosity. The broken line indicates a power law fit through the six data points from this study. The power law exponent for each fit is annotated in the plot. The two samples with smaller symbol size are from higher resolution images with smaller voxel dimensions.

low connectivity of the pore network in Wilcox can be visualized in **Figure 4c** by the relatively high abundance of red, spherical pores and low abundance of gray, cylindrical throats compared to the Doddington network in **Figure 4a**, which shows a high abundance of throats connecting the pores. In Wilcox, pores have a median radius of 7.4 μm, whilst the median throat radius is 5.5 μm and the median throat length is 37.1 μm.

The macropore network characteristics of the three different carbonates: Estaillades, Massangis Jaune, and Savonnières are compared in **Figures 4d–f**. The Estaillades limestone (**Figure 4d**) has the highest density of small, gray, and cylindrical throats, reflected by a pore coordination number of 5, the highest value observed in all samples. The median pore radius, throat radius and throat length is 12.4, 5.9, and 40.4 μm, respectively. The pore geometry observed in the Massangis Jaune limestone (**Figure 4e**) is the least well-connected, highlighted by a mean pore coordination number of 1. This sample has median pore radius of 7.2 μm, median throat radius of 7.9 μm, and median throat length of 53.4 μm. The Savonnières limestone network (**Figure 4f**) also consists of high throat density, reflected by a pore coordination number of 4. The pores in Savonnières have a median radius of 19.2 μm, whilst the throats have a median radius of 9.8 μm, the highest values observed in all three carbonates. The same can be said for the median throat length, calculated at 66.7 μm.

The log normal plots in **Figure 5** show the distributions of pore and throat geometries in sandstones (**Figures 5A,B**) and carbonates (**Figures 5C,D**). We also report the mean coordination number, median pore and throat radius, and median throat length values in **Table 3**. In **Figures 5A,B**, we included published data from Fontainebleau and Berea Sandstones (Thomson et al., 2018) for comparison. The high coordination number and connectivity in the Doddington sandstone is clearly demonstrated by the peaks in the histograms in **Figures 5A,B**. The distribution of pore radius in all three carbonates in **Figure 5C** are asymmetric with a skewness toward the right. In comparison, distribution of throat radii in the carbonates in **Figure 5D** is nearly symmetric.

The main attributes of the pore network display a power law relationship with porosity. The data in these plots involve only the macroporosity. The plots shown in **Figure 6** demonstrate the relationship between porosity and pore radius, throat radius and throat length in all six samples, with the addition of two sandstones used in a similar study by Thomson et al. (2018). We also plot the porosity-coordination number relation for comparison. In the log-log plots, we overlay fits of the form $y = a\phi^n$, in each plot with the value of n annotated in the plots.

Among the PNM attributes considered here, the pore radius displays the strongest dependence on porosity. From the porosity-pore radius plot in **Figure 6A** we observe that the pore radius varies with porosity with an exponent of 2/3. Both the radius and length of the throats in panels (B) and (D) show a near square-root variation with porosity. Coordination number of the pores also increase with the porosity with an exponent of 0.57.

3.3. Absolute Permeability Simulation

We modeled the single phase flow of water directly through the pore space images of the macroporosity and total porosity

cases along the Z-axis only. Results of each simulation have been summarized in **Table 3**. In the Doddington sandstone, permeability measured through macroporosity has a value of 3,013 mD, which increases by 24% to 3,725 mD when the simulation is computed considering the total porosity. These are the highest values of permeability observed in the three sandstone samples. The Knorringfjellet sandstone shows a dramatic increase in permeability when considering the macroporosity and total porosity scenarios. The connected porosity proportion has a permeability of 7 mD. The total porosity provided a value of 60 mD, which is 760% increase compared to the macroporosity only simulation. The Wilcox sandstone has zero connected porosity when analyzing the entire volume in this study, and therefore could not be used to simulate flow. As such, no permeability measurements were acquired. The Estaillades limestone allowed flow through its macroporosity at 259 mD. Compared to the total porosity model, this value increased by 132% to 601 mD. Similarly to the Wilcox sandstone, the Massangis Jaune limestone has zero connected porosity in the macroporosity case, meaning that no permeability simulation could be modeled. However, in the total porosity case the connectivity across the Z-axis permitted flow and a permeability measure was obtained at 612 mD. The Savonnières limestone has the most efficient network for fluid flow, with a macroporosity permeability value at 1408 mD. The total porosity simulation provided an increased permeability at 3,990 mD, 183% more.

We display the combined porosity and permeability data in **Figure 7**. Where applicable, the plot displays data from both the macropore network (filled squares) and total pore network (filled circles). Also added in the plot are data from Fontainebleau and Berea sandstones from Thomson et al. (2018). We fit the data with an equation of the form $k = k_0\phi^n$. Values of both parameters are annotated in the plot. The exponent of $n = 3.32$ from our data is higher than the theoretical value of $n = 2$ of throats with a circular cross section, but is slightly lower than the value of 3.8–4.5 obtained from experimental measurements (Doyen, 1988; Bernabé et al., 2010; Revil et al., 2014).

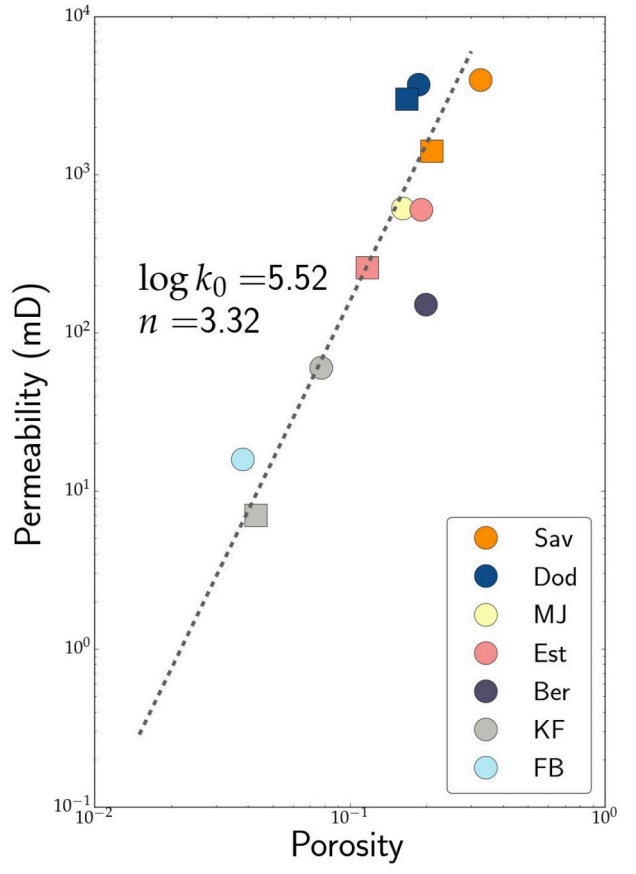

FIGURE 7 | Plot of porosity and permeability from our samples and Fontainebleau (FB) and Berea (B) sandstones from Thomson et al. (2018). Filled circles represent data from total porosity while filled squares represent data from macroporosity alone. The broken line is a fit to the data of the form $k = k_0\phi^n$. The fit parameters are annotated in the plot.

4. DISCUSSION

4.1. Micropermeability

As discussed in the introduction, dimension of the micropores in our samples are beyond the limit of detection and analysis in this study. As a result, certain assumptions must be made regarding the geometry and connectivity of micropores Bultreys et al. (2015). We chose to select two end member cases. In one case, the microporosity is considered impermeable, thus the permeability of the rock is determined only by the macroporosity. In the other case, we consider the microporosity consists essentially of void space and the effective permeability of the rock is given by the total permeability. In reality, the microporous phase may have a non-zero permeability, rendering the effective permeability somewhere between these two cases. To rigorously address the issue of micropermeability two issues need to be addressed in future work.

First, the 3D microtomographic images of the pore network can be supplemented by additional, higher resolution 3D images, possibly obtained by techniques such as FIB electron microscopic tomography. These two different scales will provide two values of permeability through the macro and micro pore spaces, which then need to be averaged using some weighting formula.

Secondly, the nature of flow through nanometer-sized pores can be fundamentally different from the classic Darcy flow model. At such small pore dimensions, the ratio between surface area to volume of pores increase substantially (Israelachvili, 1991; Chen et al., 2004), rendering surface tension at the grain-fluid interface as a strong retarding force to fluid percolation. Thus, evaluation of permeability from these pore spaces need to use a modified form of Stokes flow, taking into account the surface tension (Hier-Majumder et al., 2006; Takei and Hier-Majumder, 2009; Hier-Majumder and Abbott, 2010).

Despite these uncertainties, the end member approach taken in this study can be extremely useful in identifying the role of cementation in reducing permeability during reactive porous flow. In the following section, we discuss the implications of our results on such flows.

4.2. Effect of Cementation on Fluid Transport

Cementation during reactive porous flow leads to the deposition of secondary phases along the initially interconnected pore network, reducing the effective transport properties of the network. Using the results of our pore network models and permeability simulations, we can quantify the influence of cement volume fraction on two important parameters, the fraction of connected pore space and the ratio between permeability after and before cementation.

The 3D image of Knoringfjellet sandstone in **Figure 8** demonstrates the way cement, identified as the microporous phase, influences the pore space. The grain matrix is shown in gray scale, while the macroporosity (labeled "pore") and microporosity (labeled "cement") are identified in cyan and red, respectively. As the colored image on the right demonstrates, the cement fills up several channels essentially disconnecting the top and the bottom sections of the image. The presence of this cement has important consequences on the connectivity of the pore network.

For example, the Doddington sandstone has a total porosity of 18.6%, of which only 1.9% resides in microporosity (**Table 2**). As a result, 16.6% of the total volume of the Doddington sample resides in connected macropores. In contrast, Massangis Jaune carbonate shows a comparable total porosity of 16.1%, the majority of which (11.2% of total volume) resides in microporosity in the cement. In this sample, no connected macroporosity was detected due to cementation. The plot in **Figure 9A** plots the fraction of interconnected macropores as a function of cement volume fraction. As the plot depicts, the interconnectivity of the pore network is substantially reduced at cement volume fractions greater than 4 vol%. This result implies that the connectivity of a pore network will decline with time as precipitation occurs during reactive porous flow, until this

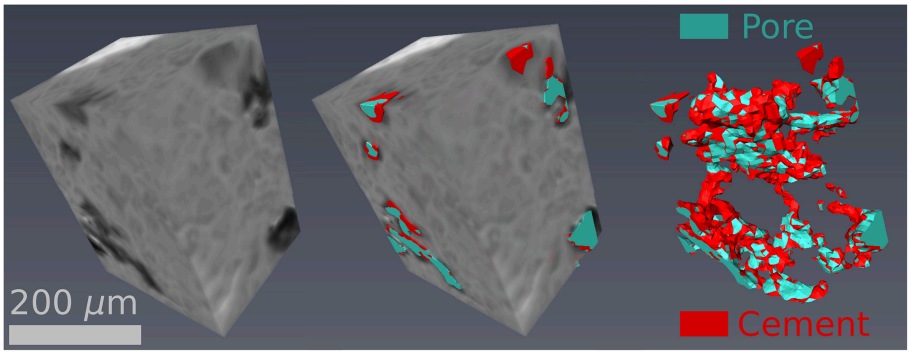

FIGURE 8 | 3D visualization of gray scale and segmented images of a subvolume in the Knorringfjellet sandstone. The micrograph in the middle overlaps the gray scale image on the segmented phases, whereas the micrograph on the right shows only the macropore and the microporous cement.

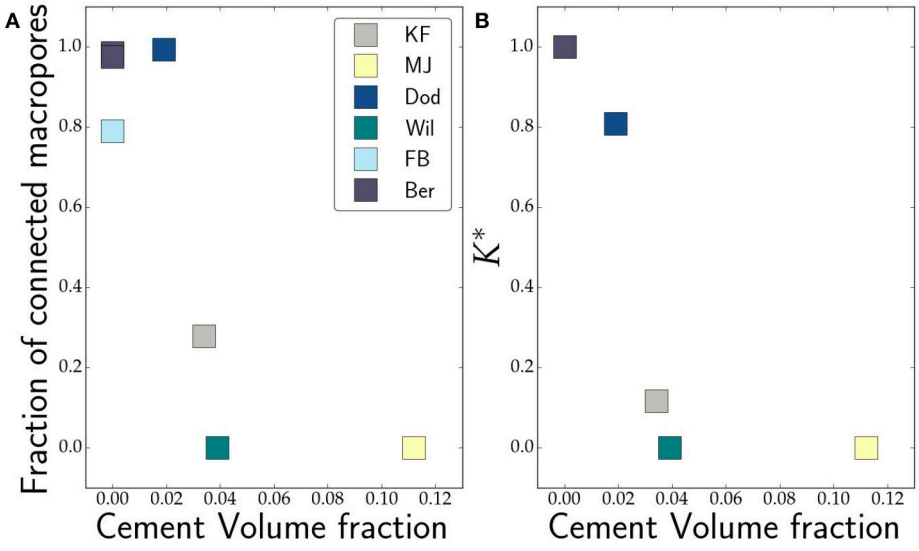

FIGURE 9 | Plots of fraction of **(A)** interconnected macroporosity and **(B)** the ratio between macro permeability and total permeability as a function of cement volume fraction.

threshold value is reached at which majority of the network will be cut-off from pervasive percolation of pore fluid.

The effect of cementation is also observed directly on the effective permeability. Since the segmentation allows us to evaluate the pore space before (total porosity) and after (macroporosity) cementation, the ratio of permeability between these two networks can be quite useful. The plot in **Figure 9B** illustrates this behavior in the plot of $k^* = k_M/k_T$ as a function of cement volume fraction. As before, we notice that the permeability declines sharply with an increase in cement volume fraction, eventually becoming zero for cement volume fractions greater than 4 vol%. The permeability values are reported in **Table 3**.

As permeability is progressively reduced by cement deposition, the fluid flux through a pore network will decrease with time. A number of recent studies on reactive porous flow during carbon capture and sequestration (Ghesmat et al., 2011; Unwin et al., 2016) and reaction infiltration instability (Takei and Hier-Majumder, 2009; Kelemen et al., 2011; Szymczak and Ladd, 2013) detailed the way in which development of reaction fronts play an important role in sequestering dissolved chemical components in the fluid. None of these studies, however, take into account the way permeability changes during the progression of reactive porous flow. As discussed above, the flux of porous flow will diminish with time due to permeability reduction, thus reducing the efficiency of carbon sequestration over the life time of an operation. The reduction in flux of porous flow can also be seen as a positive, particularly in the upper regions of carbon sequestration reservoirs where the sealing capacity may increase with time due to cementation and clogging of pores. This can enhance reservoir storage and reduce unwanted leakage. Future models incorporating the influence of cementation will provide more accurate and realistic estimates of the amount of carbon that can be stored in subsurface reservoirs.

5. CONCLUSIONS

- We analyzed 6 natural rocks, most containing a microporous cement phase. We consider the microporosity as void space to capture the pore network prior to cementation and solid to capture the pore geometry after cementation.
- In the macropore space, the pore radius varies with porosity with an exponent of 2/3, while mean coordination number, throat radius, and throat length all vary with a porosity exponent close to 1/2. Our results indicate a porosity exponent of 3.3 for permeability.
- We find that, within the sample set used in this study and the resolution of our images, the fraction of connected pores and permeability decrease sharply with cement volume fraction and the connectivity of macropores is cut off near a cement volume fraction of 4%.

DATA AVAILABILITY

The results from PNM model are available through Figshare: Hier-Majumder, Saswata; Thomson, Paul-Ross; Hazel, Alexander (2019): Data for "The Influence of Microporous Cements on the Pore Network Geometry of Natural Sedimentary Rocks." figshare. Fileset. https://doi.org/10.17637/rh.7667642.

AUTHOR CONTRIBUTIONS

P-RT carried out the image segmentation and permeability simulations in all samples. AH carried out the analysis and permeability simulations on Doddington and Knorringfjellet sandstones. SH-M and P-RT jointly carried out the final pore-network modeling and statistical analysis. All three authors contributed to writing and revision of the manuscript.

FUNDING

This research was also supported by the grant EAR125880 from the US National Science Foundation.

ACKNOWLEDGMENTS

The authors acknowledge insightful suggestions from Yiqiao Wu on the pore network models of the carbonate rocks. The raw 3D Images used in this work were kindly provided by Tom Bultreys. P-RT acknowledges support from a NERC Oil and Gas CDT graduate fellowship (grant number NE/M00578X/1).

SUPPLEMENTARY MATERIAL

The Supplementary Material for this article can be found online at: https://www.frontiersin.org/articles/10.3389/feart.2019.00048/full#supplementary-material

REFERENCES

Alyafei, N., and Blunt, M. J. (2016). The effect of wettability on capillary trapping in carbonates. *Adv. Water Resour.* 90, 36–50. doi: 10.1016/j.advwatres.2016.02.001

Andrä, H., Combaret, N., Dvorkin, J., Glatt, E., Han, J., Kabel, M., et al. (2013a). Digital rock physics benchmarks-Part I: imaging and segmentation. *Comput. Geosci.* 50, 25–32. doi: 10.1016/j.cageo.2012.09.005

Andrä, H., Combaret, N., Dvorkin, J., Glatt, E., Han, J., Kabel, M., et al. (2013b). Digital rock physics benchmarks-part II: Computing effective properties. *Comput. Geosci.* 50, 33–43. doi: 10.1016/j.cageo.2012.09.008

Bera, B., Mitra, S. K., and Vick, D. (2011). Understanding the micro structure of Berea Sandstone by the simultaneous use of micro-computed tomography (micro-CT) and focused ion beam-scanning electron microscopy (FIB-SEM). *Micron* 42, 412–418. doi: 10.1016/j.micron.2010.12.002

Berg, C. F., Lopez, O., and Berland, H. (2017). Industrial applications of digital rock technology. *J. Petrol. Sci. Eng.* 157, 131–147. doi: 10.1016/j.petrol.2017.06.074

Bernabé, Y., Li, M., and Maineult, A. (2010). Permeability and pore connectivity: a new model based on network simulations. *J. Geophys. Res. Solid Earth* 115, 1–14. doi: 10.1029/2010JB007444

Boone, M. A., De Kock, T., Bultreys, T., De Schutter, G., Vontobel, P., Van Hoorebeke, L., et al. (2014). 3D mapping of water in oolithic limestone

at atmospheric and vacuum saturation using X-ray micro-CT differential imaging. *Mater. Character.* 97, 150–160. doi: 10.1016/j.matchar.2014.09.010

Bultreys, T., De Boever, W., and Cnudde, V. (2016a). Imaging and image-based fluid transport modeling at the pore scale in geological materials: a practical introduction to the current state-of-the-art. *Earth Sci. Rev.* 155, 93–128. doi: 10.1016/j.earscirev.2016.02.001

Bultreys, T., Stappen, J. V., Kock, T. D., Boever, W. D., Boone, M. A., Hoorebeke, L. V., et al. (2016b). Investigating the relative permeability behavior of microporosity-rich carbonates and tight sandstones with multiscale pore network models. *J. Geophys. Res. Solid Earth* 121, 7929–7945. doi: 10.1002/2016JB013328

Bultreys, T., Van Hoorebeke, L., and Cnudde, V. (2015). Multi-scale, micro-computed tomography-based pore network models to simulate drainage in heterogeneous rocks. *Adv. Water Resour.* 78, 36–49. doi: 10.1016/j.advwatres.2015.02.003

Chen, N., Kuhl, T., Tadmor, R., Lin, Q., and Israelachvili, J. (2004). Large deformation during coalescence of fluid interfaces. *Phys. Rev. Lett.* 92:024501. doi: 10.1103/PhysRevLett.92.024501

Choquette, P. W., and Pray, L. C. (1970). Geologic nomenclature and classification of porosity in sedimentary carbonates. *AAPG Bull.* 54, 207–250.

Cnudde, V., and Boone, M. N. (2013). High-resolution X-ray computed tomography in geosciences: a review of the current technology and applications. *Earth Sci. Rev.* 123, 1–17. doi: 10.1016/j.earscirev.2013.04.003

Derluyn, H., Dewanckele, J., Boone, M. N., Cnudde, V., Derome, D., and Carmeliet, J. (2014). Crystallization of hydrated and anhydrous salts in porous limestone resolved by synchrotron X-ray microtomography. *Nuclear Instrum. Methods Phys. Res. B* 324, 102–112. doi: 10.1016/j.nimb.2013.08.065

Doyen, P. M. (1988). Permeability, conductivity, and pore geometry of sandstone. *J. Geophys. Res.* 93:7729.

Ghesmat, K., Hassanzadeh, H., and Abedi, J. (2011). The impact of geochemistry on convective mixing in a gravitationally unstable diffusive boundary layer in porous media: CO2storage in saline aquifers. *J. Fluid Mech.* 673, 480–512. doi: 10.1017/S0022112010006282

Hier-Majumder, S., and Abbott, M. E. (2010). Influence of dihedral angle on the seismic velocities in partially molten rocks. *Earth Planet. Sci. Lett.* 299, 23–32. doi: 10.1016/j.epsl.2010.08.007

Hier-Majumder, S., Ricard, Y., and Bercovici, D. Role of grain boundaries in magma migration and storage. (2006). *Earth Planet. Sci. Lett.* 248, 735–749. doi: 10.1016/j.epsl.2006.06.015

Iassonov, P., Gebrenegus, T., and Tuller, M. (2009). Segmentation of x-ray computed tomography images of porous materials: a crucial step for characterization and quantitative analysis of pore structures. *Water Resour. Res.* 45:W09415. doi: 10.1029/2009WR008087

Israelachvili, J. N. (1991). *Intermolecular and Surface Forces, 2 Edn.* London; San Diego, CA: Academic Press.

Jennings, J. W., and Lucia, F. J. (2003). *Predicting Permeability From Well Logs in Carbonates With a Link to Geology for Interwell Permeability Mapping.* SPE Reservoir Evaluation & Engineering. Vol. 6. Society of Petroleum Engineers. doi: 10.2118/84942-PA

Jiang, Z., Van Dijke, M. I., Sorbie, K. S., and Couples, G. D. (2013). Representation of multiscale heterogeneity via multiscale pore networks. *Water Resour. Res.* 49, 5437–5449. doi: 10.1002/wrcr.20304

Jiang, Z., van Dijke, M. I., Wu, K., Couples, G. D., Sorbie, K. S., and Ma, J. (2012). Stochastic pore network generation from 3D rock images. *Transport Porous Media* 94, 571–593. doi: 10.1007/s11242-011-9792-z

Jiao, K., Yao, S., Liu, C., Gao, Y., Wu, H., Li, M., and Tang, Z. (2014). The characterization and quantitative analysis of nanopores in unconventional gas reservoirs utilizing FESEM-FIB and image processing: an example from the lower Silurian Longmaxi Shale, upper Yangtze region, China. *Int. J. Coal Geol.* 128-129, 1–11. doi: 10.1016/j.coal.2014.03.004

Kelemen, P. B., Matter, J., Streit, E. E., Rudge, J. F., Curry, W. B., and Blusztajn, J. (2011). Rates and mechanisms of mineral carbonation in peridotite: natural processes and recipes for enhanced, *in situ* CO2 capture and storage. *Annu. Rev. Earth Planet. Sci* 39 545–576. doi: 10.1146/annurev-earth-092010-152509

Ketcham, R. A., and Carlson, W. D. (2001). Acquisition, optimization and interpretation of x-ray computed tomographic imagery: applications to the geosciences. *Comput. Geosci.* 27, 381–400. doi: 10.1016/S0098-3004(00)00116-3

Ma, L., Taylor, K. G., Lee, P. D., Dobson, K. J., Dowey, P. J., and Courtois, L. (2016). Novel 3D centimetre-to nano-scale quantification of an organic-rich mudstone: The Carboniferous Bowland Shale, Northern England. *Mar. Petrol. Geol.* 72, 193–205. doi: 10.1016/j.marpetgeo.2016.02.008

Madonna, C., Quintal, B., Frehner, M., Almqvist, B. S. G., Tisato, N., Pistone, M., et al. (2013). Synchrotron-based X-ray tomographic microscopy for rock physics investigations. *Geophysics* 78, D53–D64. doi: 10.1190/geo2012-0113.1

Marquez, X., Solling, T., Finlay, S., Bounoua, N., and Gagigi, T. (2014). 3D imaging of porosity modifying phases in Shuaiba Reservoir, Al Shaheen Field. *International Petroleum Technology Conference* (Doha), 16.

Mehmani, A., and Prodanović, M. (2014). The effect of microporosity on transport properties in porous media. *Adv. Water Resour.* 63, 104–119. doi: 10.1016/j.advwatres.2013.10.009

Menke, H., Andrew, M., Blunt, M., and Bijeljic, B. (2016). Reservoir condition imaging of reactive transport in heterogeneous carbonates using fast synchrotron tomography—effect of initial pore structure and flow conditions. *Chem. Geol.* 428, 15–26. doi: 10.1016/j.chemgeo.2016.02.030

Menke, H. P., Bijeljic, B., Andrew, M. G., and Blunt, M. J. (2015). Dynamic three-dimensional pore-scale imaging of reaction in a carbonate at reservoir conditions. *Environ. Sci. Technol.* 49, 4407–4414. doi: 10.1021/es505789f

Mostaghimi, P., Blunt, M. J., and Bijeljic, B. (2013). Computations of absolute permeability on micro-CT images. *Math. Geosci.* 45, 103–125.

Okabe, H., and Blunt, M. J. (2005). Pore space reconstruction using multiple-point statistics. *J. Petrol. Sci. Eng.* 46, 121–137. doi: 10.1007/s11004-012-9431-4

Øren, P.-E., and Bakke, S. (2003). Reconstruction of berea sandstone and pore-scale modelling of wettability effects. *J. Petrol. Sci. Eng.* 39, 177–199. doi: 10.1016/j.petrol.2004.08.002

Pal, N. R., and Pal, S. K. (1993). A review on image segmentation techniques. *Pattern Recogn.* 26, 1277–1294. doi: 10.1016/S0920-4105(03)00062-7

Pittman, E. D. (1979). "Porosity, diagenesis and productive capability of sandstone reservoirs," in *'Aspects of Diagenesis'*, (SEPM Society for Sedimentary Geology). doi: 10.2110/pec.79.26.0159

Prodanović, M., Mehmani, A., and Sheppard, A. P. (2014). Imaged-based multiscale network modelling of microporosity in carbonates. *Geol. Soc. Lond.* 406, SP406–SP409. doi: 10.1016/0031-3203(93)90135-J

Raeini, A. Q., Blunt, M. J., and Bijeljic, B. (2014). Direct simulations of two-phase flow on micro-CT images of porous media and upscaling of pore-scale forces. *Adv. Water Resour.* 74, 116–126. doi: 10.1016/j.advwatres.2014.08.012

Ramstad, T., Øren, P.-E., Bakke, S., et al. (2010). Simulation of two-phase flow in reservoir rocks using a lattice boltzmann method. *SPE J.* 15, 917–927. doi: 10.2118/124617-PA

Revil, A., Kessouri, P., and Torres-Verdín, C. (2014). Electrical conductivity, induced polarization, and permeability of the Fontainebleau sandstone. *Geophysics* 79, D301–D318. doi: 10.1190/geo2014-0036.1

Saif, T., Lin, Q., Butcher, A. R., Bijeljic, B., and Blunt, M. J. (2017). Multi-scale multi-dimensional microstructure imaging of oil shale pyrolysis using X-ray micro-tomography, automated ultra-high resolution SEM, MAPS Mineralogy and FIB-SEM. *Appl. Ener.* 202, 628–647. doi: 10.1016/j.apenergy.2017.05.039

Schlüter, S., Sheppard, A., Brown, K., and Wildenschild, D. (2014). Image processing of multiphase images obtained via X-ray microtomography: a review. *Water Resour. Res.* 50, 3615–3639. doi: 10.1002/2014WR015256

Sezgin, M., and Sankur, B. (2004). Survey over image thresholding techniques and quantitative performance evaluation. *J. Electron. Imaging* 13, 146–166. doi: 10.1117/1.1631315

Shah, S., Gray, F., Crawshaw, J., and Boek, E. (2016). Micro-computed tomography pore-scale study of flow in porous media: Effect of voxel resolution. *Adv. Water Resour.* 95, 276–287. doi: 10.1016/j.advwatres.2015.07.012

Szymczak, P., and Ladd, A. J. C. (2013). Interacting length scales in the reactive-infiltration instability. *Geophys. Res. Lett.* 40, 3036–3041. doi: 10.1002/grl.50564

Takei, Y., and Hier-Majumder, S. (2009). A generalized formulation of interfacial tension driven fluid migration with dissolution/precipitation. *Earth Planet. Sci. Lett.* 288, 138–148. doi: 10.1016/j.epsl.2009.09.016

Teles, A. P., Lima, I., and Lopes, R. T. (2016). Rock porosity quantification by dual-energy X-ray computed microtomography. *Micron* 83, 72–78. doi: 10.1016/j.micron.2016.02.004

Thomson, P.-r., Aituar-zhakupova, A., and Hier-majumder, S. (2018). Image segmentation and analysis of pore network geometry in two natural sandstones. *Front. Earth Sci.* 6:58. doi: 10.3389/feart.2018.00058

Trier, Ø. D., and Jain, A. K. (1995). Goal-directed evaluation of binarization methods. *IEEE Trans. Patt. Anal. Mach. Intelligence*, 12, 1191–1201.

Unwin, H. J. T., Wells, G. N., and Woods, A. W. (2016). CO2 dissolution in a background hydrological flow. *J. Fluid Mech.* 789, 768–784. doi: 10.1017/jfm.2015.752

Valvatne, P. H., and Blunt, M. J. (2004). Predictive pore-scale modeling of two-phase flow in mixed wet media. *Water Resour. Res.* 40:W07406. doi: 10.1029/2003WR002627

Wang, W., Kravchenko, A., Smucker, A., and Rivers, M. (2011). Comparison of image segmentation methods in simulated 2d and 3d microtomographic images of soil aggregates. *Geoderma* 162, 231–241. doi: 10.1016/j.geoderma.2011.01.006

Wildenschild, D., and Sheppard, A. P. (2013). X-ray imaging and analysis techniques for quantifying pore-scale structure and processes in subsurface porous medium systems. *Adv. Water Resour.* 51, 217–246. doi: 10.1016/j.advwatres.2012.07.018

Wildenschild, D., Vaz, C., Rivers, M., Rikard, D., and Christensen, B. (2002). Using x-ray computed tomography in hydrology: systems, resolutions, and limitations. *J. Hydrol.* 267, 285–297. doi: 10.1016/S0022-1694(02)00157-9

Youssef, S., Rosenberg, E., Gland, N. F., Kenter, J. A., Skalinski, M., and Vizika, O. (2007). "High resolution CT and pore-network models to assess petrophysical properties of homogeneous and heterogeneous carbonates," in *SPE/EAGE Reservoir Characterization and Simulation Conference, 28–31 October* (Abu Dhabi: Society of Petroleum Engineers), 28-31. doi: 10.2118/111427-MS

Conflict of Interest Statement: The authors declare that the research was conducted in the absence of any commercial or financial relationships that could be construed as a potential conflict of interest.

Chapter 5

Pore Network Analysis of Brae Formation Sandstone, North Sea

Description. This chapter is presented in manuscript format and is currently in the second stage of review in the journal Marine and Petroleum Geology. In this work, subsampled micro-cores are used for image analysis from two cored wells of the Miller Oil Field, UK. The X-ray image acquisition was performed at the Natural History Museaum, obtaining four samples from each well across an interval of roughly 5 m. Macroporosity measurements display a range between 4.9% to 15.2% across the samples. The samples also contain a small proportion of microporosity in the form of secondary minerals. Three regimes of pore connectivity are identified through the network analysis. At macroporosity values $< 3\%$, the network becomes isolated, while full connection is achieved at porosities $> 10\%$. A partially connected regime exists between 3 and 10% porosity. The porosity and permeability results agree well with existing measurements.

Author contribution. Paul-Ross Thomson performed the image filtering and segmentation, conducted the image analysis, interpreted the data, performed some of the Helium pycnometry measurements, generated most figures and wrote most of the manuscript.

Pore Network Analysis of Brae Formation Sandstone, North Sea

Paul-Ross Thomson[a], Mark Jefferd[b], Brett L Clark[c], Domenico Chiarella[a], Tom Mitchell[b], Saswata Hier-Majumder[a]

[a]*Department of Earth Sciences, Royal Holloway University of London, Egham, Surrey, TW20 0EX, UK.*
[b]*University College, London*
[c]*Natural History Museum, London*

Abstract

In this work, we apply digital rock physics (DRP) to characterize the pore networks of the Brae Formation sandstones from two different wells in the Miller field area (North Sea, UK). Using X-ray micro-CT scans, we calculate the porosity and permeability and generate pore network models to assess pore shape characteristics. The porous samples are marked by macroporosities ranging from 4.9% to 15.2% with the effective porosities varying from 0 to 14.8%. The samples also contained some microporosity hosted in secondary and accessory mineral phases, varying between 2.6% to 10.7%. Pore network model results for total porosity indicate that the samples have median pore and throat radii ranging from 5.5 μm to 16.8 μm and 6.4 μm to 12.9 μm, respectively. The throat length of all samples has a median value ranging between 36.3 μm and 82.4 μm. The ratio between effective porosity and total porosity (ϕ^*) varies with total porosity (ϕ) following the exponential relation $\phi^* = 0.98 - e^{-(\phi - 0.032)/0.028}$. Pore network connectivity is established at a

Email address: Paul-Ross.Thomson.2016@live.rhul.ac.uk (Paul-Ross Thomson)

porosity of 3% and full communication is achieved at porosities exceeding 10%. Permeability was found to vary with total porosity with an exponent of 3.67. Based on these observations and the results from our models, the connectivity of the pore network has important implications for predicting reservoir performance during large scale subsurface projects such as hydrocarbon production and CO_2 storage.

Keywords: Digital Rock Physics, Porosity, Permeability, Pore Network Model, Reservoir, X-ray micro-CT, Brae Formation, Miller Field

1. Introduction

Generating an accurate reservoir model is of critical importance in forecasting the lifespan of hydrocarbon reservoirs and estimating the efficiency of carbon capture and sequestration. One critical parameter controlling the flow of fluids within subsurface reservoirs is the fraction of effective or connected pore spaces in the reservoir. Effective porosity, the primary conduit of porous flow, can be significantly smaller than the bulk porosity of the rock determined from well logs. In reservoir rocks, especially those containing clay minerals and accessory phases, a significant part of the pore space can be trapped in micropores which are unfavorable to porous flow (Bultreys et al., 2016; Thomson et al., 2019). Additionally, effective porosity within the macropores—pores distributed along grain edges and corners—can be significantly lower than the total macroporosity. To quantify the connectivity of the pore space, it is therefore necessary to combine high resolution visualization of pore spaces with bulk measurements.

In this work, we address the issue of quantifying effective pore space in a

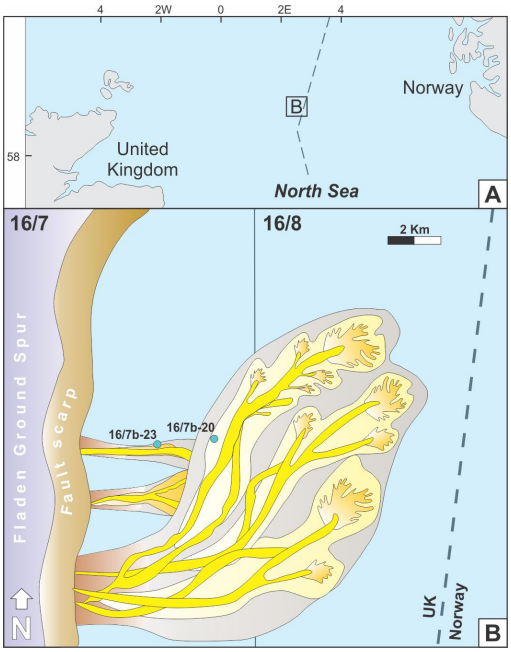

Figure 1: (A) Map of the North Sea showing the position of the studied system. (B) Depositional map of the Miller Fan system with the position of the studied pair of cored wells.

well studied suite of natural sandstones from a former producing hydrocarbon field in the North Sea. Using digital rock physics (DRP) techniques, we compare the pore network characteristics of the Brae Formation sandstones occurring at different depth intervals. The Brae Formation comprises primary reservoir rock in the Miller Oil Field, located at the western edge of the South Viking Graben (Rooksby, 1991). These rocks have been studied extensively in the context of hydrocarbon exploration and carbon capture and sequestration (Lu et al., 2011; Maast et al., 2011; Rooksby, 1991).

The Southern Viking Graben is an Upper Jurassic rift basin containing a major hydrocarbon province extending over the geographic border separat-

ing United Kingdom and Norway (Figure 1A; Turner and Cronin (2018)). In particular, a large proportion of hydrocarbon reserves is contained in synrift deposits, which constitute the Brae Formation. The Kimmeridgian-Tithonian Brae Formation consists of the Brae 1 and Brae 2 zones representing the result of large volumes of clastic material that were sourced from the Fladen Ground Spur area into the South Viking Graben (Figure 1B). Deposits result in fault-bounded systems fed through sand-rich turbiditic flows forming vertically- and laterally-stacked lobe elements (McClure and Brown, 1992). The Brae sandstone reservoirs are encased and distally interfingered within the organic-rich hemipelagic shale of the Kimmeridgian Clay Formation (Rooksby, 1991). In this study, we focus on cores recovered from two wells, one from the Miller field (16/7b-20) and the other from the edge of the Central Brae field (16/7b-23), within the depth range between 4040 m and 4064 m. The two cored wells are from different locations within the turbidite fan system in the Brae-Miller field complex. Well 16/7b-23 is located proximal to the sediment source supply and major fault of the South Viking Graben, while well 16/7b-20 is distally located, nearer the center of the graben.

Previous studies on the reservoir characteristics of the South Viking Graben involved porosity derived from well logs (Maast et al., 2011; Rooksby, 1991) and studies of secondary mineral precipitation (Aase and Walderhaug, 2005; Lu et al., 2011; Marchand et al., 2001). These studies indicate that the bulk porosity at depths greater than 4000 m varies widely between 5% and 25% (Maast et al., 2011), with an average bulk porosity of 16% in the Brae Formation (Rooksby, 1991). Studies on the nature of secondary mineraliza-

tion indicate that the pore space in the sandstone can be filled with varying amounts of clay, microquartz, or carbonate phases (Aase and Walderhaug, 2005; Lu et al., 2011; Maast et al., 2011; Marchand et al., 2001). Despite this array of studies on the nature of the Brae Formation rocks, the nature of connectivity of the pore spaces, values of pore and throat diameters, and the fraction of pore space trapped in the secondary mineral phases remain poorly understood. Quantifying the factors controlling the connectivity of the macropores is crucial in estimating the permeability of the rock.

A number of empirical studies highlight the importance of effective porosity on permeability of reservoir rocks (Gomez et al., 2010; Mavko and Nur, 1997; Revil et al., 2014). The relationship between porosity, ϕ, and permeability, k, is commonly expressed within the Kozeny-Carman relation of the form $k \propto \phi^3$, which arises from a model of pores and throats situated along grain corners and edges. Experimental measurements of permeability by Bourbié and Zinszner (1985) demonstrated that this model breaks down at low porosities, typically $< 9 - 10\%$. Mavko and Nur (1997) suggested a modified form of the relation, $k \propto (\phi - \phi_p)^3$, where $\phi_p = 2.5\%$ is defined as the percolation threshold, to address the change in porosity exponent. A number of experimental measurements of permeability in various clean sandstones led to a number of different values of the porosity exponent and the percolation threshold (Doyen, 1988; Gomez et al., 2010; Madonna et al., 2013; Revil et al., 2014). Simultaneous determination of effective porosity and permeability in sandstones allows us to identify the role of pore network connectivity on permeability directly. Despite a number of measurements of bulk porosity and permeability on the Brae Formation sandstone, direct

constraints on the permeability arising from an analysis of the pore network still remains poorly understood.

This work aims to bridge this gap by studying the characteristics of the pore network and simulating porous flow in the Brae Formation from high resolution computed microtomographic (micro-CT) volumes. In order to assess microporosity in secondary minerals and clay minerals, we compare our results with bulk porosity measurements using Helium pycnometry. Through X-ray micro-CT techniques, this study aims to characterize the pore volume properties of the Miller field (Brae Formation, Upper Jurassic, North Sea) cored in wells 16/7b-20 and 16/7b-23. Using a pore network model (PNM) approach to quantitatively classify pore space properties of each sample in terms of pore radius, throat radius, throat length and coordination number (number of throats connected to each pore).

2. Materials and methods

We prepared eight different samples for X-ray micro-CT image acquisition by creating 5 mm diameter core plugs. The acquired images were processed to segment the pore volume in each sample. The stacked images produced a 3D pore volume from which the total and effective porosity was measured. These 3D pore volumes were used further to measure the geometry of the pores and throats and to calculate the absolute permeability of each sample. In the following subsections, we outline the details of each of these steps.

2.1. X-ray micro-CT image acquisition

To acquire the micro-CT images, cylindrical shaped core samples were prepared. We used eight core samples from British Petroleum, collected

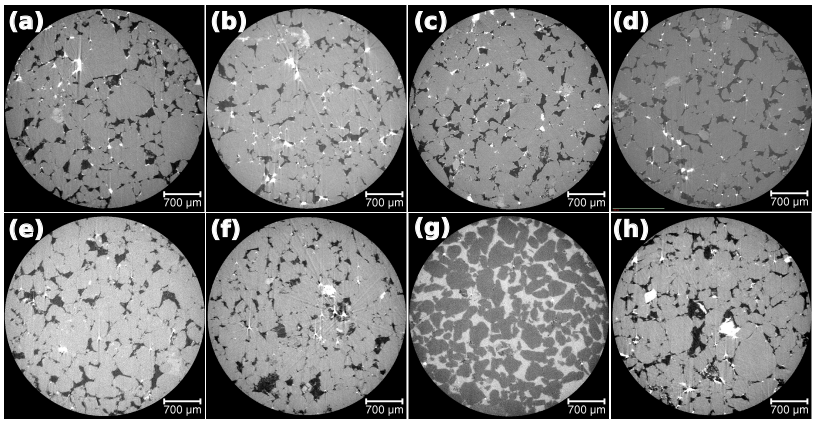

Figure 2: Gray scale image slices of the eight samples studied in this work. The panels are arranged numerically from samples BFS1 (a) to BFS8 (h). The scale bar in each image represents 700 μm. Resolution of the images in voxel size are reported in Table 1.

within an interval of ∼5 m in well 16/7b-20 (between 4040.10 m and 4045.13 m depths) and ∼4 m in well 16/7b-23 (between 4061 m and 4063.75 m depths). The 5 mm diameter core plugs used for micro-CT acquisition were drilled from sections of these 15 cm diameter cores. The diameter of the cylinders minimized X-ray absorption by additional sample mass outside the ∼4 mm diameter imaging volume. All 8 Brae Formation sandstone samples were labeled according to their depth (BFS1 to BFS8, see also Table 1) and marked to show orientation (way up) from which it had been sampled. Supplementary Figure S1 shows an example of the original core and one of the ∼5 mm core plugs used during image acquisition.

We acquired the X-ray images on a Zeiss Xradia Versa 520 scanner at the Imaging and Analysis Center at The London Natural History Museum. The hardware utilizes a transmission source generating polychromatic X-rays with an energy range between 30 and 160 kV and a maximum power capabil-

ity of 10 W. The X-ray tube generates a focal spot size, which is small enough to provide sufficient spatial coherence to utilize phase contrast enhancement. Increasing the sample-detector distance to 14 mm allows to detect interference fringes at object boundaries in the images, including mineral phase boundaries inside the rock. Depending on the rock type (composition and grain size) a voltage of 80 to 100 kV was selected to optimize X-ray transmission. A full 360 degree rotation was used to collect 3201 projections for each scan to minimize reconstruction artifacts. A camera binning of 2×2 was applied to samples requiring higher voltage during the acquisition in order to increase the signal-to-noise ratio and improve overall contrast. Depending on the nature of the sample, we acquired images of resolution 2 μm^3 voxels and 3.9 μm^3 voxels. The image resolution for each sample is reported in Table 1. Data reconstruction was performed using the Zeiss Reconstructor Scout-and-Scan software. A filtered back projection algorithm with beam hardening correction was used to reconstruct the projections to produce a stack of 16-bit tiff images. In the next step, we processed each stack of gray scale images. The micrographs in Figure 2 show slices of raw gray scale images from each sample.

2.2. Filtering and segmentation

We carried out the image analysis and simulations using the software PerGeos - Thermo Fisher Scientific. The raw gray scale images (e.g. Figure 3(a)) are filtered to reduce noise, to smooth the image pixels, and to increase the contrast between pore space, quartz grains and other phases. The non-local means filter (Buades et al., 2008, 2010) was applied to all images. Figure 3(b) highlights the results of the non-local means filter, with enhanced image

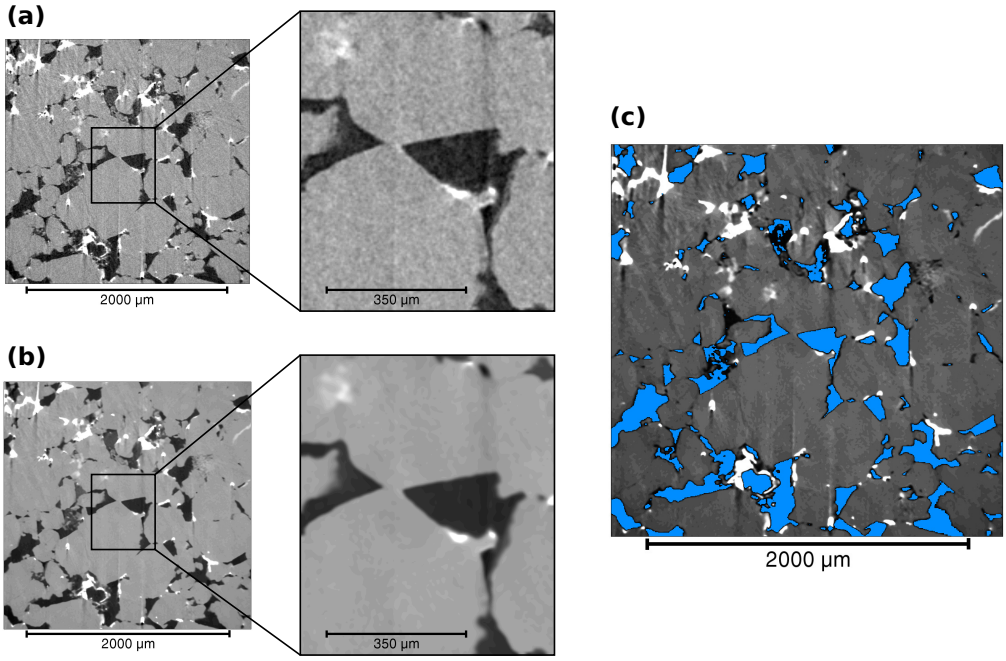

Figure 3: Image processing steps: (a) 2D slice of the raw image data with zoomed inset showing speckled pixelated texture, (b) 2D slice following non-local means filter with zoomed inset showing smoothed pore and grain texture, and (c) 2D image showing segmentation of the macropore phase (blue).

quality and no apparent loss of microstructural detail. The 3D images used in this study were largely free from artifacts such as beam hardening and bright fringes along mineral grains (Thomson et al., 2018), therefore, no special filtering was necessary.

The filtered images were segmented to separate macropores from other phases, such as quartz, feldspar, carbonates, and clays (Iassonov et al., 2009; Ketcham and Carlson, 2001; Wildenschild et al., 2002). All the samples used in this study contained variable amounts of microporosity, associated with micron to submicron sized pore spaces, and are included in secondary mineral

growths and clay minerals. The dimension of these micropores are beyond the resolution of the scanner, precluding a quantitative estimate of microporosity based on the microtomographic images (Thomson et al., 2019). As a result, we employed a binary segmentation technique. In this method, we segment the images into two phases: macropores and solids. Figure 3(c) shows a 2D slice following the binary segmentation of the macroporosity phase (blue). The macroporosity consists of both pores and throats, with pores located at grain corners acting as a junction between two or more throats that form along the edge of grains. Solids comprise of all mineral grains as well as parts of the matrix containing microporosity. We carried out the pore network modeling in the macropores, while the volume fraction of micropores were determined by the use of Helium pycnometry measurements.

In the binary segmentation method, we selected the two phases using both an automated segmentation technique (Otsu, 1979) and a manual interactive thresholding selecting the peaks on the bimodal histogram of gray scale intensity. The phases are defined based upon their gray scale color, which is a function of X-ray attenuation, related to the density of different materials in the samples. Figure 4(a) shows a 3D volume rendering visualization of the filtered raw data, highlighting a very dark gray/black shade that belongs to the macropore space; the micropores were marked by specular patches of dark gray, surrounded by a lighter gray; while quartz grains and other minerals such as carbonates and clay minerals are associated with lighter shades of gray, forming a broad peak at the higher intensity end of the spectrum. For the threshold segmentation of the macropores, we assigned pixels from the peak at the low intensity end of the gray scale histogram. All samples

have pixel intensity values between a range of 0 and 6200 for the macroporosity. A number of previous studies explored the relative merits of automated global segmentation and local segmentation methods (Iassonov et al., 2009; Pal and Pal, 1993; Sezgin and Sankur, 2004; Trier and Jain, 1995). While an automated thresholding algorithm circumvents the possibility of operator bias, this method can neglect local variations in gray scale intensity, leading to over or underestimation of macroporosity (see Thomson et al., 2019, and references therein). While we calculated the porosity using both techniques, we found that the automated thresholding method consistently led to inaccurate phase boundary detection when compared with the original gray scale images. We report the macroporosity calculated using both techniques in Table 1 in the supplement, but in the main article and subsequent calculations, we use our preferred results from manual thresholding. To ensure that the macropores were represented accurately, pixels assigned to the macropore phase were checked visually at various intervals in the samples (e.g. top, middle, bottom). We used this process to check that the pixels selected as part of the macroporosity network were consistent throughout the sample and to avoid the unwanted inclusion of pixels from other materials.

2.3. Pore network modeling and microporosity

The first step in pore network modeling is the determination of total macroporosity. We use the macropore space from the binary segmented images to evaluate total macroporosity. To quantify the uncertainty in the total macroporosity in each sample, we evaluated the total macroporosity over a number of regions of interest (ROI) of different dimensions. We then take the maximum variation in the calculated macroporosity and report this variation

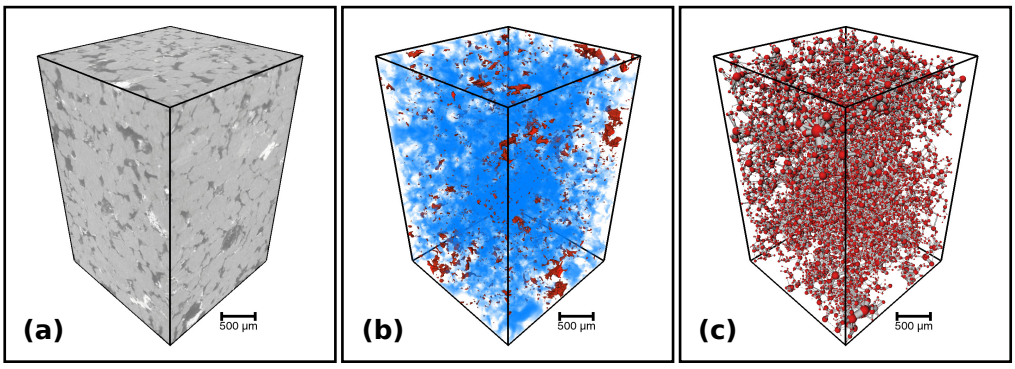

Figure 4: Raw image and pore network model output from sample BFS8. (a) A 600×600×900 voxels 3D stack of gray scale images. (b) Volume rendering of effective porosity (blue) and unconnected pore spaces (red). (c) Pore network model of total porosity, scaled to show pore radius and throat radius, where red spheres represent pores and gray cylinders are throats. This sample contains a total porosity of 15.2 vol% and an effective porosity of 14.8 vol%.

as the uncertainty. All porosity measurements and the dimensions of their ROIs are reported in Table 1 of the supplement. Once the total macroporosity was evaluated, we then quantified the effective macropore space.

We used the segmented gray scale images to quantify the macropore network characteristics, and to evaluate the permeability through numerical simulations. To provide the most representative data, samples were cropped to volumes just below that of their maximum dimensions. For samples acquired with voxels dimensions of 2.0 μm^3, we specified a ROI of dimension 600×600×900 voxels. The samples acquired at lower resolutions of 3.9 μm^3 had ROIs of 1200×1200×1800 voxels. As discussed earlier, in this study the focus of our digital rock physics analysis is entirely on the macroporosity of the sandstone samples.

In order to characterize the geometry of the pore volume, the 3D segmented label fields must be processed by a skeletonization algorithm (See Thomson et al. (2018, 2019) for additional information about the algorithm). The pore network model extension in PerGeos uses a hybrid algorithm (Youssef et al., 2007) to erode the 3D pore geometry into a one voxel thick skeleton. The skeleton retains the original geometry of the pore network and is used to calculate the length and connectivity of each line. Throats are identified as the one voxel thick lines on the skeleton, while pores are defined as the junctions where two or more throats intersect. The number of throats intersecting a pore is defined as the coordination number of the pore. Pores and throats are designated based on a known extreme radius and their dimensions are calculated based on the expansion of a sphere within pores and the length and equivalent hydraulic radius in each throat. Results of the algorithm include both numerical data (e.g. coordination number, pore radius, throat radius, and throat length) and 3D volumes (node and branch representations).

The pore network model was used to measure the pore geometries for both total porosity and effective (connected) porosity. The volume fraction of total porosity was calculated by combining each voxel assigned to the pore space to produce a 3D volume. To calculate the effective porosity, the total pore space was further processed to determine a percolation threshold. If a network of pores connects at least one pair of opposing faces of the 3D volume, then the network is classified as effective. Pores made up of voxels that do not contribute to the effective network are classified as isolated and are filtered as a consequence of the axis connectivity algorithm. Once

the pores and throats involved in the connected network are identified, the effective porosity is calculated based on their representative voxels. Figure 4(b) shows a 3D volume rendering visualization of the effective pore network (blue) and isolated pores (red) in sample BFS8. Figure 4(c) shows a pore network model representation of the total porosity found in sample BFS8. In this idealized model, the pores are shown as red spheres, while throats are displayed as gray cylinders. These models can provide useful visual aids to compare and contrast the frequency of large pores and throats in each sample.

In order to account for microporosity in the samples, we carried out bulk porosity measurements using Helium pycnometry. We used two sets of samples to carry out these measurements. In the first set of measurements, we used the cylindrical samples that were used to obtain the micro-CT images. In the second set, we prepared larger cylinders of the rocks from the same core. Details of the Helium porosity measurements are provided in the supplementary material. Since the Helium pycnometer measures both the effective micro and macroporosity, we calculated the microporosity by subtracting the macroporosity from the Helium pycnometry measurements.

2.4. Permeability simulations

The 3D images for the effective pore network were used to assess the absolute permeability in each sample. Since these are the only pores considered to contribute to flow, the isolated pores that do not form part of the effective 3D network are ignored. A finite volume solver (from the petrophysics module in PerGeos) was used to calculate the flow of water through the effective pore space. The equations for mass and momentum conservation for the fluid

flow are

$$\boldsymbol{\nabla} \cdot \boldsymbol{u} = 0, \tag{1}$$

$$-\boldsymbol{\nabla} P + \mu \nabla^2 \boldsymbol{u} = 0, \tag{2}$$

where $\boldsymbol{u}$ is the fluid velocity vector, P is the pressure and μ is the viscosity of water ($= 1 \times 10^{-3}$ Pa s). The boundary conditions for the simulation are described in detail by Thomson et al. (2018). We used an iterative solver to determine the velocity and pressure. The iterations were continued until the L_2 norm of the residuals reached a predetermined tolerance level. As shown by Thomson et al. (2019) the tolerance level for error, ϵ, strongly determines the numerical value of permeability obtained from the simulations. Using a predetermined value for $\epsilon \leq 10^{-6}$ the permeability is measured and compared between all samples with an effective pore network.

3. Results

The results of porosity and permeability analysis from our images are displayed graphically in Figure 8. Additional detailed information on the porosity and permeability is provided by quantitative analysis in Section 3.1. The results from porosity, pore network modeling and permeability image analysis are summarized in Table 1 of the supplementary material. The results of the pore network modeling are described in Section 3.2.

3.1. Total and effective Porosity

The total porosity is given by the inclusion of effective and isolated pores in the samples that were analyzed. All but one of the samples has visual

Sample	Well ID	Depth	Macroporosity (Effective)	Microporosity	Permeability
		(m)	%	%	(mD)
BFS1[a]	16/7b-20	4040.10	7.2±0.4 (5.8)	10.4 ± 1.4	91.2
BFS2[a]	16/7b-20	4041.35	7.1±3.2 (5.7)	8.3 ± 0.3	86.3
BFS3[b]	16/7b-20	4043.75	8.0±0.2 (6.4)	10.2 ± 1.7	7.6
BFS4[b]	16/7b-20	4045.13	9.6±1.0 (9.1)	7.7 ± 2.3	104.2
BFS5[b]	16/7b-23	4061	7.8± 0.5 (5.1)	10.7 ± 1.0	6.7
BFS6[a]	16/7b-23	4062	4.9± 0.6 (0.0)	7.2 ±0.6	0.0*
BFS7[b]	16/7b-23	4063	0.0	2.6 ± 0.7	0.0*
BFS8[a]	16/7b-23	4063.75	15.2 ± 2.0 (14.8)	3.5 ± 0.2	795.1

[a]Voxel size 3.9 μm^3, [b]Voxel size 2.0 μm^3, * zero effective porosity

Table 1: Summary of sample data used in this study, including sample name, well ID depth interval, and voxel resolution.

porosity, which, based on our methods, provided measurements for total and effective pore networks in most samples. Sample BFS7 was the only rock type that appears cemented and does not show clear pore spaces (Figure 2(g)). Across the two cored wells, measured porosity ranged from 4.9% to 15.2%.

The samples from well 16/7b-20 range in total macroporosity from 7.1% to 9.6%, with a mean value of 8.0%. Effective porosity values range from 5.7% to 9.1%, with a mean value of 6.8%. Within the narrow range of depth in our dataset, no distinct correlation between porosity and depth was observed. As indicated in Table 1, the average bulk porosity (macro and micro combined) in this well is 17%. This value is in good agreement with the 16% bulk porosity estimated by Rooksby (1991). The samples acquired from well 16/7b-23 have total porosity ranging from from 4.9% to 15.2%, with a mean value of 9.3%. The pore space in one of the samples from this well, BFS7, was completely replaced by carbonate precipitates (see Figure 2(g)). In another sample, BFS6, the macroporosity was 4.9%, without a detectable effective network. Figure S2 within the supplementary material shows the volume rendering visualization for all samples with a pore network, including sample BFS6 (f) with no connected, effective pore space. As a result, these two samples were unusable for permeability simulations. Of the two samples that have an effective network of pores, their volume fractions are 5.1% and 14.8%, with a mean value of 12.6%. These measurements were performed on the largest ROI to give the most representative data possible. Much like the analysis in the previous well, we do not observe any particular trend in porosity with increasing depth.

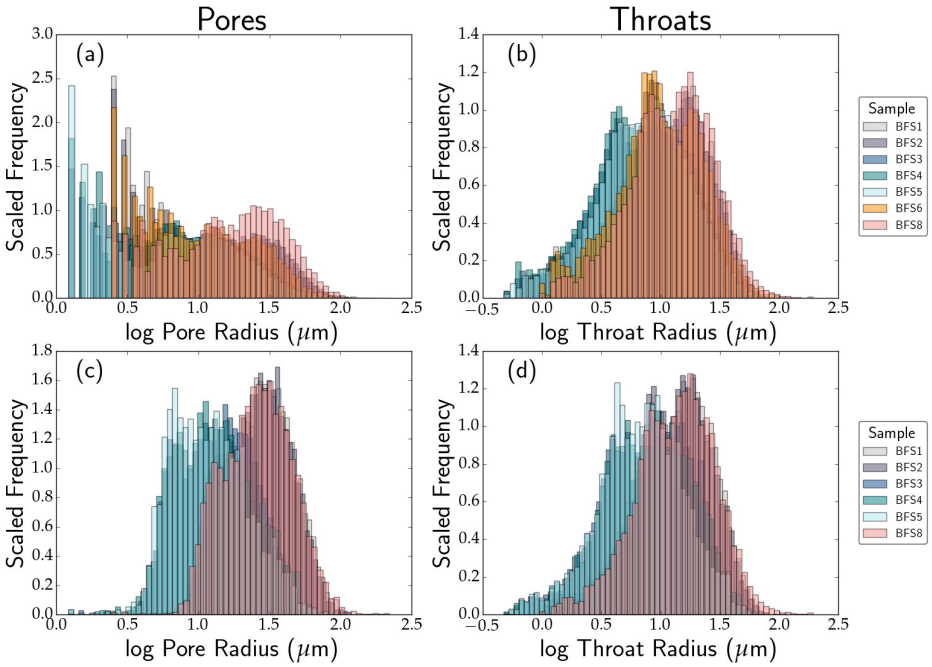

Figure 5: Log normal distribution of pore and throat geometries in the total pore network ((a) and (b)) and effective pore network ((c) and (d)). The left column illustrates the distribution of pore radii, while the right column displays the distribution of throat radii. The histograms have been normalized to emphasize the distinction between them.

3.2. Pore network modeling

Output from the pore network models reveal a number of distinct features of total and effective macroporosities. First, we compare the distribution of pore and throat radii in the total porosity and effective porosity. The histograms in Figure 5 compare the histograms of logarithmic pore and throat radii in total porosity (panels (a) and (b)) with those in effective porosity. The pore radius of the total pore space in all samples show a peak near the low end in Figure 5(a). This peak, consisting of small pores, disappears in

the distribution of effective porosity. Comparison of the two distributions suggests that the total macroporosity consists of a large number of small, unconnected pores, while the effective pore network consists of fewer, larger pores. The throat radii of the total pore space in Figure 5(b) and effective pore space in panel (d) both display bimodality. Neither distribution contains a large peak at the low values. Unlike the pore radii, the peaks of throat radii do not show a significant shift to the high values from total to effective porosity. We present the median values of the pore and throat radii, throat lengths, and coordination numbers for all samples in Table 1 of the supplementary material.

An increase in porosity results in larger, better connected pores and throats with considerable variations in the pore network characteristics. The nature of the variation, however, is different between total and effective porosity. In Figure 6, we plot these variations in median pore radii (panel a), median throat radii (b), mean coordination number (c), and median throat lengths (d). The data from effective porosity are plotted as filled symbols, while the data from total porosity are plotted as open symbols. The sample names are annotated in the legend. While both data sets in panel (a) show that the pore radius increases with an increase in porosity, the median pore radius for effective pores are larger than the total porosity. Despite this difference, the general trend indicates that more porous rocks are characterized by larger pores. This behavior of the pores is also supported by the trend of mean coordination number with porosity. In total porosity, the mean coordination number shows a 3/4 power law relation with porosity as shown by the slope of the log-log plot in panel (c). This variation is practically absent in

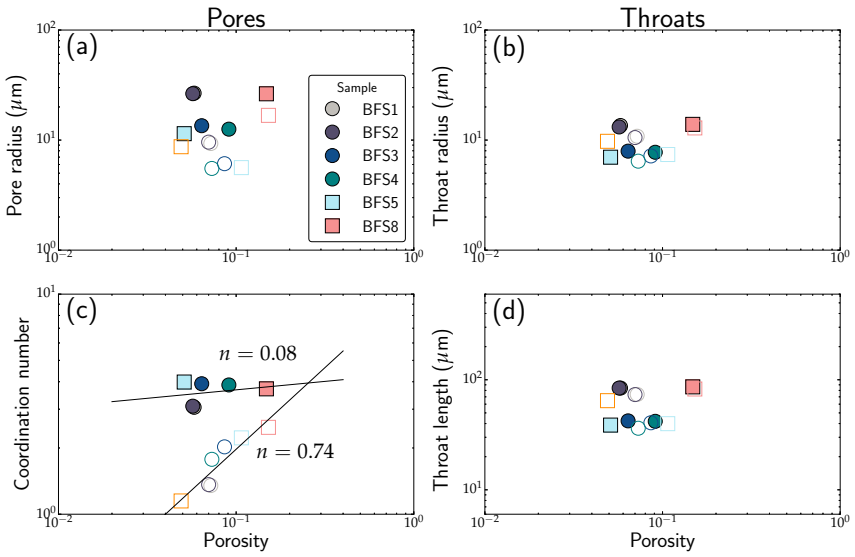

Figure 6: Pore geometry characteristics for the seven samples in this study. The panels display log-log plots of (a) pore radius, (b) throat radius, (c) mean coordination number, and (d) throat length as a function of total porosity. Core-derived data from wells 16/7b-20 and 16/7b-23 are symbolized by circles and squares, respectively. Filled symbols represent data that display effective porosity while open symbols indicate data that make up total porosity.

effective porosity, with mean coordination numbers varying within the narrow range of 3-4 and a log-log slope of 0.08, indicating that the pores in a effective network must be above a threshold value. In contrast, the median throat radius and length in panels (b) and (d) do not display any significant variations between the two sets of porosities, but show a general trend of increase in value with an increase in porosity.

Taken together, the results indicate that pores, junctions in the network, play a crucial role in the effectiveness of the network. Rocks with higher

porosity are characterized by larger pores with higher coordination numbers. The results presented here on coordination number of pores are very similar to previous studies involving image analysis and modeled microstructure (Bernabé et al., 2010; Lindquist et al., 2000; Thomson et al., 2018). Theoretical models and analogue material studies also indicate that mean coordination number or the degree of connectivity of a solid phase increase with the increase in phase volume fraction in the material (Bertei and Nicolella, 2011; van de Lagemaat et al., 2001; Wimert and Hier-Majumder, 2012; Zou et al., 2003). To establish an effective pore network, a coordination number of at least 3 is required. The distinction between total and effective porosities are sharpest at low values of total porosity.

The effectiveness of pore space becomes more obvious when we compare the effective porosity with the total porosity. The plot in Figure 7(a) compares the effective porosity and the total porosity from our samples. We also include data from the pore network models of sandstones and limestones by Thomson et al. (2019) for comparison. To aid visualization, we plotted a line with a slope of 1 in the figure. At total porosities exceeding 10%, the effective porosity is nearly the same as the total porosity, as the data points fall on the line with a slope of 1. At lower values of total porosity, the effective porosity drops sharply, along the dashed line shown in the figure. This behavior becomes more prominent when the ratio between effective and total porosity is plotted against the total porosity in Figure 7(b). As both sets of plots indicate, three distinct regimes can be identified from the plot. Above 10% total porosity, nearly 100% of the porosity is effective. We call it the fully effective regime. Below this threshold, the effective porosity drops

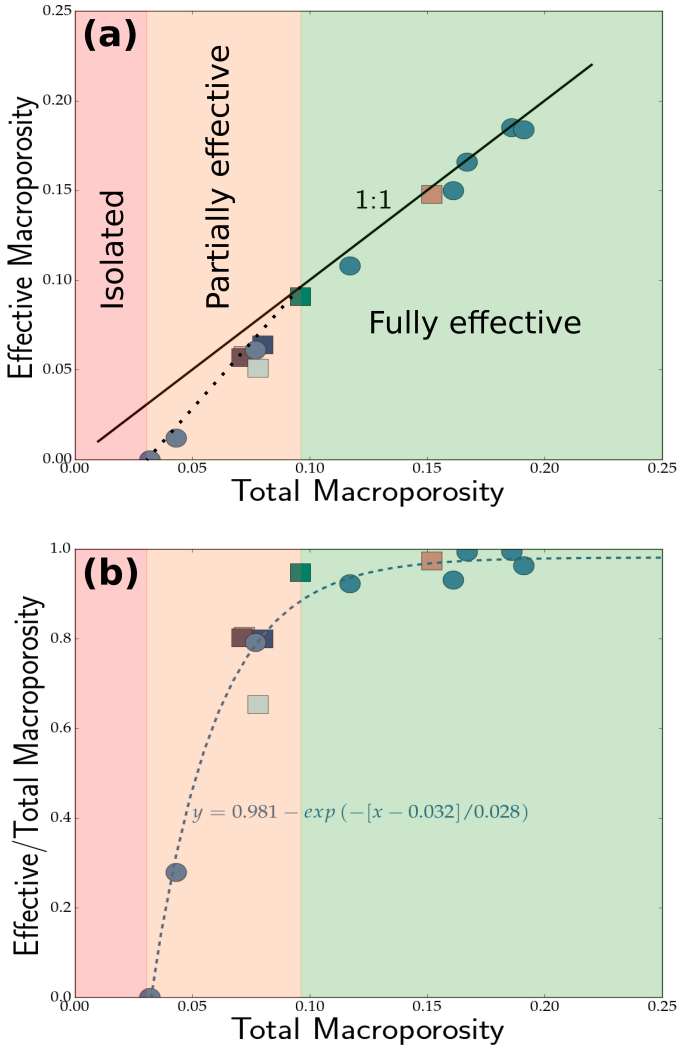

Figure 7: The effectiveness of pore space in fluid transport. (a) Effective (connected) porosity of the rock as a function of total macroporosity. The solid black line shows the 1:1 correlation. (b) The ratio between effective and total porosity as a function of total porosity. The symbols are the same as in Figure 8. The dashed blue line is the fit to the data and the equation to the fit is annotated in the plot.

sharply with a decrease in the total porosity. This is the regime of a partially effective pore network. With further reduction in porosity, the effective pore fraction eventually becomes zero, leading to the zone of isolated pore spaces. Our results indicate that this value is near a total porosity of 3%, similar to previously published estimates of percolation threshold of 2.0% -2.5% (Gomez et al., 2010; Mavko and Nur, 1997; Revil et al., 2014). The ratio between effective and total porosity, ϕ^*, can be expressed as a decaying exponential function $\phi^* = a - e^{-(\phi - b)/c}$ of total porosity, ϕ. We overlay a fit of this function to the combined data set in Figure 7(b) with the values of the parameters a, b, and c displayed on the plot. This function is useful in providing a first-order quantitative evaluation of reservoir quality in tight reservoirs typically marked by low total porosity. These results also outline the importance of pore network modeling in understanding the nature of connectivity of reservoir rocks, results that are not attained by traditional bulk porosity measurements.

4. Discussion

4.1. Comparison with previous permeability measurements

Effective porosity plays an important role in controlling the permeability of reservoir rocks. A study on experimental determination of permeability of clean Fontainebleau sandstones by Bourbié and Zinszner (1985) demonstrated that the porosity exponent, n, in the Kozeny-Carman relation $k = k_0\phi^n$ changes from the classical value of 3 to a much higher value of up to 7 as the total porosity decreases below 9%. Citing the role of a percolation threshold, $\phi_p = 2.5\%$, Mavko and Nur (1997) proposed a modified form of

the Kozeny-Carman relation, $k = k_0(\phi - \phi_p)^n$, which provided a uniform value of $n = 3$ for the entire range of porosities. Later experimental determinations of permeability showed that this percolation threshold shows some variation between different rock types, but usually varies between 2.0-2.5% (Gomez et al., 2010; Revil et al., 2014). In these studies, the percolation threshold was determined by fitting the experimental data. This value, however, is quite similar to the value of ∼3% total porosity at which we observe the establishment of a effective pore network in our samples. We also notice that the value of porosity at which the slope of the porosity-permeability curve changes is very close to the value of full connection threshold (8-10%) reported in Figure 7. Information on pore network connectivity was unavailable for the studies by Bourbié and Zinszner (1985) and Mavko and Nur (1997). The results presented here shows that the two crucial porosity values, the percolation threshold and the slope-break, are associated with the isolation threshold and full connection threshold.

Using the modified Kozeny-Carman relation, Mavko and Nur (1997) obtained a value of the porosity exponent $n = 3$. Later studies by Gomez et al. (2010) and Revil et al. (2014) found that the value of n varies between 4.0 to 4.5 for a percolation threshold of 2%. Another set of experimental measurements of permeability by Doyen (1988) found that using the traditional Kozeny-Carman relation, the porosity exponent is 3.8 over a range of total porosity between 5 to 22%. All of these experiments were carried out in clean sandstones containing negligible amounts of microporosity. Since our macropore network only constitutes of porosity along grain edges and corners, our numerically determined macroporosity and permeability from the

Brae Formation sandstone can be directly compared to the raw data from these studies.

In the six samples where we were able to identify an effective porosity, the permeability varied by two orders of magnitude between 7.6 mD and 795.0 mD. We compare the data from the simulations in this study with previous simulation results (e.g. Thomson et al. (2019)) and laboratory experiments (Bourbié and Zinszner, 1985; Doyen, 1988; Gomez et al., 2010; Madonna et al., 2013; Revil et al., 2014) in Figure 8. In this plot, we overlay a fit of the Kozeny-Carman relation $k = k_0\phi^n$ to the simulation data from this study and Thomson et al. (2019). The values of the parameters k_0 and n are annotated on the plot. The porosity exponent (n) within the range of our numerical simulations is 3.67, quite similar to the value of 3.8 obtained by Doyen (1988). While the porosity exponents of the modified Kozeny-Carman relation from the study of Gomez et al. (2010) and Revil et al. (2014) are not directly comparable to our fit, we find that the raw data of these studies are largely similar. We also created a fit of permeability as a function of effective porosity, which yielded a slightly lower porosity exponent of 3.3. As discussed earlier, at porosities $< 10\%$, the slope becomes steeper. While the permeability measurements from our models agree quite well with previous empirical data and models, we recognize the fact that empirically determined values of percolation threshold may not reflect the accurate values at which connection is established. Thus, a clearer insight into the nature of porous flow in reservoir rocks can be achieved when permeability measurements are accompanied by pore network models.

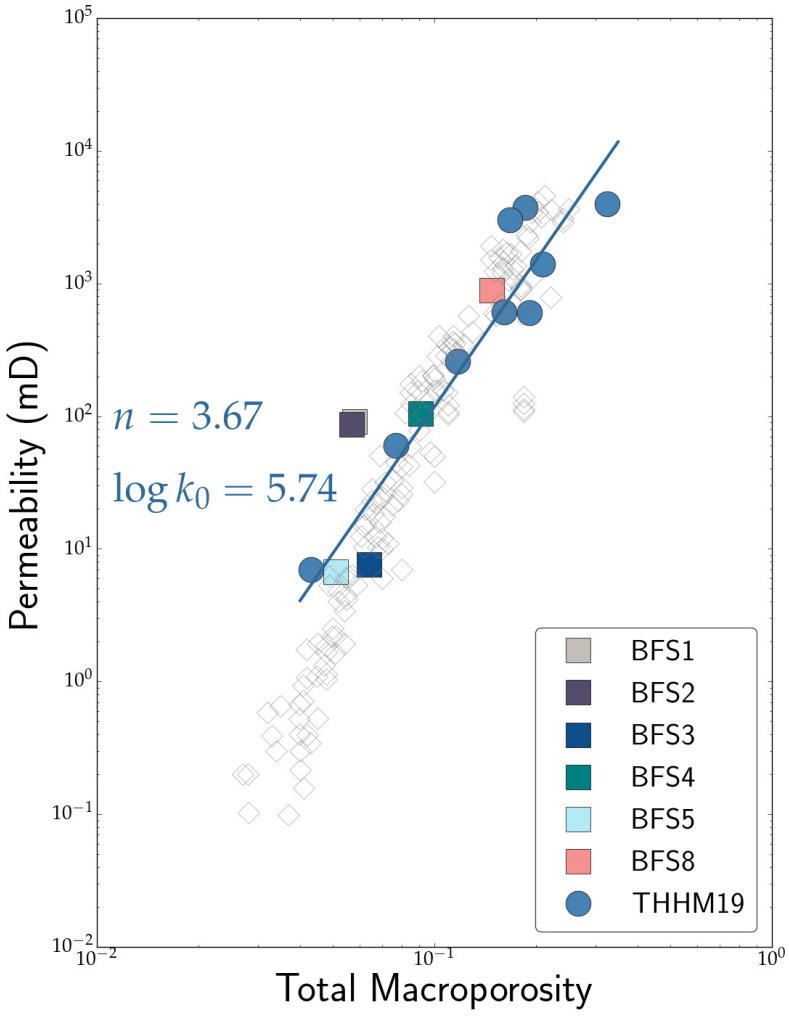

Figure 8: Plot of permeability as a function of total macroporosity. Square symbols indicate data from the measurements reported in Table 1. For comparison, we also included data points from Thomson et al. (2019), marked as THHM19 in the legends. Open symbols indicate porosity and permeability measurements from laboratory experiments of Bourbié and Zinszner (1985); Doyen (1988); Gomez et al. (2010); Madonna et al. (2013) and Revil et al. (2014). The solid line is a fit to the data with filled symbols of the form $k = k_0\phi^n$, where k is permeability, measured in mD, k_0 is a constant, ϕ is total macroporosity, and n is the porosity exponent.

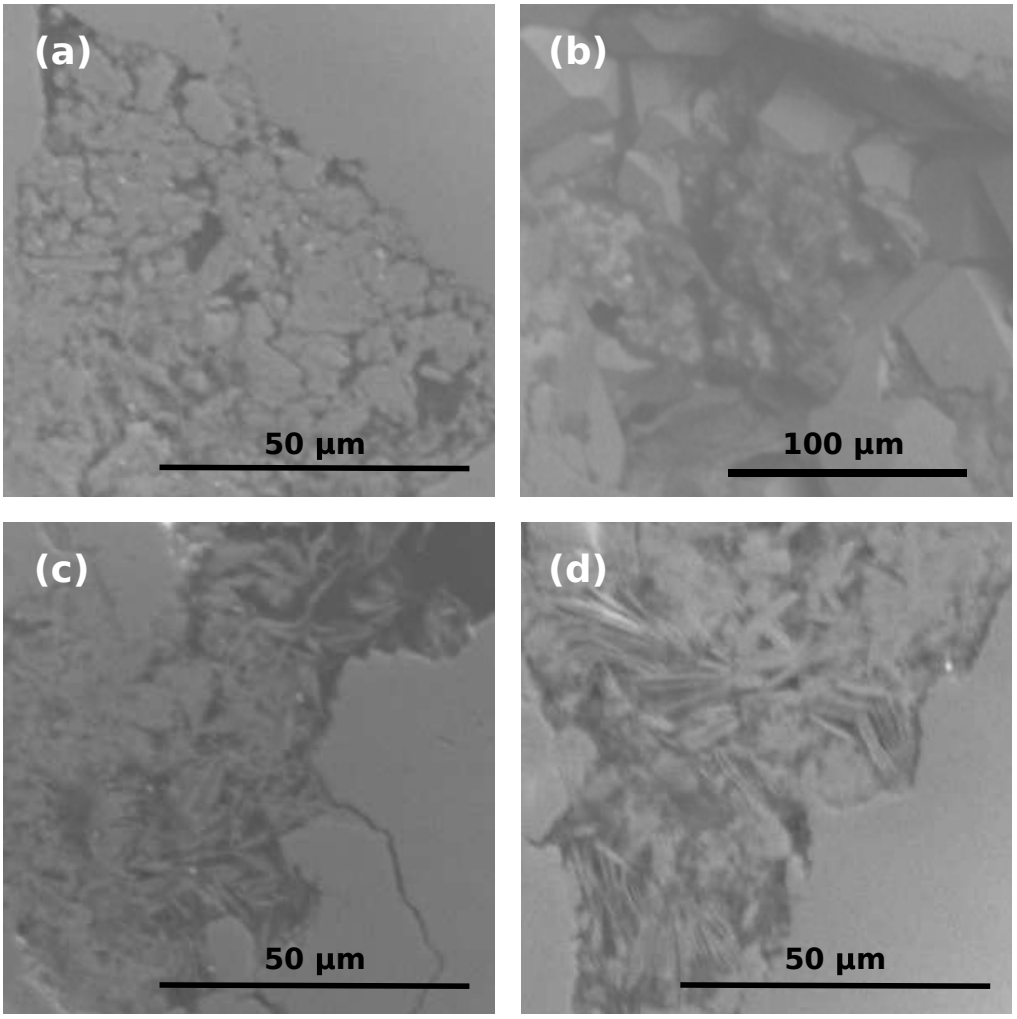

Figure 9: SEM images showing examples of microporosity below resolution of micro-CT images used in this study. (a) BFS1 with fragmented rock particles and void spaces in between individual grains, (b) BFS 6 showing micro quartz, and fibrous growths in (c) BFS4 and (d) BFS8.

4.2. Microporosity

In the North Sea, at depths of greater than roughly 2500 m, quartz and calcite cementation is considered the main porosity-reducing process (Bjørlykke et al., 1992; Giles et al., 1992; Lu et al., 2011; Marcussen et al., 2010). Micro quartz cements range between 3 and 15% while calcite cements range between 0 and 4% in zones that are devoid of calcite concretions and between 20 to 40% in calcite concretion zones (Lu et al., 2011). In addition, the Brae formation sandstones can contain up to 8% clay, muscovite and lithic fragments. These secondary and accessory phases act as sites of microporosity, which can be sampled by bulk porosity measurements but do not participate in fluid percolation.

In agreement with previous studies on the Brae Formation, our samples contain variable amounts of microporosity, typically associated with clay minerals and secondary mineral phases. While a detailed evaluation of the microporosity is outside the scope of this article, we present some Scanning Electron micrographs of several regions of interest in samples BFS1 (a), BFS6 (b), BFS4 (c) and BFS8 (d) in Figure 9. The images in Figure 9(a) and (b) show macropore spaces partially filled with microcrystals, rendering the individual pore into a microporous region. The presence of these microcrystals supports previous observation of micro-quartz coating in the Miller field sandstones (Aase and Walderhaug, 2005). Figure 9(c) and (d) both show the void space filled by a fibrous texture. These micrographs demonstrate the abundance of microporosity in our samples.

One of the key challenges in micro-CT analysis of porous media is the inclusion of microporosity for accurate porosity and permeability measure-

ments. In recent years, several efforts have been made to include porosity at both macro and micro scale using dual-scale models (*e.g.* Bultreys et al. (2016); Mehmani et al. (2019); Mehmani and Prodanović (2014); Soulaine et al. (2016). An alternative approach is to assess the upper and lower limits of the influence of microporous cements on permeability (Thomson et al., 2019). The lower limit, like in this article, considers the micropores as completely impermeable, and fluid flow is only modeled through the macropore network. Since the micropore spaces between microcrystals and fibrous textures are beyond the detection limit of the scanner, we treated these microporous regions as part of the solid matrix during image segmentation. The analysis involving the upper limits considers the micropores as completely void and 100% permeable. While this does not directly quantify the the influence of microporosity, it provides a margin of error for permeability measurements using digital methods. The findings of the upper bounds are reported in a forthcoming publication (Thomson et al., 2020). In contrast, low viscosity Helium gas used in Helium pycnometry can penetrate these microporous regions and incorporates the volume of pore space included in the microporosity. As the results from the Helium pycnometry measurements indicate, these samples contain a significant amount of microporosity.

4.3. Depositional environment and DRP

The 3D micro-CT image analysis indicates that samples from the core that was recovered from well 16/7b-20 have a more homogeneous internal organization compared to the samples from well 16/7b-23. The reason for such variability in facies and porosity can be attributed to deposition in two different regions within the same depositional area. In particular, the core

from well 16/7b-23 penetrates a more proximal area, possibly characterized by higher lateral and vertical facies variability, and moderately sorted sediments. Conversely, although the two wells are located relatively close (∼2 km) to each other (Figure 1B), the core from well 16/7b-20 penetrates an area relatively more distal, sourced from a lateral entry point, and characterized by more mature and well sorted sediments.

This study illustrates variations in macroporosity in a number of sandstone samples at increasing depths across two cored wells in the Miller field complex of the North Sea, South Viking Graben. This area is known for its large regional variation in reservoir quality of deeply buried (> 4000 m) sandstones belonging to the Upper Jurassic syn-rift sequences. Despite these sandstones having similar texture and mineralogy throughout the area, the porosities are known to range between 5% and 25% (Maast et al., 2011). Our porosity measurements fall within this range and we observe some sample intervals with greater porosities and permeabilities occurring at greater depths (e.g. BFS4 and BFS8), while others (e.g. BFS3) are from shallower intervals and display much reduced porosity and permeability.

4.4. Implications of pore network connectivity

As the demand for hydrocarbons is expected to continue into the near future and we look to use preexisting reservoirs as potential depositories for CO_2 and other waste products, it is crucial to have a better understanding of pore network connectivity and its control on the rocks ability to store fluid and permit flow. The observations and results of this study indicate the important implications of pore network connectivity for predicting reservoir quality and performance in subsurface formations. Rock formations contain-

ing intervals of relatively poor reservoir quality (between 3 and 10% porosity) are undesirable during conventional hydrocarbon production as these can act as baffles to fluid flow, however these may be much more attractive during CO_2 injection, when the goal is for long term storage in the subsurface. On the other hand, formations with good reservoir quality, those with porosity exceeding 10%, will be expected to perform much better during oil and gas production, and can also form more favourable targets for CO_2 storage projects, particularly if the sealing capacity is high and there is low potential for CO_2 to breach and escape the formation. The understanding of pore network connectivity plays an essential role in predicting the reservoir performance of deeply buried rock formations.

While our hypothesis of the three regimes are robust for the scale of resolution of the images, it needs to be further tested. Future work on the relationship between effective porosity and total porosity—determined from multiple resolutions and length scales—will be crucial to determine a number of factors. First, such studies will be able to identify the possible existence of any correlation between the length scales of samples and the boundaries of the three regimes reported above. Second, the existence of such studies will be able to identify the length-independent representative elementary volume (REV) for such samples. Finally, the knowledge of the REV will allow extrapolation and upscaling of these results to reservoir scale simulations.

5. Conclusions

We studied the macropore network characteristics from 8 samples of Brae Formation sandstone from the South Viking Graben in the North Sea. Our

results show that the samples contain variable amounts of micro and macroporosity. Our pore network analysis indicates three regimes of pore network connection. At macroporosity values $< 3\%$, the macropore network becomes disconnected, while full connection is achieved at total porosities above 10%. Permeability of the rocks vary between 7.6 and 795.0 mD, with a Kozeny-Carman porosity exponent of 3.67. The pore network connectivity regimes and the permeability results agree well with existing measurements on sandstones.

Acknowledgments

P-RT acknowledges support from a NERC Oil and Gas CDT graduate fellowship (grant number NE/M00578X/1). This research was also supported by the grant EAR125880 from the US National Science Foundation.

References

Aase, N. E. and Walderhaug, O. (2005), 'The Effect of Hydrocarbons on Quartz Cementation: Diagenesis in the Upper Jurassic Sandstones of the Miller Field, North Sea, Revisited', Petroleum Geoscience **11**(3), 215–223.

Bernabé, Y., Li, M. and Maineult, A. (2010), 'Permeability and Pore Connectivity: A New Model Based on Network Simulations', Journal of Geophysical Research: Solid Earth **115**(10), 1–14.

Bertei, A. and Nicolella, C. (2011), 'Percolation Theory in SOFC Composite Electrodes: Effects of Porosity and Particle Size Distribution on Effective

Properties', Journal of Power Sources **196**(22), 9429–9436.
URL: *http://dx.doi.org/10.1016/j.jpowsour.2011.06.087*

Bjørlykke, K., Nedkvitne, T., Ramm, M. and Saigal, G. C. (1992), 'Diagenetic Processes in the Brent Group (Middle Jurassic) Reservoirs of the North Sea: An Overview', Geological Society, London, Special Publications **61**(1), 263–287.

Bourbié, T. and Zinszner, B. (1985), 'Hydraulic and Acoustic Properties as a Function of Porosity in Fontainebleau Sandstone', Journal of Geophysical Research **90**(B13), 11524–11532.

Buades, A., Coll, B. and Morel, J.-M. (2008), 'Nonlocal Image and Movie Denoising', International Journal of Computer Vision **76**(2), 123–139.
URL: *https://doi.org/10.1007/s11263-007-0052-1*

Buades, a., Coll, B. and Morel, J. M. (2010), 'Image Denoising Methods. A New Nonlocal Principle', SIAM Review **52**(1), 113–147.

Bultreys, T., Stappen, J. V., Kock, T. D., Boever, W. D., Boone, M. A., Hoorebeke, L. V. and Cnudde, V. (2016), 'Investigating the Relative Permeability Behavior of Microporosity-Rich Carbonates and Tight Sandstones with Multiscale Pore Network Models', Journal of Geophysical Research: Solid Earth **121**(11), 7929–7945.

Doyen, P. M. (1988), 'Permeability, Conductivity, and Pore Geometry of Sandstone', Journal of Geophysical Research **93**(B7), 7729.
URL: *http://doi.wiley.com/10.1029/JB093iB07p07729*

587 Giles, M., Stevenson, S., Martin, S., Cannon, S., Hamilton, P., Marshall,
588 J. and Samways, G. (1992), 'The Reservoir Properties and Diagenesis of
589 the Brent Group: A Regional Perspective', Geological Society, London,
590 Special Publications **61**(1), 289–327.

591 Gomez, C. T., Dvorkin, J. and Vanorio, T. (2010), 'Laboratory Measure-
592 ments of Porosity, Permeability, Resistivity, and Velocity on Fontainebleau
593 Sandstones', Geophysics **75**(6), E191.

594 Iassonov, P., Gebrenegus, T. and Tuller, M. (2009), 'Segmentation of X-
595 ray Computed Tomography Images of Porous Materials: A Crucial Step
596 for Characterization and Quantitative Analysis of Pore Structures', Water
597 Resources Research **45**(9).

598 Ketcham, R. A. and Carlson, W. D. (2001), 'Acquisition, Optimization and
599 Interpretation of X-ray Computed Tomographic Imagery: Applications to
600 the Geosciences', Computers and Geosciences .

601 Lindquist, W. B., Venkatarangan, A., Dunsmuir, J. and Wong, T.-f. (2000),
602 'Pore and Throat Size Distributions Measured from Synchrotron X-ray
603 Tomographic Images of Fontainebleau Sandstones', Journal of Geophysical
604 Research: Solid Earth **105**(B9), 21509–21527.
605 **URL:** *https://agupubs.onlinelibrary.wiley.com/doi/abs/10.1029/2000JB900208*

606 Lu, J., Wilkinson, M., Haszeldine, R. S. and Boyce, A. J. (2011), 'Carbonate
607 Cements in Miller Field of the UK North Sea: A Natural Analog for Min-
608 eral Trapping in CO2 Geological Storage', Environmental Earth Sciences
609 **62**(3), 507–517.

Maast, T. E., Jahren, J. and Bjørlykke, K. (2011), 'Diagenetic Controls on Reservoir Quality in Middle to Upper Jurassic Sandstones in the South Viking Graben, North Sea Diagenetic Controls on Reservoir Quality in the South Viking Graben Sandstones', AAPG bulletin **95**(11), 1883–1905.

Madonna, C., Quintal, B., Frehner, M., Almqvist, B. S. G., Tisato, N., Pistone, M., Marone, F. and Saenger, E. H. (2013), 'Synchrotron-Based X-ray Tomographic Microscopy for Rock Physics Investigations', Geophysics **78**(1), D53–D64.
URL: *http://library.seg.org/doi/abs/10.1190/geo2012-0113.1*

Marchand, A. M., Haszeldine, R. S., Smalley, P. C., Macaulay, C. I. and Fallick, A. E. (2001), 'Evidence for Reduced Quartz-Cementation Rates in Oil-Filled Sandstones', Geology **29**(10), 915–918.

Marcussen, Ø., Maast, T. E., Mondol, N. H., Jahren, J. and Bjørlykke, K. (2010), 'Changes in Physical Properties of a Reservoir Sandstone as a Function of Burial Depth–The Etive Formation, Northern North Sea', Marine and Petroleum Geology **27**(8), 1725–1735.

Mavko, G. and Nur, A. (1997), 'The Effect of a Percolation Threshold in the Kozeny-Carman Relation, Gary Mavko and Amos Nur ', Geophysics **62**(5), 1480–1482.

McClure, N. and Brown, A. (1992), 'Miller Field: A Subtle Upper Jurassic Submarine Fan Trap in the South Viking Graben, United Kingdom Sector, North Sea: Chapter 20'.

Mehmani, A., Milliken, K. and Prodanović, M. (2019), 'Predicting Flow Properties in Diagenetically-Altered Media with Multi-Scale Process-Based Modeling: A Wilcox Formation Case Study', Marine and Petroleum Geology **100**, 179–194.

Mehmani, A. and Prodanović, M. (2014), 'The Effect of Microporosity on Transport Properties in Porous Media', Advances in Water Resources **63**, 104–119.

Otsu, N. (1979), 'A Threshold Selection Method from Gray-Level Histograms', IEEE Transactions on Systems, Man, and Cybernetics **9**(1), 62–66.

Pal, N. R. and Pal, S. K. (1993), 'A Review on Image Segmentation Techniques', Pattern recognition **26**(9), 1277–1294.

Revil, A., Kessouri, P. and Torres-Verdín, C. (2014), 'Electrical Conductivity, Induced Polarization, and Permeability of the Fontainebleau Sandstone', Geophysics **79**(5), D301–D318.
URL: *http://library.seg.org/doi/10.1190/geo2014-0036.1*

Rooksby, S. K. (1991), The Miller Field, Blocks 16/7B, 16/8B, UK North Sea, in 'United Kingdom Oil and Gas Fields, 25 Years Commemorative Volume', Vol. 14, pp. 159–164.

Sezgin, M. and Sankur, B. (2004), 'Survey Over Image Thresholding Techniques and Quantitative Performance Evaluation', Journal of Electronic imaging **13**(1), 146–166.

Soulaine, C., Gjetvaj, F., Garing, C., Roman, S., Russian, A., Gouze, P. and Tchelepi, H. A. (2016), 'The Impact of Sub-Resolution Porosity of X-ray Microtomography Images on the Permeability', Transport in Porous Media **113**(1), 227–243.

Thomson, P.-R., Aituar-Zhakupova, A. and Hier-Majumder, S. (2018), 'Image Segmentation and Analysis of Pore Network Geometry in Two Natural Sandstones', Frontiers in Earth Sciences **6**(June), 1–14.
URL: *https://www.frontiersin.org/articles/10.3389/feart.2018.00058/full*

Thomson, P.-R., Ellis, R., Chiarella, D. and Hier-Majumder, S. (2020), 'Microstructural Analysis from X-ray CT Images of the Brae Formation Sandstone, North Sea', Frontiers in Earth Science (in review) .

Thomson, P.-R., Hazel, A. and Hier-Majumder, S. (2019), 'The Influence of Microporous Cements on the Pore Network Geometry of Natural Sedimentary Rocks', Frontiers in Earth Science **7**, 48.
URL: *https://www.frontiersin.org/article/10.3389/feart.2019.00048*

Trier, Ø. D. and Jain, A. K. (1995), 'Goal-Directed Evaluation of Binarization Methods', IEEE Transactions on Pattern Analysis & Machine Intelligence (12), 1191–1201.

Turner, C. C. and Cronin, B. T. (2018), 'The Brae Play, South Viking Graben, North Sea; An Introduction'.

van de Lagemaat, J., Benkstein, K. and Frank, A. (2001), 'Relation Between Particle Coordination Number and Porosity in Nanoparticle Films: Im-

plications to Dye-Sensitized Solar Cells', Journal of Physical Chemistry B **105**(50), 12433–12436.

Watson, H. C. and Roberts, J. J. (2011), 'Connectivity of Core Forming Melts: Experimental Constraints from Electrical Conductivity and X-ray Tomography', Physics of the Earth and Planetary Interiors **186**(3-4), 172–182.
URL: *http://dx.doi.org/10.1016/j.pepi.2011.03.009*

Wildenschild, D., Vaz, C., Rivers, M., Rikard, D. and Christensen, B. (2002), 'Using X-ray Computed Tomography in Hydrology: Systems, Resolutions, and Limitations', Journal of Hydrology **267**(3-4), 285–297.

Wimert, J. T. and Hier-Majumder, S. (2012), 'A Three-Dimensional Micro-geodynamic Model of Melt Geometry in the Earth's Deep Interior', Journal of Geophysical Research-Solid Earth **117**(B04), B04203.

Youssef, S., Rosenberg, E., Gland, N., Kenter, J., Skalinski, M. and Vizika, O. (2007), 'High Resolution CT and Pore-Network Models to Assess Petrophyscial Properties of Homogeneous and Heterogeneous Carbonates', PE/EAGE Reservoir Characterization and Simulation Conference p. 12.

Zou, R., Bian, X., Pinson, D., Yang, R., Yu, A. and Zulli, P. (2003), 'Coordination Number of Ternary Mixtures of Spheres', Particle & Particle Systems Characterization **20**(5), 335–341. 4th World Congress on Particle Technology (WCPT4), Sydney, Australia, July 21-25, 2002.

Chapter 6

Microstructural Analysis from X-ray CT Images of the Brae Formation Sandstone, North Sea

Description. This chapter is presented in manuscript format and is published in Earth and Planetary Materials, a section of the journal Frontiers in Earth Science. Using the Brae Formation images, 3D grain size analysis is performed on the segmented grain phase to assess any relationship with porosity and permeability. Additionally, there is a focus on the presence of a cement phase, known to be abundant in these rocks and many North Sea reservoir rocks. Similarly, to previous work, the proportion of this phase is quantified and discussed in relation to its influence on reservoir quality by modelling scenarios before and after cementation. The results from the grain size analysis show that these rocks are medium grained sandstones with mean grain size in the range 315 524 um. With the small range of measurements from the samples, it was not possible to identify any trends between grainsize, porosity and permeability. However, compared to previous studies, the grainsize results do agree well with more global trends. Using the models to test the theoretical bounds of the cement phase, a negative impact on both porosity and permeability is identified. Above a threshold cement volume fraction of $\sim$5.5% the connectivity of the pore network is disabled and porous flow is no longer possible.
Author contribution. Paul-Ross Thomson performed the image filtering and

segmentation, conducted the image analysis, interpreted the data, generated most figures and wrote most of the manuscript.

frontiers in Earth Science

ORIGINAL RESEARCH
published: 02 July 2020
doi: 10.3389/feart.2020.00246

Microstructural Analysis From X-Ray CT Images of the Brae Formation Sandstone, North Sea

*Paul-Ross Thomson, Rory Ellis, Domenico Chiarella and Saswata Hier-Majumder**

Department of Earth Sciences, Royal Holloway University of London, Egham, United Kingdom

During deposition and subsequent diagenesis, reservoir rocks develop sediment texture and cement phases are formed during the precipitation of secondary minerals such as microcrystalline quartz, calcite and clay fibrous over-growths that contain secondary porosity. The grain size distribution and presence of secondary microporous material can influence the reservoir porosity and permeability. Using 3D X-ray microtomographic images we analyze the grains and pore space in Brae Formation sandstones from the South Viking Graben in the North Sea. The samples—derived from two cored wells (16/7b-20 and 16/7b-23), and located within the depth interval between 4,040 m and 4,064 m—display mean grain sizes between 315 and 524 microns (1.78–1.05 ϕ units), classifying them as predominantly medium-grained sands, with moderate to well-sorting (0.51–0.7 ϕ units). From our models we calculate the upper and lower bounds of the micropores on the pore connectivity and permeability. Our samples show total porosities between 10 and 18% of which 6 and 13% are effective, leading to a permeability range between 1 and 400 mD through the effective macropore network. We found that the fraction of effective porosity and effective permeability shows a non-linear reduction with increase in microporous cement volume fraction. Above a threshold cement volume of approximately 5.5% the effective pore network is disconnected and percolation is no longer possible. Based on our observations and modeling results we propose that cement precipitation can be a positive consequence of mineral trapping from sequestered CO_2, which can be important for reducing reservoir quality and ensuring efficient long term storage.

Keywords: digital rock physics, 3D grain size, porosity, microporosity, cementation, Brae Formation sandstone, permeability, petrophysics

OPEN ACCESS

Edited by:
Alejandro Fernandez-Martinez, Centre National de la Recherche Scientifique (CNRS), France

Reviewed by:
Matthew Louis Whitaker, Stony Brook University, United States
Martin Charles Wilding, Sheffield Hallam University, United Kingdom

****Correspondence:***
Saswata Hier-Majumder
pr.thomson.2013@gmail.com; paul-ross.thomson.2016@rhul.ac.uk

Specialty section:
This article was submitted to Earth and Planetary Materials, a section of the journal Frontiers in Earth Science

Received: *15 January 2020*
Accepted: *04 June 2020*
Published: *02 July 2020*

Citation:
Thomson P-R, Ellis R, Chiarella D and Hier-Majumder S (2020) Microstructural Analysis From X-Ray CT Images of the Brae Formation Sandstone, North Sea. Front. Earth Sci. 8:246. doi: 10.3389/feart.2020.00246

1. INTRODUCTION

The South Viking Graben is an important hydrocarbon bearing region in the North Sea. One of the several oil fields in this region is the Miller field, located within the UK sector of the North Sea. The main hydrocarbon bearing reservoir in the Miller field is the Jurassic Brae Formation sandstone (Rooksby, 1991; Maast et al., 2011). Consisting primarily of submarine fan deposits, the Brae Formation sandstones are characterized by relatively high porosity (Rooksby, 1991) with secondary mineral phases such as microcrystalline quartz and calcite occupying grain surfaces and pore spaces (Aase and Walderhaug, 2005; Lu et al., 2011; Maast et al., 2011). These secondary phases contain microporosity, which can influence the effective permeability of the rock. While the oil production

in the Miller Oil field ceased in 2007, due to the high porosity and existing infrastructure, this field can be potentially used as a future location for deep geological carbon sequestration (Lu et al., 2009). For such future applications, it is important to identify the factors that control the reservoir qualities such as porosity and permeability of the Brae Formation sandstones.

While a number of previous studies looked into the large scale reservoir properties of the Brae Formation sandstone (Rooksby, 1991; Maast et al., 2011) or the nature of secondary phases (Aase and Walderhaug, 2005; Lu et al., 2011; Maast et al., 2011), quantitative, 3 dimensional grain scale analysis of the Brae Formation sandstones remain relatively scarce. We aim to bridge this gap in this article and a companion article (Thomson et al., 2020) by studying core samples from two wells within the western sector (16/7b) of the Miller field. In the companion article, we reported the characteristics of 3D pore network and identified the connection threshold of the macroporous network in the Brae Formation and a suite of other similar sandstones. In this study, we focus on the grain size distribution and the influence of microporosity on the permeability of the Brae Formation rocks.

The reservoir quality (porosity and permeability) of sandstones is strongly influenced by sediment texture (i.e., grain size and sorting; Beard and Weyl, 1973; Scherer, 1987a,b) and diagenetic features such as secondary cementation (Worden, 1998). One component of texture, grain size distribution, defined as the distribution of the grain diameters and their sorting, is an important variable in classifying sedimentary rocks. Grain size distribution provides useful information about the depositional history and the sediment source supply (Klovan, 1966; Visher, 1969; Joseph et al., 1998; Browne et al., 2005), as well as influencing the permeability of the rock. While traditional measurements of grain size from microstructures were carried out on two-dimensional optical or electron microscopic images (Maast et al., 2011), the availability of microtomographic imaging provides an opportunity to measure grain shape attributes in three dimensions. In addition, measurements of porosity and permeability from the same images allows direct correlations between grain size distribution and reservoir properties.

The Brae Formation sandstone is characterized by a distal submarine-fan setting, fine to coarse grained quartzitic composition and diagenetic overprint, with calcite concretions, pyrite precipitates and quartz overgrowth (Rooksby, 1991; Turner and Allen, 1991; Garland, 1993; Gluyas et al., 2000; Marchand et al., 2000). While the previous studies of the secondary phases in the Brae Formation sandstone provide a wealth of information regarding the nature of the deposits and their relation with the primary pore space, relatively little attention has been paid on the influence of the secondary or microporosity on the permeability of the Brae Formation.

Microporosity can exert a significant influence on the effective permeability of reservoir rocks (Bultreys et al., 2016b; Thomson et al., 2019). Traditionally, estimates of permeability can be achieved by several methods. Well flow tests can provide useful information at reservoir scale, while gas or liquid permeability experiments in the laboratory provide estimates at core scale. Although physical experiments can likely access microporosity and provide measurements of fluid flow in a dual-porosity system, these techniques do not provide quantitative data on the volume of micropores or how much these pores contribute to fluid flow within reservoir rocks. Over the last two decades, the use of micro CT techniques has increased in popularity within pore scale research. These methods have provided better understanding for pore scale physics and the technology continues to develop quickly. However, the image resolution and selection of an appropriate representative elementary volume from which both pore types (macro and micro) can be sampled, remains challenging (Mehmani and Prodanović, 2014; Bultreys et al., 2016b; Thomson et al., 2019).

In the absence of 3D images of the micropore network, we establish the upper and lower bounds on the influence of the micropores on the permeability. Following the method outlined by Thomson et al. (2019), we treat the microporous secondary phase as two end members, one consisting entirely of void space, and the other entirely solid. This approach, commonly employed in determining effective elastic properties of porous media (Mavko et al., 2009), allows the establishment of a framework for future, high resolution microtomographic studies of direct determination of micropore network characteristics and the resultant permeability. We segment and analyze the micro CT images of eight sandstone samples from these two wells to quantify the volume fraction and connectivity of the macro and micropore spaces, measure the 3D grain size characteristics, and explore the relationship between grain size and reservoir properties.

2. METHODS

For this work, we chose four different sample intervals from two cores from two wells originating from the Brae/Miller field area. From each sample interval, we drilled one 5 mm diameter core plug to acquire X-ray micro-CT images at the Imaging and Analysis Centre at The London Natural History Museum. For more information on this process, we refer the reader to the companion article, Thomson et al. (2020). The stacked raw images obtained from the acquisition process are filtered and segmented to separate the key phases using the software PerGeos from Thermo Fisher Scientific. We outline further details of each of these steps in the following text.

2.1. Image Processing

The image acquisition process can result in a variety of unwanted features in the final stack of tiff images. The most prevalent artifact is beam hardening, which creates edges of the samples that appear brighter than the center, even when the material remains the same. Another common feature of the scanning process is the presence of ring artifacts centered on the rotational axis of the sample (Ketcham and Carlson, 2001; Wildenschild et al., 2002).

The first step to reduce the impact of such features in the samples, was to extract a sub-volume from the raw data. We set the region of interest (ROI) to 1,300×1,300×1,850 voxels (2.6×2.6×3.7 mm) and 730×630×930 voxels (2.8×2.5×3.6 mm) for samples with voxel dimensions of 2.0 and 3.9 μm^3, respectively. This permitted a large sample area for grain

TABLE 1 | Summary of sample data used in this study, including sample name, depth interval, total porosity, macro and microporosity, permeability, associated well and voxel resolution.

Sample	Depth (m)	Total porosity (%)	Macro porosity (%)	Micro porosity (%)	Total permeability (mD)	Macro permeability (mD)
BFS1[a]	4040.10	11.2 (±0.2)	7.3	3.9	395.8	127.1
BFS2[a]	4041.35	10.1 (±1.0)	6.6	3.5	124.1	70.7
BFS3[b]	4043.75	12.5 (±1.0)	9.4	3.1	149.3	21.4
BFS4[b]	4045.13	12.6 (±1.9)	9.5	3.1	339.6	110
BFS5[b]	4061	10.7 (±3.9)	6.6	4.1	37.4	1.17
BFS6[a]	4062	10.7 (±1.1)	5.4	5.3	0*	0*
BFS7[b]	4063	0	0	0	0*	0*
BFS8[a]	4063.75	17.6 (±1.3)	12.7	4.9	884.3	399.9

Samples listed on rows shaded with light gray are from the well 16/7b-20, the remaining samples are from the well 16/7b-23.
*[a]Voxel size 3.9 μm^3. [b]Voxel size 2.0 μm^3. * zero effective porosity.*

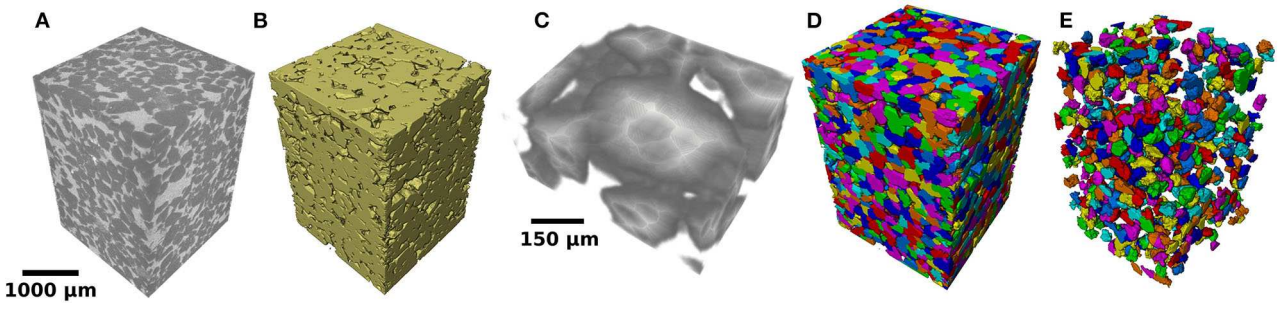

FIGURE 1 | Volume rendering visualization showing **(A)** the raw 3D data, **(B)** the segmented quartz grain phase, **(C)** a sub-volume section showing the distance map used for regional maxima computation for individual grains, **(D)** the separated quartz grains in the whole volume, and **(E)** the mean grain size ± 10% for sample BFS7.

size analysis. However, smaller ROIs were required during permeability simulation in order to reduce the computational time constraints. Further information on each sample can be found in **Table 1**.

The next step, image filtering, aims to smooth gray scale intensities of the voxels and enhance the contrast between key phases in the micro-CT images. There are a variety of image filtering techniques that deploy many different methods to efficiently remove artifacts, reduce noise and increase edges (Schlüter et al., 2014). In this work, we used the non-local means filter to effectively despeckle and maintain contrast between grains and pores (Buades et al., 2008, 2010). Unlike many other linear methods (e.g., Gaussian, mean filter, etc.), this filter is not limited by a small sized kernel, meaning that the entire image may be used as a search window in the final weighting stage for gray scale determination of each voxel. A large search window dramatically increases the computational time for the filtering process and can lead to the removal of key features as a result of excessive smoothing. We used the default search window size to maintain a balance between processing time and quality image filtering.

The final stage of image processing is segmentation, the individual separation of each phase. During this process, the different phases are separated based on their gray scale intensity values, which are related to material density, atomic number and the energy of the X-rays. The process of image segmentation can be either automated (Ridler and Calvard, 1978; Otsu, 1979) or manual, based on gray scale histogram evaluation alone. The process is most commonly completed manually due to small but consistent over or underestimated values from automated schemes (Iassonov et al., 2009; Wildenschild and Sheppard, 2013; Bultreys et al., 2016a). Inconsistent results from automated techniques arise from samples that have multiple phases with similar gray scale intensity and/or significant image noise (Thomson et al., 2018). We chose to use a manual thresholding technique, assigning voxels in the 3D ROI to labels that we interpreted the material belong to (e.g., pore or grain). **Figure 1A** shows the contrast between the grain phase (dark gray) and the cement phase (light gray) in one of the samples.

Volume fraction measurements for different materials in the samples are obtained from the 3D volumes generated as a result of the segmentation process. In total, we generated four label fields from the four key materials that are present within each sample. Phases with the lowest gray scale intensity through to those with the highest gray scale intensity, are identified as macroporosity, microporosity, quartz grain and other minor mineral grains. Each of these phases have a proportion of the total voxels in the volume assigned to their designated label field. While the identification of macroporosity, quartz grain and other less abundant minerals is fairly straightforward,

establishing an accurate representation of the microporosity remains challenging. To work around this complication, we adopted the approach already used in previous works (Bultreys et al., 2016b; Thomson et al., 2019), where microporosity is identified and assigned as an intermediate gray scale phase between macroporosity and quartz grain. To calculate the representative proportion of each phase, the number of voxels assigned to one label field (e.g., macroporosity) is divided by the total number of voxels in the entire sample volume.

2.2. Porosity Characterization

One key limitation of micro CT analysis is the inability to accurately determine the role of microporous material in porous geological media. There is a conflict between sample size and image resolution which prevents the quantification of both macro and micropores in a sample. We overcome this using an end-member approach to quantify the effect of microporosity hosted by microcrystalline precipitations in these rocks. We generate simple models to assess the influence of the microporous phase on the connectivity of the pore network and the control on permeability. Two extremes of pore network connectivity are assessed. At one end of the scale we assume that the microporosity is void space, and on the other, it is an impermeable solid. In reality, porosity of the microporous phase lies between these two extremes. In the absence of the information about the micropore geometry, the two end members provide us the upper and lower bounds of effective porosity and permeability. We calculate the fraction of effective macroporosity by dividing the effective macroporosity by the total macroporosity to assess the influence of the cement phase (microporous material) on the connectivity of the pore network. Similarly, we test our permeability models to assess how the ratio of permeability is controlled by the cement volume fraction. In addition, treating the microporosity in terms of the two end member cases, can also serve as a temporal analog. If the microporosity is derived from secondary cement phases, the two end members provide the geometry of the pore space before and after cementation.

2.3. Permeability Simulation

Following the segmentation of the pore space phase in each sample, the pore network is further processed to remove any isolated voxels that do not form part of the interconnected pore system between two planes of the volume. This process was performed on the long axis (Z) of each sample to provide a network of effective porespace where possible. The effective 3D pore volume was then used to simulate the absolute permeability through each of the samples. Using a finite volume solver from the Pergeos petrophysics module, we calculated the single phase flow of water by solving Stokes equation,

$$\nabla \cdot \boldsymbol{u} = 0, \tag{1}$$

$$-\nabla P + \mu \nabla^2 \boldsymbol{u} = 0, \tag{2}$$

where $\boldsymbol{u}$ is the fluid velocity vector, P is the pressure and $\mu = 1 \times 10^{-3}$ Pa.s is the viscosity of water. With the exception of the 3D pore volume of the effective network, all boundary conditions (as described in Thomson et al., 2018) and parameters were kept constant. Similarly to previous work by Thomson et al. (2019) we ensured that the convergence criterion or error, ϵ, was set to a predetermined value for $\epsilon \leq 10^{-6}$. This parameter is particularly important as it determines the computational cost and accuracy of permeability results.

2.4. Grain Size Measurements

Following the process of segmentation of the quartz grain phase (**Figure 1B**), 3D grain volumes are obtained for further analysis. The goal of this analysis is to obtain quantitative data on the grain size. To achieve this goal, the 3D grain volume has to be handled using a number of image processing steps. The watershed algorithm is key to this analysis and is a powerful method that allows automated separation of the grains and/or pores (Youssef et al., 2007). The process of grain separation is described in the following steps:

- The 3D label field for the grain phase, generated during segmentation described in section 2.1, is used to compute a distance map (e.g., **Figure 1C**). The distance map is created by assigning a value to each voxel within a grain. The value for each voxel corresponds to its distance to the background, which in this case, is the pore space. The distance map provides the "input priority map" for the watershed process.
- Next, the distance map is used to compute the regional maxima, located at the most inner region of the grains. A new label field is created containing markers at the center of the grains. These marker regions are used as seed areas for flooding during the watershed.
- The watershed algorithm then expands the marker regions toward increasing values of the input priority map, so the distance map has to be inverted first. The marker-based watershed algorithm is applied, ensuring that the inverted distance map and maxima labels are connected.
- Finally, the watershed image is used to generate separation lines. These separation lines are subtracted from the original 3D label field for the grain phase to produce a new 3D image containing individual separated grains. The 3D separated grain image is converted to a label image (**Figure 1D**) and processed using the label analysis tool to provide 3D Feret diameters of the grains.
- The 3D grain label images can be filtered to show the proportion of a particular grain size in the sample. **Figure 1E** shows the mean grain size $\pm$ 10% for sample BFS7.

The grain size measurements obtained from the grain separation algorithm are used to quantify the degree of sorting and classify the samples. Due to the sensitivity of the algorithm, the data is not completely free from errors. Some measurements, arising from small scale noise in the gray scale intensity of the images, are present in the data that do not fall within the expected range for sandstone sediments. Since the primary focus of this study is the analysis of quartz grains, we remove small scale noise in our data by filtering the results based on the Wentworth (1922) grain size classification for sediments, to exclude grain size measurements < 63 μm. This provided us with data that displayed characteristics for very fine sands and above.

TABLE 2 | Summary of grain size analysis, including mean and median grain size, sorting, and skewness.

Sample	Mean grain size (μm)	Median grain size (μm)	Mean grain size (M_Z) (ϕ)	Median grain size (ϕ)	Sorting (ϕ_1)	Skewness (Sk_1)
BFS1	523.6	488	1.05	1.04	0.60	0.03
BFS2	521.2	482.3	1.05	1.05	0.57	0.01
BFS3	314.9	295.2	1.78	1.76	0.60	0.07
BFS4	381.6	346.6	1.54	1.53	0.68	0.04
BFS5	386.7	363.7	1.51	1.46	0.69	0.16
BFS6	519.7	483.6	1.06	1.05	0.56	0.02
BFS7	318.9	309.1	1.72	1.69	0.51	0.12
BFS8	461.2	434.1	1.23	1.20	0.64	0.11

Samples listed on rows shaded with light gray are from well 16/7b-20, the remaining samples (dark gray) are from well 16/7b-23.

The grain size statistics are calculated using the 3D measurement for grain length. We report some of the grain size analysis and graphical representations using phi (ϕ) units. To obtain phi units we applied a logarithmic transformation of millimeters to whole integers, using the formula:

$$\phi = -\log_2\left(\frac{d}{d_0}\right), \tag{3}$$

where d is grain diameter (3D grain length) in millimeters, and $d_0 = 1$ mm. To calculate the median grain size we use the 50 percentile where half the grains are larger and half are smaller than the median. We report the median grain size in both microns and phi units. In addition, we use the following formula from Folk (1980) to calculate the mean (average) grain size in phi units:

$$M_Z = \frac{\phi 16 + \phi 50 + \phi 84}{3}, \tag{4}$$

where $\phi 16$, $\phi 50$, and $\phi 84$ represent the grain size at 16, 50, and 84 percentiles in the data.

The grain size variation between samples can provide useful information for sediment source, transportation and comparison of petrophysical properties. Folk (1980) introduced the "inclusive graphic standard deviation" which includes 90% of the distribution and provides the best overall measure of sediment sorting. To calculate the sorting in ϕ units, the following equation is used:

$$\phi_1 = \frac{\phi 84 - \phi 16}{4} + \frac{\phi 95 - \phi 5}{6.6}, \tag{5}$$

where $\phi 95$ and $\phi 5$ represent the ϕ values at 95 and 5 percentiles. We classify the sorting of the samples based on the discrete classification scale for sorting (Folk, 1980): $\phi_1 < 0.35$: very well-sorted; 0.35–0.5: well-sorted; 0.5–0.71: moderately well sorted; 0.71–1.0: moderately sorted; 1.0–2.0: poorly sorted; 2.0–4.0: very poorly sorted; and > 4.0: extremely poorly sorted.

The skewness is used to describe the degree of asymmetry of a distribution. Samples may have similar average grain size and sorting but their degrees of symmetry may be quite different. We use the inclusive skewness equation (Folk, 1980):

$$Sk_1 = \frac{\phi 16 + \phi 84 + 2\phi 50}{2(\phi 84 - \phi 16)} + \frac{\phi 5 + \phi 95 - 2\phi 50}{2(\phi 95 - \phi 5)}, \tag{6}$$

which provides a much better statistic and includes 90% of the curve compared to other methods (e.g., Inman, 1952).

3. RESULTS

For each sample we compare the grain size characteristics, porosity and permeability. The total porosity, the proportions of macroporosity and microporosity, and the permeability are showed in **Table 1**. The mean and median grain size, sorting, and skewness statistics for each sample is displayed in **Table 2**.

3.1. Grain Size Characteristics

Our results from the 3D grain length analysis, obtained from Equation (4) show that most of the samples have a mean grain size between 2 and 1 ϕ units (250 and 500 μm). This suggests that they are typically medium-grained sandstone (Wentworth, 1922). The sample BFS1 has a mean grain size outside of this range (523.6 μm), classifying it as a coarse grained sandstone. Sorting is obtained from Equation (5). All samples are moderately to well-sorted, characterized by the narrow range of ϕ_1 values between 0.5 and 0.7. Within this small range, BFS7 has the best sorting of quartz grains, while BFS5 is the least well-sorted. The distribution of grain size is shown graphically in **Figure 2** for the four samples from conventional core from the Brae interval in exploration wells 16/7b-20 (**Figure 2A**) and 16/7b-23 (**Figure 2B**), respectively. These plots highlight that all samples have an asymmetrical distribution with a positive skewness and an apparent excess of more fine grained material. The results of the skewness analysis obtained from Equation (6) shows that all samples have values between 0.01 and 0.12, indicating near symmetrical through to fine skewed preference.

3.2. Porosity and Pore Network Analysis

A detailed analysis of the macropore network of these samples is presented in Thomson et al. (2020). In this article, we focus on the geometry of the microporosity determined by image analysis

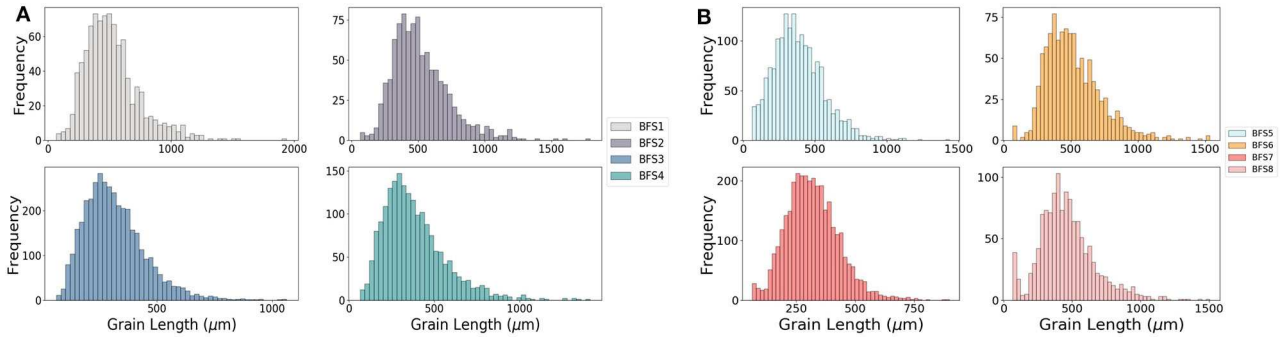

FIGURE 2 | Grain size distribution plots for samples BFS1-BFS4 from well 16/7b-23 **(A)** and samples BFS5-BFS8 from well 16/7b-20 **(B)**.

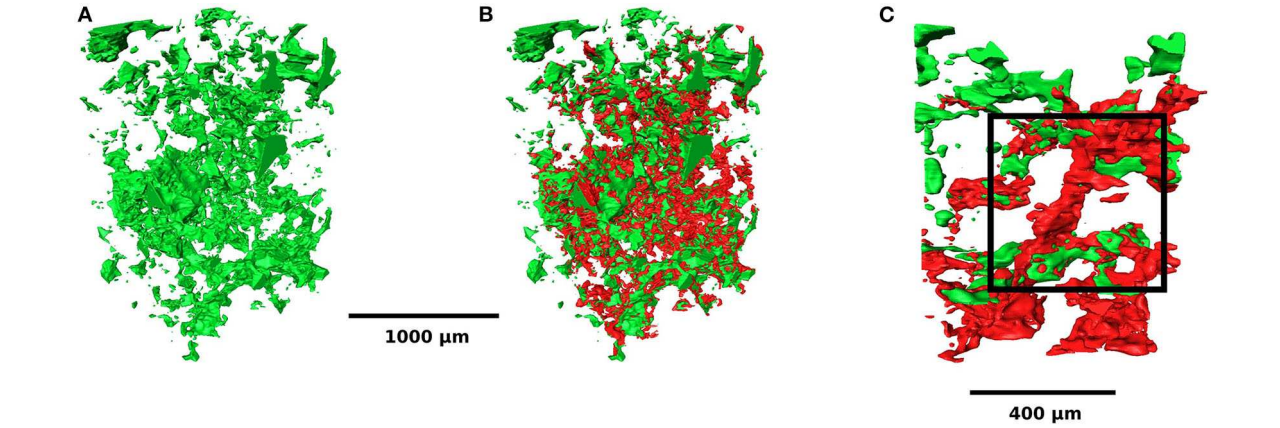

FIGURE 3 | Volume rendering visualization of the influence of cement on the pore network. Shown in sample BFS6 where green is macroporosity and red is microporosity. The poorly connected macroporosity is shown in isolation in **(A)**. The proportion of both macro and microporosity is shown in **(B)**. The microporous cement phase can effectively fill some channels between larger clusters of macropores **(C)**.

and the total porosity, calculated by adding the micro and macropore spaces. Samples from well 16/7b-20 (BFS1 through to BFS4) have total porosities of 11.2, 10.1, 12.5, and 12.6%, respectively. The average total porosity from the samples in this well is 11.6%. Samples from well 16/7b-23 show a wider range in total porosity, with one sample (BFS7), completely devoid of detectable porosity. The calculated total porosity for sample BFS5, BFS6, and BFS8 is 10.7, 10.7, and 17.6%, respectively. The average total porosity is also higher in the samples from this well with a value of 13%.

Macroporosity is the dominant void space in most of the samples. The proportion of microporosity is generally much smaller than the macroporosity, with the exception of sample BFS6, which contains almost equal amounts of macro and microporosity. **Figure 3A** demonstrates the poorly connected network of macropores in BFS6. The relative proportion of macro (green) and microporosity (red) in sample BFS6 is shown in **Figure 3B**. The influence of microporous pore-filling cements can be observed in **Figure 3C**, where larger clusters of porespace appears to become disconnected. The samples BFS3 and BFS4 have the largest share of macroporosity out of all the samples, with 75% of void space in the macropores. The sample BFS8 also has a high proportion of macroporosity, with a value of 72%. Samples BFS1 and BFS2 have a 65% proportion of macroporosity, while BFS5 has 62%.

3.3. Results From Permeability Simulations

In this article, we compare and contrast the two end member cases of permeability. In the first case, we assume that the micropore space is impermeable, and the fluid flow takes place only through the connected macropores. In the second end member case, we assume that the microporosity is void, and fluid flow takes place through the connected fraction of the total pore space. In a companion publication (Thomson et al., 2020), we reported the results of only the first end member case. While the true permeability of the rocks falls somewhere between these two limits, in the absence of higher resolution microtomographic images of the micropore space, these two limits allow us to quantify the upper and lower bounds on permeability of these microporous, cement-bearing rocks.

The results of our permeability simulations highlight the impacts of cementation on the ability of pore networks to permit fluid flow. **Figure 4** shows the volume rendering visualization of absolute permeability though BFS1: (A) total pore network,

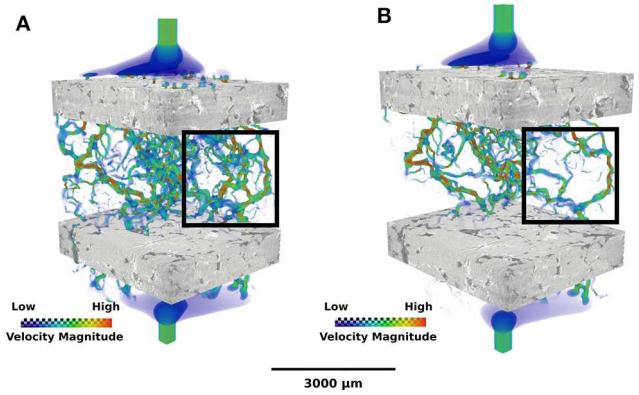

FIGURE 4 | Volume rendering visualization of the effect of microporosity on permeability in sample BFS1. **(A)** The upper limit: in this case the micropore space is considered to be completely void. The streamlines, colored by dimensionless fluid velocity, illustrate the flow pathways before cementation. **(B)** The lower limit: in this case, we consider the macropore space to be impermeable, leading to a more sparse distribution of streamlines. See **Table 1** for the permeability values for these two limits in each sample.

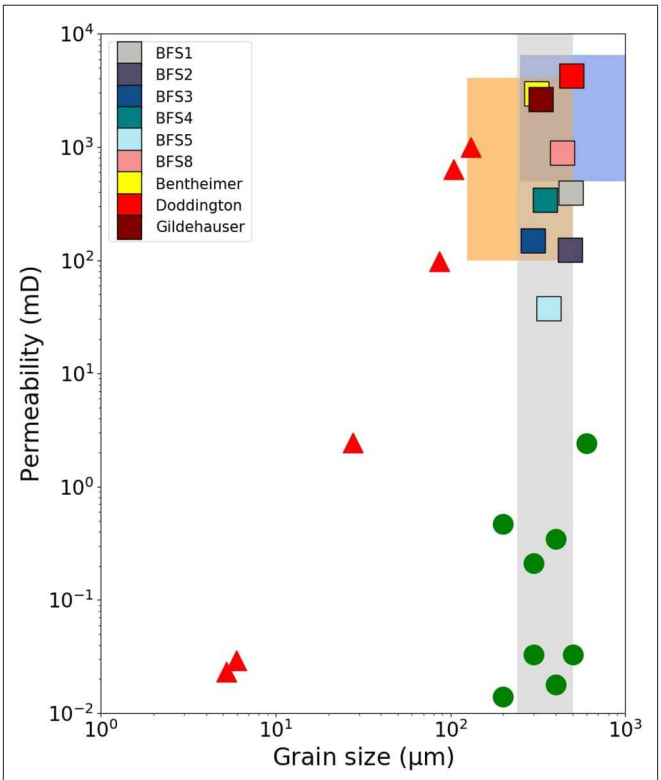

FIGURE 5 | Comparison between our data and previous studies of permeability as a function of grain size. The red triangles represent data from hydrate-free sediments (Konno et al., 2015), while the green circles represent data from tight gas sandstones (Becker et al., 2017). The shaded orange and blue regions correspond to fine to medium and medium to coarse grained intervals of the Piper Formation, respectively (Maher, 1980). The shaded gray interval is the range of grain size measurements obtained by point-count analysis for the Brae Formation (Maast et al., 2011).

where macro and microporosity form a single network; and (B) through the macropore network only. As the figure highlights, there is a greater abundance of flow pathways in the total pore network (a) compared to that of the macropore network (b). The reduced frequency of channels and diminished connectivity of the pore network has a negative impact on the rocks ability to permit fluid flow and hence the permeability measurements. **Table 1** shows the results of total and macro only permeability simulations. The total permeability (flow through the effective total pore space, the second case described above) measurements varied by one order of magnitude between 37.4 and 884.3 mD, in samples BFS5 and BFS8, respectively. The permeability measurements through effective macropores varied by two orders of magnitude between 1.17 and 399.9 mD, once again in samples BFS5 and BFS8. The maximum variation in permeability within a single sample between the total pore network and the macro only network is by one order of magnitude.

4. DISCUSSION

4.1. Comparison With Previous Measurements

The results from our measured grain size and permeability compares well with previous measurements from Brae Formation and similar rocks. As the plot in **Figure 5** displays, the grain size from our measurements agrees well with the grain size range obtained for the Brae Formation from traditional point-count analysis (Maast et al., 2011) highlighted as the gray shaded region. The variations in permeability arise from porosity variations in the samples. Despite these variations, our data does show good agreement with grain size and permeability values approximated from previous well log analysis (Maher, 1980). As the plot shows, the shaded orange and blue regions correspond to fine to medium and medium to coarse grained intervals and their relevant permeability ranges of the Piper Formation, respectively. These samples, also originating from sandstone reservoirs at depth (≈ 2,800 m) in the North Sea, overlay the results of our Brae Formation data similarly and shows a positive relation between grain size and permeability. While the narrow range of grain sizes in our data precludes establishment of a trend between grain size and permeability, our measurements compare well with the permeability and median grain diameter trend of hydrate free core sediments (plotted as triangles) (Konno et al., 2015). We also compare data from petrophysical analysis on tight gas sandstone analog rocks (Becker et al., 2017), which fall within the same range of grain size but are substantially less permeable due to high volumes of microporosity (up to 80%) in those rocks. Our results indicate that 3D grain size analysis and permeability simulation can be used as a reliable alternative to more classical and time consuming methods. As this technique continues to evolve, further work is required to assess the petrophysical properties of more sandstones with a greater range of grain shape and sizes.

4.2. Influence of Cement on Reservoir Properties

The Brae Formation, along with many other North Sea reservoirs, has quartz and calcite cements that are considered one of the main porosity reducing factors (Bjørlykke et al., 1992; Giles et al.,

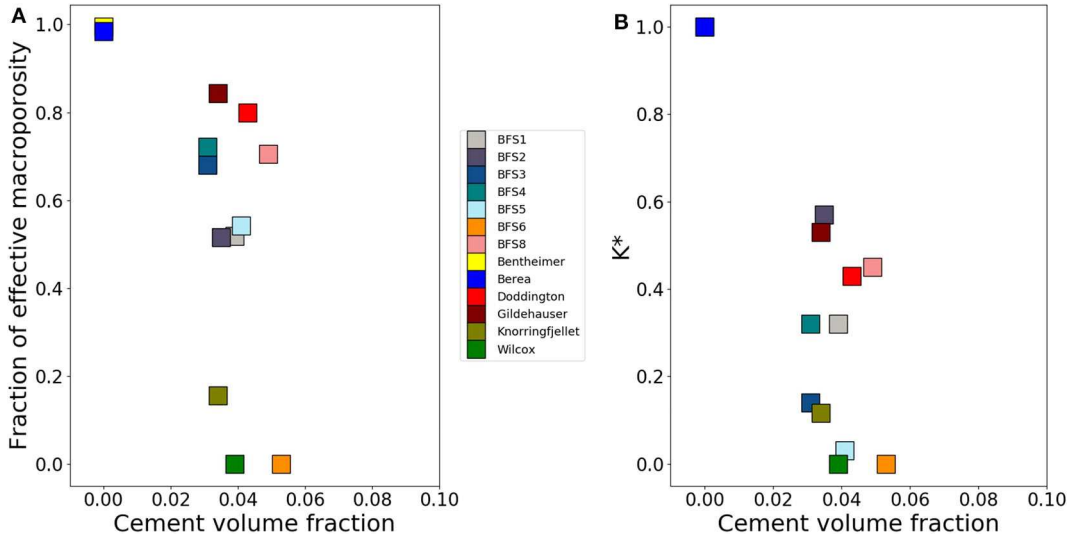

FIGURE 6 | Plots displaying the fraction of effective macroporosity **(A)** and the ratio of macro permeability and total permeability **(B)** as a function of cement volume fraction.

1992; Gluyas et al., 2000; Marcussen et al., 2010), with quartz overgrowth ranging from 3 to 15%, while calcite ranges from 20 to 40%, in concretion centers (Lu et al., 2011). Concretions exist as volumes of sandstone where almost all pore space is infilled between sand grains (e.g., sample BFS7), and these can exist in bed units ranging from 2 to 11 m thickness. Concretions are believed to be the consequence of the earliest diagenesis following deposition (Marchand et al., 2000). In the samples, we observe microquartz cement and fibrous over-growths, associated with a later phase of diagenesis and the presence of clay minerals (see Thomson et al., 2020 for SEM images). We observe the presence and quantify the relative proportion of these microporous phases using our X-ray CT images in this study, however the challenge remains to accurately model the influence of microporosity on reservoir properties (e.g., Mehmani and Prodanović, 2014; Bultreys et al., 2016b; Soulaine et al., 2016; Mehmani et al., 2019). In this work, we find agreement with previous studies of the Brae Formation, that the samples contain microporous cements, and their abundance falls within similar proportions as those reported by Lu et al. (2011), Marchand et al. (2000), and Thomson et al. (2020). The proportions of microporosity reported from image analysis in this study (**Table 1**) are slightly lower than those reported by Thomson et al. (2020) from Helium porosimetry measurements on the same samples.

The relationship between the volume of cement and the fraction of effective (connected) macroporosity shows an interesting trend in our data. We plot the cement volume fraction along the x-axis and the fraction of effective macroporosity along the y-axis. As **Figure 6A** shows, the proportion of effective macroporosity is increased with low volumes of the cement phase. As the cement phase increases, at volumes between 3 and 5%, the effective macroporosity decreases to around 50 to 80% efficiency. The majority of our data from the Brae Formation fall in this range, indicated by a cluster in the plot. As the cement volume fraction exceeds a volume of approximately 5.5% the connectivity of the pore network is lost with an effective macroporosity value of zero.

In **Figure 6B**, we display the ratio of $k^* = k_M/k_T$ as function of cement volume fraction, where k_M is macro permeability and k_T is total permeability. From this plot it is possible to observe the direct effect of cementation on fluid flow. Our two end-member models allow us to assess the pore space before (total porosity) and after (macroporosity) cementation. Similarly to the effects of cementation on pore network connectivity, we observe a trend that shows as the cement volume increases, the permeability declines quickly, finally becoming zero when cement volume fractions reach approximately 5.5%. The ratio of k^* in the samples ranges between 3 and 57%. Despite having one of the largest volumes of cement, sample BFS2 has the highest ratio of k^*. Sample BFS8 has the highest proportion of the cement phase and yet still shows good ability to permit fluid flow with a ratio of 45%. The lowest k^* ratio is found in sample BFS5 with a cement volume fraction of 5.1%, the third greatest in the samples.

The injection of CO_2 into deep saline aquifers has been practiced in the oil and gas industry for many years as a means of improving the efficiency of oil recovery from the reservoir. In more recent years, the storage of CO_2 in depleted reservoirs is being considered a possible long term method to reduce emissions to the atmosphere (Chadwick et al., 2004; Haszeldine et al., 2005; Holloway et al., 2006). One of the most notable projects includes the injection of CO_2 into the Utsira Formation of the Sleipner field (Furre et al., 2017). The Brae formation sandstone reservoir rocks of the Miller field have also been listed as a potential CO_2 storage target in the past due to a widespread seal rock and apparent natural system capable of storing accumulations of CO_2 for many millions of years (Lu et al., 2009). Three key processes of CO_2 trapping have been established (Hitchon, 1996): structural trapping, dissolution trapping, and mineral trapping. The potential of mineral trapping is greatest, due to residence times on the order of geologic timescales (Bachu

et al., 1994). As discussed previously, one might expect with the injection of CO_2, the reaction and precipitation of minerals during porous flow, and the eventual cementation of pore space, the connectivity and ability of the reservoir becomes diminished. These processes are indeed welcome, as more CO_2 is sequestered in the mineral form and the overall quality of the reservoir decreases, there is an increasing likelihood that the CO_2 remains trapped deep in the subsurface.

5. CONCLUSIONS

- We analyzed 8 samples from the Brae Formation, originating from the Miller oil field in the North Sea. We performed micro-structural analysis using 3D models obtained through X-ray CT images.
- We consider the grain size characteristics, porosity and permeability of the samples and assessed the relationships between those properties.
- Our grain size analysis indicates the samples are medium grained (250 μm to 500 μm length), moderately well-sorted and have a near symmetrical to fine skewed graphic distribution.
- No strict trend is observed between average grain size and both porosity and permeability in our data. However, grain size and permeability results do agree well with those from previous studies of other subsurface reservoir rocks.
- Within the samples analyzed in this study, an increase in cement volume has a negative influence on the porosity and permeability. Above a threshold cement volume of approximately 5.5% the connectivity of the pore network is disabled and porous flow is non-existent.

DATA AVAILABILITY STATEMENT

The datasets generated for this study are available on request to the corresponding author. Grain Size Data is available through figshare (Thomson et al., 2019).

AUTHOR CONTRIBUTIONS

P-RT carried out the image processing, grain separation and permeability simulations in all samples. RE carried out the preliminary grain size analysis. SH-M and P-RT jointly carried out the final grain size modeling and statistical analysis. All authors contributed to writing and revision of the manuscript.

ACKNOWLEDGMENTS

P-RT acknowledges support from the NERC Oil and Gas CDT graduate fellowship (grant number NE/M00578X/1). This research was also supported by the grant EAR125880 from the US National Science Foundation.

REFERENCES

Aase, N. E., and Walderhaug, O. (2005). The effect of hydrocarbons on quartz cementation: diagenesis in the upper Jurassic sandstones of the miller field, north sea, revisited. *Petrol. Geosci.* 11, 215–223. doi: 10.1144/1354-079304-648

Bachu, S., Gunter, W., and Perkins, E. (1994). Aquifer disposal of CO_2: hydrodynamic and mineral trapping. *Energy Convers. Manag.* 35, 269–279. doi: 10.1016/0196-8904(94)90060-4

Beard, D., and Weyl, P. (1973). Influence of texture on porosity and permeability of unconsolidated sand. *AAPG Bull.* 57, 349–369. doi: 10.1306/819A4272-16C5-11D7-8645000102C1865D

Becker, I., Wüstefeld, P., Koehrer, B., Felder, M., and Hilgers, C. (2017). Porosity and permeability variations in a tight gas sandstone reservoir analogue, Westphalian D, Lower Saxony basin, NW Germany: influence of depositional setting and diagenesis. *J. Petrol. Geol.* 40, 363–389. doi: 10.1111/jpg.12685

Bjørlykke, K., Nedkvitne, T., Ramm, M., and Saigal, G. C. (1992). Diagenetic processes in the brent group (middle Jurassic) reservoirs of the north sea: an overview. *Geol. Soc. Lond. Spcl Publ.* 61, 263–287. doi: 10.1144/GSL.SP.1992.061.01.15

Browne, G. H., King, P. R., Higgs, K. E., and Slatt, R. M. (2005). Grain-size characteristics for distinguishing basin floor fan and slope fan depositional settings: outcrop and subsurface examples from the late miocene mount messenger formation, new zealand. *N. Zeal. J. Geol. Geophys.* 48, 213–227. doi: 10.1080/00288306.2005.9515111

Buades, A., Coll, B., and Morel, J.-M. (2008). Nonlocal image and movie denoising. *Int. J. Comput. Vis.* 76, 123–139. doi: 10.1007/s11263-007-0052-1

Buades, A., Coll, B., and Morel, J. M. (2010). Image denoising methods. a new nonlocal principle. *SIAM Rev.* 52, 113–147. doi: 10.1137/090773908

Bultreys, T., De Boever, W., and Cnudde, V. (2016a). Imaging and image-based fluid transport modeling at the pore scale in geological materials: a practical introduction to the current state-of-the-art. *Earth Sci. Rev.* 155, 93–128. doi: 10.1016/j.earscirev.2016.02.001

Bultreys, T., Stappen, J. V., Kock, T. D., Boever, W. D., Boone, M. A., Hoorebeke, L. V., et al. (2016b). Investigating the relative permeability behavior of microporosity-rich carbonates and tight sandstones with multiscale pore network models. *J. Geophys. Res. Solid Earth* 121, 7929–7945. doi: 10.1002/2016JB013328

Chadwick, R., Zweigel, P., Gregersen, U., Kirby, G., Holloway, S., and Johannessen, P. (2004). Geological reservoir characterization of a CO_2 storage site: The Utsira sand, Sleipner, northern north sea. *Energy* 29, 1371–1381. doi: 10.1016/j.energy.2004.03.071

Folk, R. L. (1980). *Petrology of Sedimentary Rocks.* Austin, TX: Hemphill Publishing Company. Available online at: https://books.google.co.uk/books?id=e-cKAQAAIAAJ

Furre, A.-K., Eiken, O., Alnes, H., Vevatne, J. N., and Kiær, A. F. (2017). 20 years of monitoring CO_2-injection at sleipner. *Energy Proc.* 114, 3916–3926. doi: 10.1016/j.egypro.2017.03.1523

Garland, C. (1993). "Miller field: reservoir stratigraphy and its impact on development, in *Geological Society, Petroleum Geology Conference Series*, Vol. 4 (London: Geological Society of London), 401–414. doi: 10.1144/0040401

Giles, M., Stevenson, S., Martin, S., Cannon, S., Hamilton, P., Marshall, J., et al. (1992). The reservoir properties and diagenesis of the brent group: a regional perspective. *Geol. Soc. Lond. Spcl. Publ.* 61, 289–327. doi: 10.1144/GSL.SP.1992.061.01.16

Gluyas, J., Garland, C., Oxtoby, N., Hogg, A., Worden, R., and Morad, S. (2000). Quartz cement: the miller's tale. *Spcl. Publ. Int. Assoc. Sedimentol.* 29, 199–218. doi: 10.1002/9781444304237.ch14

Haszeldine, R., Quinn, O., England, G., Wilkinson, M., Shipton, Z., Evans, J. P., et al. (2005). Natural geochemical analogues for carbon dioxide storage in deep geological porous reservoirs, a United Kingdom perspective. *Oil Gas Sci. Technol.* 60, 33–49. doi: 10.2516/ogst:2005004

Hitchon, B. (1996). *Aquifer Disposal of Carbon Dioxide: Hydrodynamic and Mineral Trapping - Proof of Concept.* Devon, AB: Geoscience Publishing Ltd.

Holloway, S., Vincent, C. J., Bentham, M. S., and Kirk, K. L. (2006). Top-down and bottom-up estimates of CO_2 storage capacity in the United Kingdom sector of the southern north sea basin. *Environ. Geosci.* 13, 71–84. doi: 10.1306/eg.11080505015

Iassonov, P., Gebrenegus, T., and Tuller, M. (2009). Segmentation of X-ray computed tomography images of porous materials: A crucial step for characterization and quantitative analysis of pore structures. *Water Resourc. Res.* 45:8087. doi: 10.1029/2009WR008087

Inman, D. L. (1952). Measures for describing the size distribution of sediments. *J. Sediment. Res.* 22, 125–145. doi: 10.1306/D42694DB-2B26-11D7-8648000102C1865D

Joseph, L. H., Rea, D. K., and Van der Pluijm, B. A. (1998). Use of grain size and magnetic fabric analyses to distinguish among depositional environments. *Paleoceanography* 13, 491–501. doi: 10.1029/98PA01939

Ketcham, R. A., and Carlson, W. D. (2001). Acquisition, optimization and interpretation of X-ray computed tomographic imagery: applications to the geosciences. *Comp. Geosci.* 27, 381–400. doi: 10.1016/S0098-3004(00)00116-3

Klovan, J. (1966). The use of factor analysis in determining depositional environments from grain-size distributions. *J. Sediment. Res.* 36, 115–125. doi: 10.1306/74D7141A-2B21-11D7-8648000102C1865D

Konno, Y., Yoneda, J., Egawa, K., Ito, T., Jin, Y., Kida, M., et al. (2015). Permeability of sediment cores from methane hydrate deposit in the eastern Nankai trough. *Mar. Petrol. Geol.* 66, 487–495. doi: 10.1016/j.marpetgeo.2015.02.020

Lu, J., Wilkinson, M., Haszeldine, R. S., and Boyce, A. J. (2011). Carbonate cements in Miller field of the UK North Sea: a natural analog for mineral trapping in CO_2 geological storage. *Environ. Earth Sci*, 62, 507–517. doi: 10.1007/s12665-010-0543-1

Lu, J., Wilkinson, M., Haszeldine, R. S., and Fallick, A. E. (2009). Long-term performance of a mudrock seal in natural CO_2 storage. *Geology* 37, 35–38. doi: 10.1130/G25412A.1

Maast, T. E., Jahren, J., and Bjørlykke, K. (2011). Diagenetic controls on reservoir quality in middle to upper Jurassic sandstones in the south Viking Graben, north Seadiagenetic controls on reservoir quality in the south Viking Graben sandstones. *AAPG Bull.* 95, 1883–1905. doi: 10.1306/03071110122

Maher, C. (1980). Piper oil field. *Am. Assoc. Petrol. Geol.* 30, 131–172.

Marchand, A., Haszeldine, R., Macaulay, C., Swennen, R., and Fallick, A. (2000). Quartz cementation inhibited by crestal oil charge: Miller deep water sandstone, UK north sea. *Clay Minerals* 35, 201–210. doi: 10.1180/000985500546585

Marcussen, Ø., Maast, T. E., Mondol, N. H., Jahren, J., and Bjørlykke, K. (2010). Changes in physical properties of a reservoir sandstone as a function of burial depth-the etive formation, northern north sea. *Mar. Petrol. Geol.* 27, 1725–1735. doi: 10.1016/j.marpetgeo.2009.11.007

Mavko, G., Mukerji, T., and Dvorkin, J. (2009). *The Rock Physics Handbook: Tools for Seismic Analysis of Porous Media, 2nd Edn.* Cambridge: Cambridge University Press. doi: 10.1017/CBO9780511626753

Mehmani, A., Milliken, K., and Prodanović, M. (2019). Predicting flow properties in diagenetically-altered media with multi-scale process-based modeling: a wilcox formation case study. *Mar. Petrol. Geol.* 100, 179–194. doi: 10.1016/j.marpetgeo.2018.09.001

Mehmani, A., and Prodanović, M. (2014). The effect of microporosity on transport properties in porous media. *Adv. Water Resour.* 63, 104–119. doi: 10.1016/j.advwatres.2013.10.009

Otsu, N. (1979). A threshold selection method from gray-level histograms. *IEEE Trans. Syst. Man Cybernet.* 9, 62–66. doi: 10.1109/TSMC.1979.4310076

Ridler, T., and Calvard, S. (1978). Picture thresholding using. *IEEE Trans. Syst. Man Cybernet.* 8, 630–632. doi: 10.1109/TSMC.1978.4310039

Rooksby, S. (1991). The miller field, blocks 16/7b, 16/8b, UK north sea. *Geol. Soc. Lond. Memoirs* 14, 159–164. doi: 10.1144/GSL.MEM.1991.014.01.20

Scherer, M. (1987a). Erratum to "parameters influencing porosity in sandstones: a model for sandstone porosity prediction. *AAPG Bull.* 71:1508. doi: 10.1306/94886ED9-1704-11D7-8645000102C1865D

Scherer, M. (1987b). Parameters influencing porosity in sandstones: a model for sandstone porosity prediction. *AAPG Bull.* 71, 485–491. doi: 10.1306/703C80FB-1707-11D7-8645000102C1865D

Schlüter, S., Sheppard, A., Brown, K., and Wildenschild, D. (2014). Image processing of multiphase images obtained via X-ray microtomography: a review. *Water Resourc. Res.* 50, 3615–3639. doi: 10.1002/2014WR015256

Soulaine, C., Gjetvaj, F., Garing, C., Roman, S., Russian, A., Gouze, P., et al. (2016). The impact of sub-resolution porosity of x-ray microtomography images on the permeability. *Transport in Porous Media* 113, 227–243. doi: 10.1007/s11242-016-0690-2

Thomson, P.-R., Aituar-zhakupova, A., and Hier-majumder, S. (2018). Image segmentation and analysis of pore network geometry in two natural sandstones. *Front. Earth Sci.* 6:58. doi: 10.3389/feart.2018.00058

Thomson, P.-R., Ellis, R., Chiarella, D., and Hier-Majumder, S. (2019). *Brae Formation Grain Size Data.* Royal Holloway; University of London [Dataset]. doi: 10.17637/rh.11312816.v1

Thomson, P.-R., Hazel, A., and Hier-Majumder, S. (2019). The influence of microporous cements on the pore network geometry of natural sedimentary rocks. *Front. Earth Sci.* 7:48. doi: 10.3389/feart.2019.00048

Thomson, P.-R., Jefferd, M., Clark, B., Chiarella, D., Mitchell, T., and Hier-Majumder, S. (2020). Pore network analysis of brae formation sandstone, North Sea. *Marine Petrol. Geol.*

Turner, C. C., and Allen, P. J. (1991). The central brae field, block 16/7a, UK north sea. *Geol. Soc. Lond. Memoirs* 14, 49–54. doi: 10.1144/GSL.MEM.1991.014.01.06

Visher, G. S. (1969). Grain size distributions and depositional processes. *J. Sed. Res.* 39, 1074–1106. doi: 10.1306/74D71D9D-2B21-11D7-8648000102C1865D

Wentworth, C. K. (1922). A scale of grade and class terms for clastic sediments. *J. Geol.* 30, 377–392. doi: 10.1086/622910

Wildenschild, D., and Sheppard, A. P. (2013). X-ray imaging and analysis techniques for quantifying pore-scale structure and processes in subsurface porous medium systems. *Adv. Water Resour.* 51, 217–246. doi: 10.1016/j.advwatres.2012.07.018

Wildenschild, D., Vaz, C., Rivers, M., Rikard, D., and Christensen, B. (2002). Using x-ray computed tomography in hydrology: systems, resolutions, and limitations. *J. Hydrol.* 267, 285–297. doi: 10.1016/S0022-1694(02)00157-9

Worden, R. (1998). Dolomite cement distribution in a sandstone from core and wireline data: the triassic fluvial chaunoy formation, Paris basin. *Geol. Soc. Lond. Spcl. Publ.* 136, 197–211. doi: 10.1144/GSL.SP.1998.136.01.17

Youssef, S., Rosenberg, E., Gland, N. F., Kenter, J. A., Skalinski, M., and Vizika, O. (2007). High resolution CT and pore-network models to assess petrophysical properties of homogeneous and heterogeneous carbonates. *Soc. Petrol. Eng.* doi: 10.2118/111427-MS

Conflict of Interest: The authors declare that the research was conducted in the absence of any commercial or financial relationships that could be construed as a potential conflict of interest.

Chapter 7

Discussion, Critical Evaluation and Future Work

7.1 Digital rock physics - critical evaluation of methodology

This section provides a critical evaluation of the different methods used in this work, and described in Chapter 2. These include sample selection, image filtering, segmentation techniques, and permeability simulation. In the following sections, each of these is discussed in terms of their advantages and disadvantages.

7.1.1 Sample selection

Although a number of different rock samples were used in this research, if this study was to be repeated or indeed improved upon, more samples would be required for further image analysis. In hindsight, with unrestricted access to the original cored wells of the Miller field, more samples from the Brae Formation sandstone should have been acquired. Though there were a total of 8 samples analyzed from this reservoir, one of these was almost completely consolidated and showed no visible porosity, and therefore was not suitable for pore network analysis. The acquisition and analysis of more samples would provide more reliable data, a better understanding of heterogeneity in this formation and hopefully some further insight into pore network connectivity variability in an analogous CCS reservoir.

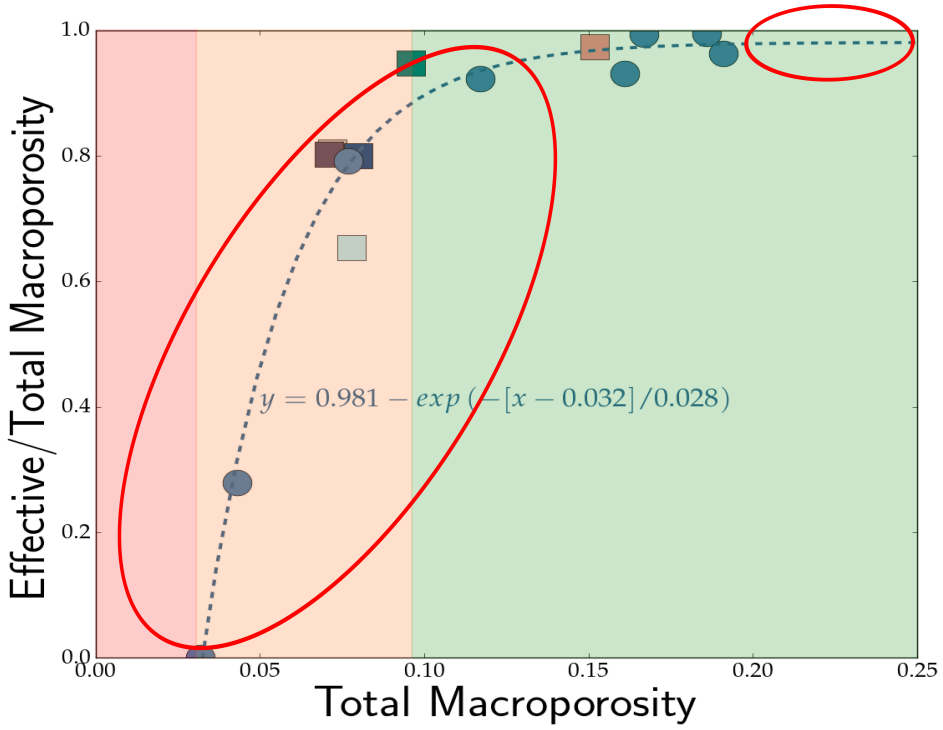

Figure 7.1: The ratio between effective and total macroporosity as a function of total macroporosity. Modified from Thomson et al. (2020), showing regions of the plot that require further analysis.

Figure 7.1 demonstrates the current lack of data in this study. Future work which includes the analysis of samples characterized by lower porosity ($< 10\%$) and higher porosity ($> 20\%$) will help consolidate the different pore connectivity regimes shown as isolated (red), partially effective (orange) and effective (green). In addition to this, the 3D pore network analysis using samples acquired at different image resolutions and scales, will allow the determination of an appropriate representative elementary volume (REV) for future studies.

7.1.1.1 Scaling

One major limitation of this work and pore scale analysis in general is its lack of ability to represent reservoir scale heterogeneity. The comparison between 5 mm rock samples and km scale sand bodies is almost an impossible task. While upscaling was not an objective of this work, it is important to discuss here. Reservoir scale

heterogeneity can simply not be incorporated at the pore scale, unless of course, you have a completely homogeneous reservoir, which is practically unheard of within nature. The quality of the reservoir can vary spatially, which means there may significant change in permeability, porosity, thickness, faulting, fracturing and rock facies. In order to try and incorporate this into a pore scale study such as this, one would have to acquire and process a large number of samples, from various intervals within the overall reservoir. This type of study would not come without its own difficulties, as acquiring samples and their images is both time consuming and expensive. An alternative approach is to consider a step by step method to include all scales. One potential method for upscaling is the integrated approach between data at different scale. Rhodes et al. (2008) and Blunt et al. (2013) have suggested the use of core-scale measurements to benchmark pore scale modelling. From here, the core-scale measurements are input into a metre scale simulation (grid block), upscaled and finally reservoir simulation of the macroscopic process of interest. However, this link between pore and reservoir scale processes remains a fundamental research challenge.

7.1.2 Image filtering

The image filtering process is an important step in any image analysis study. It forms the first step from which results can be affected if the images are not processed properly. As described in Chapter 2, section 2.2.2.1, the non-local means filter (Buades et al., 2005, 2008) was the primary filtering method used in this thesis. The main advantages of this filtering technique are consistent and reliable results which can be attributed to the algorithms consideration and average weighting of gray scale values of voxels in the local neighborhood to the voxel that is being processed at any one time. However, given the extra consideration for the voxels in the local neighborhood, this provides the first and major disadvantage of this filter. The process is computationally intensive and therefore can take up to several hours to run, particular in samples with a large volume of interest and high image resolution. While this issue can be countered by the ability to restrict the process to 2D, there is still room for improvement going forward. For future work, the application of 3D

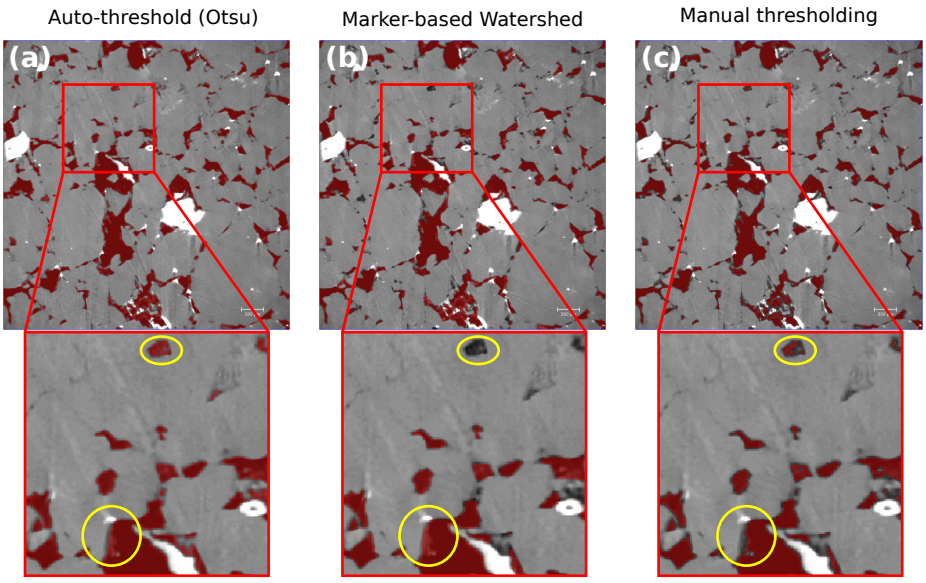

Figure 7.2: Comparison between three segmentation techniques trialled in this study. Auto-threshold (a), Marker-based Watershed (b), and Interactive (manual) threshold (c).

filtering is recommended, with the addition of access to increased computational resources.

7.1.3 Image segmentation

The image segmentation is another crucial step involved in any image analysis work and this has the ability to affect all subsequent quantitative analysis and modelling attempts (Iassonov et al., 2009). Chapter 2, section 2.2.2.2 of this thesis briefly describes the key image segmentation techniques and outlines the interactive threshold segmentation method that was consistently used in this research. Though this method is user-dependent and can introduce some operator bias, it remains a popular technique for image segmentation. Despite numerous automated image segmentation methods (Otsu, 1979; Ridler and Calvard, 1978), it is often still necessary to provide manual assistance during the segmentation process (Bultreys et al., 2016a; Iassonov et al., 2009). Automated and semi-automated segmentation methods including Otsu (Otsu, 1979) and the watershed algorithm respectively were trialled and tested in this research (Figure 7.2(a) and (b)). Both techniques were found to

have issues and there was a common theme, the overestimation and underestimation of the pore phase in many samples. As Figure 7.2 highlights, the different segmentation algorithms all produce slightly different results (indicated by the areas circled in yellow). The interactive (manual) thresholding technique (Figure 7.2(c)) was preferred in this research because it was more sensitive and permitted the segmentation of microporous material, which the automated techniques simply included as macropores.

The image acquisition process can also have a large influence over image processing. Chapter 3 demonstrates the impact of high energy synchrotron beam image acquisition and the additional image filtering and segmentation steps required to produce reliable 3D models for data analysis. While the images used in Chapter 3 required more attention, the other images in Chapters 4, 5 and 6 were considerably easier to process and as a result could be segmented reliably using the interactive threshold segmentation method alone. Although, as previously mentioned, there is a certain degree of uncertainty surrounding the manual segmentation of images, cautious steps were made during the process to ensure reliability of the final segmented images. During the initial stage of manual thresholding, the histogram range was selected based on the visual inspection of gray scale color. Throughout each sample, the individual slices were moved from top to bottom along the Z-axis to check that voxels assigned to the phase of interest are correctly selected and no erroneous material is included. In addition to this, the final segmented volumes of interest are measured and the results are cross referenced with measurements from other sources. This includes measurements made on the same samples from other digital rock physics studies and also measurements achieved from experimental techniques. Even if excellent data and reliable results are achieved from user controlled segmentation processes, the demand for reliable, consistent, computationally efficient and automated techniques is still apparent (Iassonov et al., 2009). Future algorithms that reduce or remove the influence of operator bias, while still producing high quality results in homogeneous and heterogeneous samples from different acquisition setups will play an important role going forward.

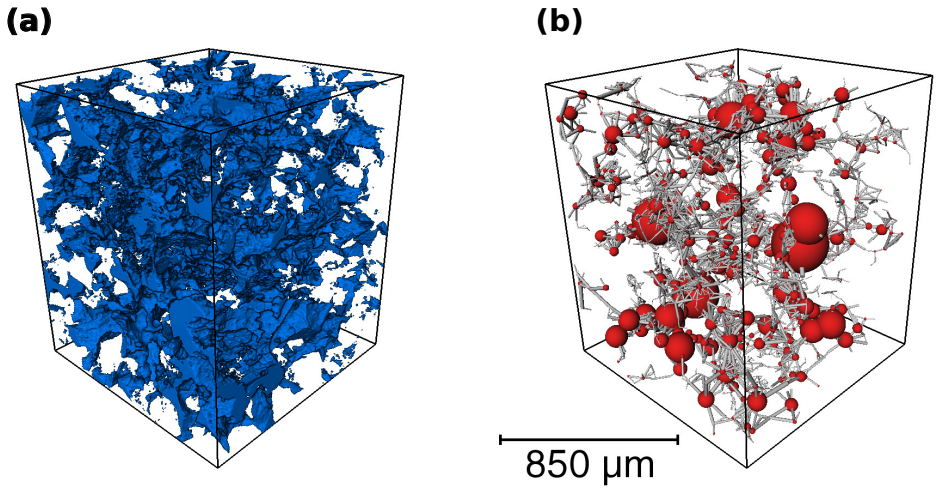

Figure 7.3: Volume rendering visualization of effective pore network (a) and pore network model simplified geometry of effective pore network (b).

7.1.4 Permeability simulation

The finite volume solver as described in Chapter 2, section 2.3.3 and in greater detail in Chapter 3, was used to obtain the single phase permeability measurements in this work. The main advantage of this solver is the ability to simulate flow directly though the 3D voxel volume which represents the natural geometry of the pore network (see Figure 7.3(a)). Though this type of solver is often a preferred approach because of its numerical efficiency and its ability to simulate fluid flow with very large density and viscosity ratios (Meakin and Tartakovsky, 2009), in this work, it was found to be computationally intensive. Indeed, simulations were running for up to three or four days in some samples. The computational time was perhaps the most limiting factor of the finite volume solver, however as was discussed in the previous sections, access to increased computational resources would reduce the time constraints of this method in future studies.

The other major disadvantage of the finite volume solver used in this work is its limited ability to simulate single-phase flow. Though the absolute permeability measurements obtained in this work have provided useful insights related to the influence of pore network connectivity and microporous cements, further work is required to assess the relationship between pore network connectivity and multi-

phase flow. The phenomenon of two-phase and three-phase flow in porous media is an active area of research and has direct implications related to the better understanding of fluid flow in subsurface reservoirs. The implementation of different numerical approaches (e.g. network models (Figure 7.3(b)) and Lattice Boltzmann (Blunt, 2001; Shah et al., 2016)) which utilize simplified pore geometries and are more computationally efficient will provide a more developed understanding in this research area and also a useful comparison to techniques used in this work.

7.2 Pore network connectivity

As described in Chapter 1, one aim of this thesis was to investigate the presence of an experimentally derived porosity threshold using digital techniques. 3D pore network models generated from X-ray microtomographic images have successfully demonstrated that there is an increase in pore radius, throat radius, throat length and coordination number with increased porosity. The models have also highlighted three distinct regimes of pore network connectivity: above 10% porosity the effective pore network has a near 1:1 ratio with the total pore network, between 3 and 10% porosity the connectivity of the pore network is reduced and it becomes partially effective, while below 3% porosity a threshold is established and the effective network is completely lost.

As the results indicate in Chapter 3, the pore geometry varies quite significantly in the sandstone rocks of different porosity. With a low porosity of 4%, the Fontainebleau sandstone is characterized by fewer, larger pores and throats. While the Berea sandstone has a porosity of 16% and displays a dense network of much smaller and more numerous pores and throats. These observations are supported by the measurements of median coordination number in each of the samples. As the porosity increases, the pore network becomes better connected, displaying median coordination number of 2 and 6 for Fontainebleau and Berea sandstone, respectively. These results build on existing evidence of an increase in median coordination number with porosity as demonstrated by Lindquist et al. (2000). Although their work focused on the Fontainebleau sandstone with a range of porosity (7 -

22%) and using slightly different image resolution, segmentation and skeletonization algorithms, the results in this thesis are largely similar.

Another significant outcome of the data presented in Chapter 3 is the relationship between total porosity and isolated porosity. The Fontainebleau sandstone, characterized by its lower porosity and less well connected pore network, has 21% of its pore space in isolation. While in comparison, the Berea sandstone has a higher porosity and much denser network of pores and throats, and consequently has a lower proportion of isolated pore space between 2 and 6%. This finding supports previous observations of increased pore connectivity at higher porosity in theoretical models of pore networks using fluid mechanical and geometrical models (von Bargen and Waff, 1986; Wimert and Hier-Majumder, 2012; Ghanbarzadeh et al., 2015).

Although Chapter 3 formed an important step in establishing the methodology and the results provided insight into the variation of pore network connectivity in two sandstones with quite different porosity, the data analysis was limited by a small number of samples. In Chapter 4 the analysis develops with the addition of new samples, including three carbonates and three sandstones. Similarly to the findings from Chapter 3, rocks with higher porosity are characterized by a pore network of larger pore and throats, and an increase in median coordination number with increasing porosity. While previous research has focused on one particular rock type (Lindquist et al., 2000), these results build on earlier work by Thomson et al. (2018), and demonstrate the variability in pore network geometry in both homogeneous and heterogeneous rock types.

In Chapter 5 it was discussed how three regimes of pore network connectivity are identified from the 3D pore models. Figure 7(a) in this chapter highlights that above 10% porosity, the connectivity of the total and effective pore network is nearly 1:1. The connectivity of the pore network becomes partially effective between 3 and 10% porosity. In this window between 3 and 10%, the ratio of effective and total macroporosity increases rapidly before leveling off at approximately 10% porosity (Figure 7(b)). Finally, below 3% porosity, a threshold is identified and

pores become completely disconnected, inhibiting porous flow. While numerous experimental studies have demonstrated that a minimum threshold porosity must exist before flow is permitted through a network of effective pore space (Gomez et al., 2010; Mavko and Nur, 1997; Revil et al., 2014), this is one of the first studies that has been able to identify a similar porosity threshold using 3D pore models derived from X-ray micro CT images of natural reservoir rocks. Furthermore, the 3% threshold identified from the 3D models is in good agreement with previous estimates of porosity threshold of 2-2.5% (Gomez et al., 2010; Mavko and Nur, 1997; Revil et al., 2014).

7.2.1 Implications of pore network connectivity

Using 3D models derived from the reconstruction of X-ray CT images, the results in this thesis show that it is possible to identify a so called percolation or porosity threshold in samples of natural rock. These findings match closely with percolation threshold results from previous empirical studies and provide an alternative method for accurate pore characterization and porosity/permeability relationships.

The pore connectivity of natural rocks has important implications for many large scale industries, e.g. hydrology, petroleum engineering and CCS. The findings of this research indicate that it is important to have an understanding of reservoir quality for reliable prediction of reservoir performance during projects that rely on the rocks ability to store fluids and allow effective flow. One such example is CCS, which although is not a new technology (Chadwick et al., 2004; Haszeldine et al., 2005; Holloway et al., 2006; Furre et al., 2017), is likely to become more prominent in the near future as a long term means of storing CO_2 in subsurface reservoirs. In fact, many former petroleum reservoirs, including the Brae Formation sandstone of the Miller field (Lu et al., 2009), have been targeted as potential sites for CCS. The three regimes of pore connectivity discussed in this thesis have significant considerations for CCS reservoirs. While intervals of reservoir with poor quality ($< 3\%$ porosity) will act as baffles to the flow of fluids in some parts, they may also act as effective sealing rocks in others, particularly nearer the top of the reservoir. Other intervals, with porosity between 3–10% will have increased connectivity and can be

predicted to perform slightly better, however may still act as baffles to flow. Higher quality reservoir zones ($> 10\%$ porosity) should be targeted for their improved ratio of effective pore space and greater potential for efficient storage.

While it is important to have good quality reservoir that allows the flow and storage of fluids, in the case of CCS it is also crucial that an effective seal rock is in place so that injected CO_2 remains trapped. Although this thesis focused on the pore connectivity in reservoir rocks, there is scope for the characterization of pore networks in shales and other fine grained rocks using similar digital techniques (e.g. FIB-SEM). Future studies which incorporate these techniques have the ability to quantify and assess the pore network variation and the rocks value as a good or bad sealing lithology.

7.3 The influence of microporosity

The second aim of this thesis was to explore the limit of permeability reduction by the presence of microporous material that occupies pore space with pore and throat dimensions that are characteristically much smaller and are often hosted in secondary mineral phases. As this study has shown, using simplified models of the upper and lower bounds of microporosity, the effective permeability of rocks decreases in a nonlinear fashion with increasing microporous cement until a threshold cement volume fraction occurs at $\sim 5\%$ in the lower bound.

The key challenge with digital rock physics - X-ray microtomography analysis of porous media is the inability to accurately represent microporosity in porosity and permeability measurements. The primary limitation is the image resolution, where micropores, typically below 2 μm, can not be accurately identified using traditional micro CT techniques (see for example, Chapter 4, Figure 1, where macropores are shown in red, and what are interpreted as micropores–regions of intermediate gray scale, are shown in blue). Other imaging methods, for example Focused Ion Beam-Scanning Electron Microscope (FIB-SEM) do exist, and permit the identification of micropores, however, are further limited by their destructive nature and small region of interest. The general rule of imaging microstructure dictates that the higher the

resolution required, the smaller the sample size is. Despite this limitation, some promising results have been published with the inclusion of microporosity in dual-scale models using micro CT (Mehmani et al., 2019; Mehmani and Prodanović, 2014; Bultreys et al., 2016b; Soulaine et al., 2016).

An alternative approach to account for microporous material using micro CT images, like in this thesis, is to investigate the upper and lower limits of the microporous material on permeability. Due to the fact that the micropores are beyond the detection limit of the scanner, their material phase was assigned different properties during the image segmentation stage. In the upper bound model, the regions of microporous material are treated as completely permeable, that is 100% void space. On the other hand, for the lower bound model, the microporous material is considered impermeable, preventing flow and therefore assuming flow through macropores only. While these models did not directly quantify the influence of microporosity, they provide a margin of error for permeability prediction using digital approaches. In reality, the true permeability probably lies somewhere in between the two.

As the results in Chapter 4 indicate, the connectivity of the pore network is dramatically reduced with increasing volume fraction of microporous cement. This is particularly evident in Figure 9(A) and 9(B), where the plots show the fraction of interconnected macroporosity as a function of cement volume fraction and the ratio between macro permeability and total permeability as a function of cement volume, respectively. These data suggest that there is a threshold cement volume fraction of 4%, beyond which the pore network becomes blocked and porous flow is no longer possible. While this was the case for the samples in this study, the results presented in Chapter 6 display a threshold cement volume fraction closer to 5%. The reason for this dissimilarity can be attributed to the different rock types. The samples analyzed in Chapter 4 include the Knorringfjellet and Wilcox sandstones which are considerably more heterogeneous than the Brae Formation sandstones as analyzed in Chapter 6, despite the fact that the Brae Formation is known to contain considerable amounts of porosity reducing quartz and calcite cement (Bjørlykke et al., 1992;

Giles et al., 1992; Gluyas et al., 2000; Marcussen et al., 2010). Nevertheless, the results from both analyses indicate that the effective permeability of microporous rocks decrease with increasing cement volume fraction in a nonlinear fashion.

7.3.1 Implications of modelling microporous material

While the models in this work only represent two rather simplistic end member cases, they highlight the importance of digital techniques in quantifying microporous pore clogging material. As the results demonstrate, the increasing volumes of microporous material have a detrimental effect on the rocks ability to permit fluid flow. While this thesis focused on the impact of microporous material at the pore scale, the findings suggest important considerations for larger scale processes. Applying this to the bigger picture, again considering CCS as an example, as CO_2 is injected and reactive flow leads to the precipitation of secondary cement-forming material, this can affect the porosity and permeability, and ultimately reduce the reservoir quality. Based on the models used in this work, during initial stages of CO_2 injection while the pore network remains relatively clean (before cementation), the flow regime will be more effective. As CO_2 is continually injected and moves through the interconnected pore space in the reservoir, the precipitation of secondary minerals becomes more likely. As a consequence of precipitate cementation the pore flow regime becomes less effective and CO_2 is preferentially immobilized. This is especially the case when the rock and fluid properties are in favour, namely formation water composition, lithological heterogeneity and mineralogy.

The Brae Formation sandstone has been identified as a potential sink for the storage of CO_2. Possessing a widespread seal rock, considered the most efficient means of engineered CO_2 storage, the Miller field complex (which incorporates the Brae Formation sandstone) has a natural system capable of storing CO_2 for many millions of years (Lu et al., 2009, 2011). In addition to this the Brae Formation sandstone contains an abundance of calcite concretions which would enhance the process of CO_2 mineral trapping. Although the process is slow, occurring over long time scales (to the order of many millions of years), mineral trapping is one the most efficient methods for long term storage of CO_2 (Bachu et al., 1994). Considering

the Miller field complex has both an effective seal rock and mineralogy that is preferential for mineral trapping and long term immobilization of CO_2, it is unfortunate that appropriate infrastructure has been removed and therefore is now unlikely to become a CCS site without significant reinvestment. While this is the case for the Miller field, there are plenty of analogous North Sea reservoirs which have infrastructure in place and would benefit from the digital pore characterization techniques as presented in this research. As the results within this thesis demonstrate, digital methods have the ability to provide a better understanding of microporous material and their influence on pore network connectivity in subsurface reservoirs.

Chapter 8

Conclusions

Before summarizing the main findings of this thesis, it is important to recall the key aims:

1. Through reconstruction of 2D X-ray microtomographic images, can 3D models help provide a better understanding of pore network connectivity in natural rocks with varying porosity?

2. Using 3D pore network models is it possible to identify a porosity/percolation threshold across a range of different rock samples?

3. What is the influence of sub-resolution microporosity on pore network connectivity and its ability to permit flow?

Considering these aims, the main conclusions are summarized below:

- Pore connectivity is dependent upon porosity. Higher porosity rocks are characterized by a denser network of larger pores and throats. As a result of this, the network of pore space is better connected, as indicated by median coordination number that increases with porosity.

- Total porosity influences the effective and isolated porosity. Higher porosity rocks have a larger proportion of effective pores and throats, and a smaller proportion of isolated pore space. As porosity reduces, the effective network becomes smaller and a higher proportion of isolated pore space is observed.

- Three distinct regimes of pore network connectivity are identified. The fully effective regime is apparent above 10% porosity. The pore space is almost completely in communication and displays a similar proportion of total and effective porosity, with a near 1:1 ratio. From 10 to 3% porosity the ratio of effective and total porosity decreases sharply, forming a partially effective zone. Below 3% porosity the pore network is no longer in communication, an isolated pore network regime is apparent and a porosity threshold is established.

- Microporous material that occupies pore space below the detection limit of the scanner has a negative impact on pore connectivity and permeability in the samples analyzed.

- The lower bound models indicate that at low proportions of microporous cement volume, the fraction of effective porosity is high. As cement volume fraction increases, to volumes between 3 and 5%, the fraction of effective porosity decreases to between 50 and 80% efficiency. With cement volume fractions exceeding approximately 5.5%, the effective porosity is lost and the pore network becomes isolated.

- The ratio of macro permeability and total permeability shows a similar trend with cement volume fraction. As the proportion of cement volume increases, the effective permeability decreases in a nonlinear fashion until a cement volume threshold is reached and porous flow is discontinued.

It is apparent from the results presented in this thesis that the connectivity of pore network systems are ultimately controlled by porosity. The use of 3D models generated from X-ray microtomographic images provide a powerful tool for the analysis of pore geometries in different reservoir rocks (limestones and sandstones). This technique has the ability to play an important role in reservoir characterization and has the added advantages of being less time consuming and flexible for the petrophysical analysis of natural rocks compared to experimental techniques which assess the same properties. While there is still some work to be

done to bridge the gap between pore scale and reservoir scale, digital methods are a powerful tool which aid our understanding of the fundamental physical processes that control the transport and mechanical properties of rocks at the micro scale.

Although the three key aims were addressed in this thesis, there are still some unknown factors related to our understanding of pore connectivity and fluid flow in natural rocks. Future work of interest is outlined below:

- How the connectivity of pore networks varies as result of reactive flow. This type of study would be well suited to carbon capture and storage and could shed some light on the influence of CO_2 injection into the reservoir. A digital analysis study would be interesting to compare the pore network system before and after CO_2 injection.

- A better understanding of the role of microporosity during fluid flow in various rock types. Incorporating the 3D analysis of micro and macroporosity using different imaging techniques, for example, FIB-SEM and standard micro CT techniques.

- The connectivity of pore networks in shales and other fine grained rocks using FIB-SEM. Characterizing the pore system in these rocks would not only build on the results presented in this thesis by analyzing rocks of low porosity but it would also help provide a better understanding of fine grained rocks which have an important role to play as seal rocks in conventional oil & gas systems and during CCS projects.

Appendix A

Supplementary material for the manuscript: Pore Network Analysis of Brae Formation Sandstone, North Sea (Chapter 5)

Supplementary Material: Pore Network Analysis of Brae Formation Sandstone, North Sea (Chapter 5)

Paul-Ross Thomson[a,], Mark Jefferd[b], Brett L Clark[c], Domenico Chiarella[a], Tom Mitchell[b], Saswata Hier-Majumder[a]

[a]*Department of Earth Sciences, Royal Holloway University of London, Egham, Surrey, TW20 0EX, UK.*
[b]*University College, London*
[c]*Natural History Museum, London*

Abstract

This document contains supplementary figures and tables accompanying the main manuscript.

Keywords: Digital Rock Physics, Porosity, Permeability, Pore Network Model, Reservoir, X-ray micro-CT, Brae Formation, Miller Field

1. Helium porosity

Helium porosimetry was utilized to provide a comparison between porosity measurements generated using DRP to more traditional experimental methods. To perform these measurements, a Micrometrics® AccuPyc 1340 constant volume pycnometer, fed with helium gas was used. Helium gas was chosen due to its chemical inertness and for its small atomic size allowing for easier penetration into the sample.

The working principles behind the pycnometer correspond to the ideal gas law, and the relationship between pressure and volume. Initially a sample is

Email address: Paul-Ross.Thomson.2016@live.rhul.ac.uk (Paul-Ross Thomson)

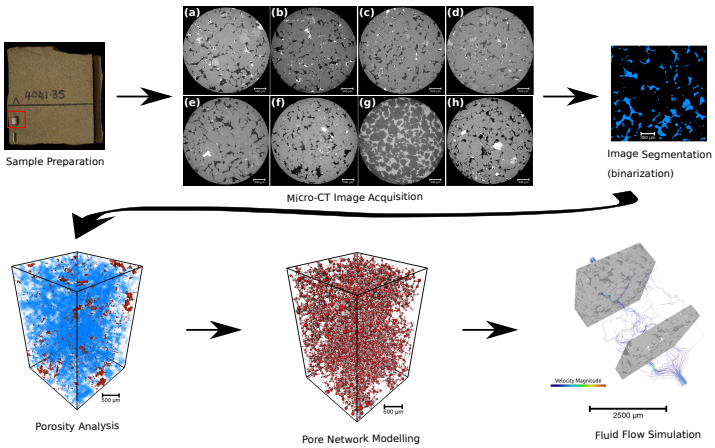

Figure 1: Work flow followed in this study for each sample, including sample preparation, micro-CT image acquisition, image segmentation, porosity analysis, pore network modelling and fluid flow simulation.

placed within a chamber of known volume and pressurised with helium gas. A valve is then opened connecting this chamber to another chamber of known volume, and the corresponding pressure drop used to calculate the volume of the solid material in the first chamber. The volume of material measured in this chamber includes the solid rock matrix plus any inaccessible pore space. The connected pore volume is then calculated by subtracting this volume from the bulk volume of the sample.

The samples used in the pycnometer were cylindrical core plugs subsampled from the same initial cores from which the DRP samples were taken. To help assess sample heterogeneity, cores of both 10 mm and 20 mm diameter were produced. The bulk volume of each sample was obtained by measuring the length and diameter of the sample using electronic callipers precise to 0.01 mm. Due to the slight friable nature of the sandstone used,

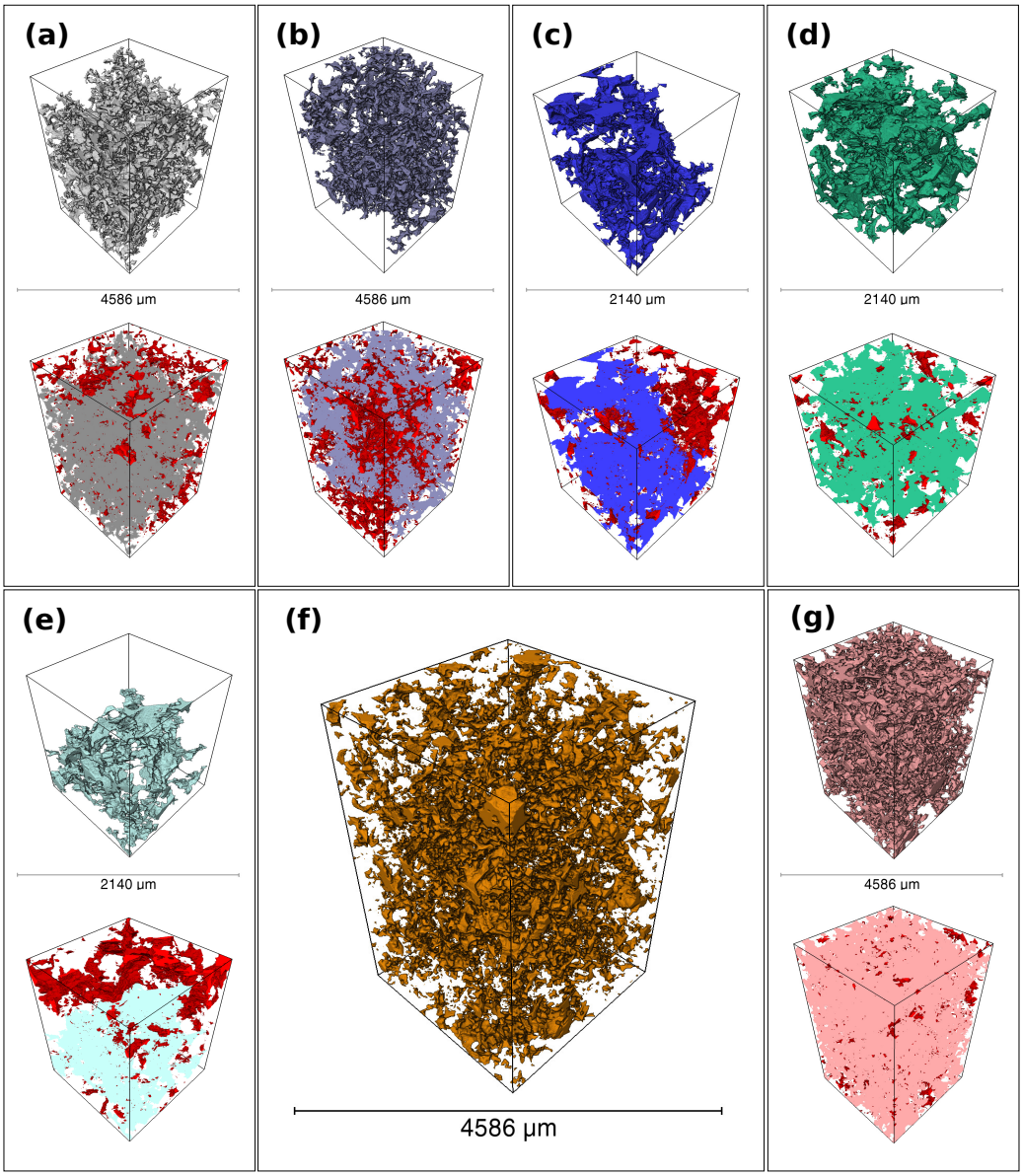

Figure 2: Visual representation of effective porosity vs isolated porosity. Samples shown include BFS1 (a), BFS2 (b), BFS3 (c), BFS4 (d), BFS5 (e), BFS6 (f) and BFS8 (g). The top row displays the proportion of effective porosity, whilst the bottom row shows both effective and isolate pores in each volume.

the samples would not quite be true cylinders, with the length and diameter varying by a maximum of 0.1 mm depending where on the sample the measurements were taken. Nevertheless, when calculating the bulk volume of each sample it was assumed they were true cylinders, with the length and diameter value used being an average obtained from at least 3 measurements on each sample. With a generous error of ±0.05 mm being applied to the length and diameter measurement, it is assumed that the maximum error in our bulk volume calculation is ±0.051 cm^3 (0.9%) and ±0.012 cm^3 (1.8%) for the 20 mm and 10mm diameter samples respectively.

To assess the accuracy of the pycnometer, a calibration test was performed prior to each suite of measurements. This involves measuring the volume of a stainless-steel ball; provided by the manufactures, which is of a known volume. The apparatus is recalibrated until the pycnometer is measuring to an accuracy of ±0.0105 cm^3 for the chamber used by the 20 mm diameter samples and ±0.005 cm^3 for the chamber used by the 10 mm diameter samples. This machine error alone propagates to porosity errors of approximately ±0.15% and ±0.6% for the 20 mm and 10 mm diameter samples respectively. Combining the machine error of the pycnometer with the error in measuring the length and diameter of the samples, we find that the maximum absolute error in our helium porosity measurements are ±0.8% for the 20 mm samples and ±1.8 % for the 10 mm diameter samples.

Sample	**Voxel Size (μm)**	**ROI (voxels)**	**Total Porosity**	**Effective Porosity**
BFS1	3.9448	600×600×900	7.2	5.8
		300×300×450	6.8	5.3

Sample	Voxel Size (μm)	ROI (voxels)	Total Porosity	Effective Porosity
		300×300×450	7.0	0
		600×600×900	5.7	4.2
		300×300×450	5.5	3.8
		300×300×450	5.7	0
BFS2	3.9448	600×600×900	7.1	5.7
		300×300×450	9.4	9.0
		300×300×450	6.2	2.4
		600×600×900	7.6	6.2
		300×300×450	6.9	5.0
		300×300×450	8.5	7.7
BFS3	1.9727	1200×1200×1800	8.6	7.8
		600×600×900	6.9	0
		600×600×900	9.9	9.5
		1200×1200×1800	8.1	7.3
		600×600×900	6.5	0
		600×600×900	9.4	9.0
		600×600×700	8.0	6.4
		600×600×350	7.9	5.9
		600×600×350	8.1	7.3
BFS4	1.9727	1200×1200×1800	7.3	0
		600×600×900	6.5	0
		600×600×900	7.5	0
		1200×1200×1800	10	9.5

Sample	Voxel Size (μm)	ROI (voxels)	Total Porosity	Effective Porosity
		600×600×900	9.1	0
		600×600×900	10.6	10
		600×600×700	9.6	9.1
		600×600×350	9.1	7.7
		600×600×350	10.1	9.7
BFS5	1.9727	1200×1200×1800	10.7	10.3
		600×600×900	10.5	10.2
		600×600×900	10.4	9.9
		1200×1200×1800	9.1	8.5
		600×600×900	9.0	7.7
		600×600×900	8.9	7.9
		600×600×700	7.8	5.1
		600×600×350	7.6	7.0
		600×600×350	8.1	7.2
BFS6	3.9448	600×600×900	5.0	0
		300×300×450	5.3	0
		300×300×450	4.7	0
		600×600×900	6.1	0
		300×300×450	6.3	0
		300×300×450	5.8	0
BFS7	Zero visible porosity			
BFS8	3.9448	600×600×900	15.2	14.8

Sample	**Voxel Size** (μ**m**)	**ROI** **(voxels)**	**Total** **Porosity**	**Effective** **Porosity**
		300×300×450	13.9	13.5
		300×300×450	13.1	12.1
		600×600×900	11.9	11.3
		300×300×450	10.9	10.3
		300×300×450	10.2	9.1

Table 2: Porosity calculation for two different segmentation methods (dark gray automated thresholding and light gray interactive manual thresholding) and different sizes of ROIs from which the porosity was calculated.

Table 1: Pore network model analysis results. Showing mean values of coordination number (CN), and median values for pore radius and throat radius and throat length for total porosity and effective porosity (bold font). Effective porosity volumes were computed using the same dimensions as those used in absolute permeability simulation.

Sample	ϕ**(%)**	**CN**	**Pore radius (μm)**	**Throat radius (μm)**	**Throat length (μm)**	**k mD**
BFS1	7.2	1.4	9.3	10.8	73.6	-
	5.8	**3.1**	**26.7**	**13.6**	**84.0**	**91.2**
BFS2	7.1	1.4	9.6	10.5	73.4	-
	5.7	**3.1**	**26.4**	**13.2**	**84.1**	**86.3**
BFS3	8.6 (7.8)	2.0	6.1	7.2	40.7	-
	8.0 **(6.4)**	**3.9**	**13.5**	**7.9**	**42.3**	**7.6**
BFS4	7.3 (0)	1.8	5.5	6.4	36.3	-
	9.6 **(9.1)**	**3.9**	**12.6**	**7.7**	**41.9**	**104.2**
BFS5	10.7 (10.3)	2.2	5.6	7.4	40.0	-
	7.8 **(5.1)**	**4.0**	**11.4**	**7.0**	**38.7**	**6.7**
BFS6	4.9 (0)	1.1	8.7	9.7	64.6	-
	0	**0**	**0**	**0**	**0**	**0***
BFS7	0	0	0	0	0	-
	0	**0**	**0**	**0**	**0**	**0***
BFS8	15.2	2.5	16.8	12.9	82.4	-
	(14.8)	**3.7**	**26.3**	**13.9**	**86.2**	**795.1**

* zero effective porosity

Bibliography

Alhashmi, Z., Blunt, M. J., and Bijeljic, B. (2016). The Impact of Pore Structure Heterogeneity, Transport, and Reaction Conditions on FluidFluid Reaction Rate Studied on Images of Pore Space. *Transport in Porous Media*, 115(2):215–237.

Alimen, H. (1936). Etude sur le stampien du bassin de paris. *Geologique de France, Memoir*, 31.

Alpak, F. O., Berg, S., and Zacharoudiou, I. (2018). Prediction of fluid topology and relative permeability in imbibition in sandstone rock by direct numerical simulation. *Advances in Water Resources*, 122:49–59.

Alyafei, N. and Blunt, M. J. (2016). The effect of wettability on capillary trapping in carbonates. *Advances in Water Resources*, 90:36–50.

Andrew, M., Bijeljic, B., and Blunt, M. J. (2014). Pore-scale imaging of trapped supercritical carbon dioxide in sandstones and carbonates. *International Journal of Greenhouse Gas Control*, 22:1–14.

Bachu, S., Gunter, W., and Perkins, E. (1994). Aquifer disposal of co2: hydrodynamic and mineral trapping. *Energy Conversion and management*, 35(4):269–279.

Bakke, S., Øren, P.-E., et al. (1997). 3-d pore-scale modelling of sandstones and flow simulations in the pore networks. *Spe Journal*, 2(02):136–149.

Bauer, D., Youssef, S., Fleury, M., Bekri, S., Rosenberg, E., and Vizika, O. (2012). Improving the Estimations of Petrophysical Transport Behavior of Carbonate

Rocks Using a Dual Pore Network Approach Combined with Computed Microtomography. *Transport in Porous Media*, 94(2):505–524.

Berg, S., Rücker, M., Ott, H., Georgiadis, A., Van der Linde, H., Enzmann, F., Kersten, M., Armstrong, R., De With, S., Becker, J., et al. (2016). Connected pathway relative permeability from pore-scale imaging of imbibition. *Advances in Water Resources*, 90:24–35.

Bjørlykke, K., Nedkvitne, T., Ramm, M., and Saigal, G. C. (1992). Diagenetic processes in the brent group (middle jurassic) reservoirs of the north sea: an overview. *Geological Society, London, Special Publications*, 61(1):263–287.

Blunt, M. J. (2001). Flow in porous media - Pore-network models and multiphase flow. *Current Opinion in Colloid and Interface Science*, 6(3):197–207.

Blunt, M. J., Bijeljic, B., Dong, H., Gharbi, O., Iglauer, S., Mostaghimi, P., Paluszny, A., and Pentland, C. (2013). Pore-scale imaging and modelling. *Advances in Water Resources*, 51:197–216.

Boone, M. A., De Kock, T., Bultreys, T., De Schutter, G., Vontobel, P., Van Hoorebeke, L., and Cnudde, V. (2014). 3D Mapping of Water in Oolithic Limestone at Atmospheric and Vacuum Saturation using X-ray Micro-CT Differential Imaging. *Materials Characterization*, 97:150–160.

Bourbié, T. and Zinszner, B. (1985). Hydraulic and acoustic properties as a function of porosity in Fontainebleau Sandstone. *Journal of Geophysical Research*, 90(B13):11524–11532.

Buades, A., Coll, B., and Morel, J.-M. (2005). A non-local algorithm for image denoising. 2:60–65.

Buades, A., Coll, B., and Morel, J.-M. (2008). Nonlocal Image and Movie Denoising. *International Journal of Computer Vision*, 76(2):123–139.

Bultreys, T., De Boever, W., Brabant, L., and Cnudde, V. (2013). Comparison of pore network models for the investigation of fluid flow properties in building

stones. In *5th International conference on Porous Media & Annual meeting of the International Society for Porous Media (InterPore 2013)*. International Society for Porous Media (InterPore).

Bultreys, T., De Boever, W., and Cnudde, V. (2016a). Imaging and image-based fluid transport modeling at the pore scale in geological materials: A practical introduction to the current state-of-the-art. *Earth-Science Reviews*, 155:93–128.

Bultreys, T., Stappen, J. V., Kock, T. D., Boever, W. D., Boone, M. A., Hoorebeke, L. V., and Cnudde, V. (2016b). Investigating the Relative Permeability Behavior of Microporosity-Rich Carbonates and Tight Sandstones with Multiscale Pore Network Models. *Journal of Geophysical Research: Solid Earth*, 121(11):7929–7945.

Bultreys, T., Van Hoorebeke, L., and Cnudde, V. (2015). Multi-scale, micro-computed tomography-based pore network models to simulate drainage in heterogeneous rocks. *Advances in Water Resources*, 78:36–49.

Chadwick, R., Zweigel, P., Gregersen, U., Kirby, G., Holloway, S., and Johannessen, P. (2004). Geological reservoir characterization of a co2 storage site: The utsira sand, sleipner, northern north sea. *Energy*, 29(9-10):1371–1381.

Churcher, P., French, P., Shaw, J., Schramm, L., et al. (1991). Rock properties of berea sandstone, baker dolomite, and indiana limestone. In *SPE International Symposium on Oilfield Chemistry*. Society of Petroleum Engineers.

Cnudde, V. and Boone, M. N. (2013). High-resolution X-ray Computed Tomography in Geosciences: A Review of the Current Technology and Applications. *Earth-Science Reviews*, 123:1–17.

De Jager, J. and Geluk, M. (2007). Petroleum geology. *Geology of the Netherlands. Royal Netherlands Academy of Arts and Sciences, Amsterdam*, 241:264.

De Muynck, W., Leuridan, S., Van Loo, D., Verbeken, K., Cnudde, V., De Belie, N., and Verstraete, W. (2011). Influence of pore structure on the effectiveness of a

biogenic carbonate surface treatment for limestone conservation. *Appl. Environ. Microbiol.*, 77(19):6808–6820.

Derluyn, H., Dewanckele, J., Boone, M. N., Cnudde, V., Derome, D., and Carmeliet, J. (2014). Crystallization of hydrated and anhydrous salts in porous limestone resolved by synchrotron X-ray microtomography. *Nuclear Instruments and Methods in Physics Research, Section B: Beam Interactions with Materials and Atoms*, 324:102–112.

Doyen, P. M. (1988). Permeability, conductivity, and pore geometry of sandstone. *Journal of Geophysical Research*, 93(B7):7729.

Dubelaar, C. W. and Nijland, T. G. (2015). The bentheim sandstone: geology, petrophysics, varieties and its use as dimension stone. In *Engineering Geology for Society and Territory-Volume 8*, pages 557–563. Springer.

Dubelaar, C. W. and Nijland, T. G. (2016). Early cretaceous obernkirchen and bentheim sandstones from germany used as dimension stone in the netherlands: geology, physical properties, architectural use and comparative weathering. *Geological Society, London, Special Publications*, 416(1):163–181.

Dutton, S. P. and Loucks, R. G. (2010). Diagenetic controls on evolution of porosity and permeability in lower Tertiary Wilcox sandstones from shallow to ultradeep (200-6700 m) burial, Gulf of Mexico Basin, U.S.A. *Marine and Petroleum Geology*, 27(1):69–81.

Ells, G. and Division, M. G. S. (1979). *The Mississippian and Pennsylvanian (Carboniferous) Systems in the United States, Michigan: Historical Review and Summary of Areal, Stratigraphic, Structural, and Economic Geology of Mississippian and Pennsylvanian Rocks in Michigan*. Geological Survey professional paper. U.S. Government Printing Office.

Fredrich, J., Greaves, K., and Martin, J. (1993). Pore geometry and transport properties of fontainebleau sandstone. *International Journal of Rock Mechanics and Mining Sciences & Geomechanics Abstracts*, 30(7):691 – 697.

Füchtbauer, H. (1963). Paleogeography and reservoir properties of the lower cretaceous bentheim sandstone. In *Excursion Guide Book I, 6th World Petroleum Congress*, pages 42–43.

Furre, A.-K., Eiken, O., Alnes, H., Vevatne, J. N., and Kiær, A. F. (2017). 20 years of monitoring co2-injection at sleipner. *Energy procedia*, 114:3916–3926.

Gao, Y., Lin, Q., Bijeljic, B., and Blunt, M. J. (2017). X-ray microtomography of intermittency in multiphase flow at steady state using a differential imaging method. *Water resources research*, 53(12):10274–10292.

Garland, C. (1993). Miller field: reservoir stratigraphy and its impact on development. In *Geological Society, London, Petroleum Geology Conference series*, volume 4, pages 401–414. Geological Society of London.

Ghanbarzadeh, S., Hesse, M. a., and Prodanović, M. (2015). A level set method for materials with texturally equilibrated pores. *Journal of Computational Physics*, 297:480–494.

Giles, M., Stevenson, S., Martin, S., Cannon, S., Hamilton, P., Marshall, J., and Samways, G. (1992). The reservoir properties and diagenesis of the brent group: a regional perspective. *Geological Society, London, Special Publications*, 61(1):289–327.

Gluyas, J. and Coleman, M. (1992). Material flux and porosity changes during sediment diagenesis. *Nature*, 356(6364):52–54.

Gluyas, J., Garland, C., Oxtoby, N., Hogg, A., Worden, R., and Morad, S. (2000). Quartz cement: the miller's tale. *Special publication-international association of sedimentologists*, 29:199–218.

Gomez, C. T., Dvorkin, J., and Vanorio, T. (2010). Laboratory Measurements of Porosity, Permeability, Resistivity, and Velocity on Fontainebleau Sandstones. *Geophysics*, 75(6):E191.

Hannibal, J. T. (2020). Berea sandstone: A heritage stone of international significance from Ohio, USA. *Geological Society, London, Special Publications*, 486.

Haszeldine, R., Quinn, O., England, G., Wilkinson, M., Shipton, Z., Evans, J. P., Heath, J., Crossey, L., Ballentine, C., and Graham, C. (2005). Natural geochemical analogues for carbon dioxide storage in deep geological porous reservoirs, a united kingdom perspective. *Oil & gas science and technology*, 60(1):33–49.

Holloway, S., Vincent, C. J., Bentham, M. S., and Kirk, K. L. (2006). Top-down and bottom-up estimates of co2 storage capacity in the united kingdom sector of the southern north sea basin. *Environmental Geosciences*, 13(2):71–84.

Iassonov, P., Gebrenegus, T., and Tuller, M. (2009). Segmentation of x-ray computed tomography images of porous materials: A crucial step for characterization and quantitative analysis of pore structures. *Water Resources Research*, 45(9).

Ketcham, R. A. and Carlson, W. D. (2001). Acquisition, optimization and interpretation of x-ray computed tomographic imagery: applications to the geosciences. *Computers & Geosciences*, 27(4):381 – 400.

Lindquist, W. B., Venkatarangan, A., Dunsmuir, J., and Wong, T.-f. (2000). Pore and throat size distributions measured from synchrotron x-ray tomographic images of fontainebleau sandstones. *Journal of Geophysical Research: Solid Earth*, 105(B9):21509–21527.

Lu, J., Wilkinson, M., Haszeldine, R. S., and Boyce, A. J. (2011). Carbonate cements in miller field of the uk north sea: a natural analog for mineral trapping in co 2 geological storage. *Environmental Earth Sciences*, 62(3):507–517.

Lu, J., Wilkinson, M., Haszeldine, R. S., and Fallick, A. E. (2009). Long-term performance of a mudrock seal in natural co2 storage. *Geology*, 37(1):35–38.

Madonna, C., Quintal, B., Frehner, M., Almqvist, B. S. G., Tisato, N., Pistone, M., Marone, F., and Saenger, E. H. (2013). Synchrotron-Based X-ray Tomographic Microscopy for Rock Physics Investigations. *Geophysics*, 78(1):D53–D64.

Marcussen, Ø., Maast, T. E., Mondol, N. H., Jahren, J., and Bjørlykke, K. (2010). Changes in physical properties of a reservoir sandstone as a function of burial depth–the etive formation, northern north sea. *Marine and Petroleum Geology*, 27(8):1725–1735.

Mavko, G. and Nur, A. (1997). The Effect of a Percolation Threshold in the Kozeny-Carman Relation Gary Mavko and Amos Nur . *Geophysics*, 62(5):1480–1482.

McBride, E. F. and EF, M. (1977). Secondary porosity-importance in sandstone reservoirs in texas. *Gulf coast association of geological societies. Annual meeting*, pages 121–122.

Meakin, P. and Tartakovsky, A. (2009). Modeling and simulation of pore-scale multiphase fluid flow and reactive transport in fractured and porous media. *Reviews of Geophysics*, 47(3):1–47.

Mehmani, A., Milliken, K., and Prodanović, M. (2019). Predicting flow properties in diagenetically-altered media with multi-scale process-based modeling: A wilcox formation case study. *Marine and Petroleum Geology*, 100:179–194.

Mehmani, A. and Prodanović, M. (2014). The Effect of Microporosity on Transport Properties in Porous Media. *Advances in Water Resources*, 63:104–119.

Mehmani, A., Prodanović, M., and Milliken, K. (2015). A quantitative pore-scale investigation on the paragenesis of wilcox tight gas sandstone. pages 2511–2517.

Mørk, A., Dallmann, W., Dypvik, H., Johannessen, E., Larssen, G., Nagy, J., Nøttvedt, A., Olaussen, S., Pchelina, T., and Worsley, D. (1999). Mesozoic lithostratigraphy. *Lithostratigraphic lexicon of Svalbard. Upper Palaeozoic to Quaternary bedrock. Review and recommendations for nomenclature use*, pages 127–214.

Øren, P.-E. and Bakke, S. (2003). Reconstruction of berea sandstone and pore-scale modelling of wettability effects. *Journal of Petroleum Science and Engineering*, 39(3-4):177–199.

Otsu, N. (1979). A threshold selection method from gray-level histograms. *IEEE Transactions on Systems, Man, and Cybernetics*, 9(1):62–66.

Paxton, S., Szabo, J., Ajdukiewicz, J., and Klimentidis, R. (2002). Construction of an intergranular volume compaction curve for evaluating and predicting compaction and porosity loss in rigid-grain sandstone reservoirs. *AAPG bulletin*, 86(12):2047–2067.

Peksa, A. E., Wolf, K.-H. A., and Zitha, P. L. (2015). Bentheimer sandstone revisited for experimental purposes. *Marine and Petroleum Geology*, 67:701–719.

Pittman, E. D. (1979). Porosity diagenesis and productive capability of sandstone reservoirs. *Special Publications of SEPM*, pages 159–173.

Prodanović, M., Mehmani, A., and Sheppard, A. P. (2014). Imaged-based multiscale network modelling of microporosity in carbonates. *Geological Society, London, Special Publications*, 406:SP406–9.

Revil, A., Kessouri, P., and Torres-Verdín, C. (2014). Electrical conductivity, induced polarization, and permeability of the Fontainebleau sandstone. *Geophysics*, 79(5):D301–D318.

Rhodes, M. E., Bijeljic, B., and Blunt, M. J. (2008). Pore-to-field simulation of single-phase transport using continuous time random walks. *Advances in Water Resources*, 31(12):1527–1539.

Ridler, T. and Calvard, S. (1978). Picture Thresholding Using. *IEEE Transactions on Systems, Man and Cybernetics*, smc-8(8):630–632.

Rismyhr, B., Bjærke, T., Olaussen, S., Mulrooney, M. J., and Senger, K. (2019). Facies, palynostratigraphy and sequence stratigraphy of the wilhelmøya subgroup (upper triassic–middle jurassic) in western central spitsbergen, svalbard. *Geological Society of Norway*, 99(4):35–64.

Roels, S., Elsen, J., Carmeliet, J., and Hens, H. (2001). Characterisation of pore structure by combining mercury porosimetry and micrography. *Materials and structures*, 34(2):76–82.

Rooksby, S. (1991). The miller field, blocks 16/7b, 16/8b, uk north sea. *Geological Society, London, Memoirs*, 14(1):159–164.

Rücker, M., Berg, S., Armstrong, R., Georgiadis, A., Ott, H., Schwing, A., Neiteler, R., Brussee, N., Makurat, A., Leu, L., et al. (2015). From connected pathway flow to ganglion dynamics. *Geophysical Research Letters*, 42(10):3888–3894.

Santarelli, F. J. and Brown, E. T. (1989). Failure of three sedimentary rocks in triaxial and hollow cylinder compression tests. *International Journal of Rock Mechanics and Mining Sciences and*, 26(5):401–413.

Schlter, S., Sheppard, A., Brown, K., and Wildenschild, D. (2014). Image processing of multiphase images obtained via x-ray microtomography: A review. *Water Resources Research*, 50(4):3615–3639.

Schmidt, V. and McDonald, D. A. (1979). The role of secondary porosity in the course of sandstone diagenesis. *Special Publications of SEPM*, 26:175–207.

Scholle, P. A. and Ulmer-Scholle, D. S. (2003). *A Color Guide to the Petrography of Carbonate Rocks: Grains, Textures, Porosity, Diagenesis, AAPG Memoir 77*, volume 77. AAPG.

Sezgin, M. and Sankur, B. (2004). Survey over image thresholding techniques and quantitative performance evaluation. *Journal of Electronic imaging*, 13(1):146–166.

Shah, S., Gray, F., Crawshaw, J., and Boek, E. (2016). Micro-computed tomography pore-scale study of flow in porous media: Effect of voxel resolution. *Advances in water resources*, 95:276–287.

Soulaine, C., Gjetvaj, F., Garing, C., Roman, S., Russian, A., Gouze, P., and Tchelepi, H. A. (2016). The impact of sub-resolution porosity of x-ray microtomography images on the permeability. *Transport in Porous Media*, 113(1):227–243.

Stampanoni, M., Groso, A., Isenegger, A., Mikuljan, G., Chen, Q., Bertrand, A., Henein, S., Betemps, R., Frommherz, U., Bhler, P., Meister, D., Lange, M., and Abela, R. (2006). Trends in synchrotron-based tomographic imaging: the SLS experience. *SPIE*, 6318:193 – 206.

Thomson, P.-R., Aituar-Zhakupova, A., and Hier-Majumder, S. (2018). Image Segmentation and Analysis of Pore Network Geometry in Two Natural Sandstones. *Frontiers in Earth Sciences*, 6(June):1–14.

Thomson, P.-R., Jefferd, M., Clark, B. L., Chiarella, D., Mitchell, T., and Hier-Majumder, S. (2020). Pore network analysis of brae formation sandstone, north sea. *Marine and Petroleum Geology – under review*.

Turner, B. R., Younger, P. L., and Fordham, C. E. (1993). Fell Sandstone Group lithostratigraphy south-west of Berwick-upon-Tweed: Implications for the regional development of the Fell Sandstone. *Proceedings of the Yorkshire Geological Society*, 49(4):269–281.

Valvatne, P. H. and Blunt, M. J. (2004). Predictive pore-scale modeling of two-phase flow in mixed wet media. *Water Resources Research*, 40(7).

Van Stappen, J., De Kock, T., Boone, M., Olaussen, S., and Cnudde, V. (2014). Pore-scale characterization and modelling of co2 flow in tight sandstones using x-ray micro-ct; knorringfjellet formation of the longyearbyen co2 lab, svalbard. *Norwegian Journal of Geology*, 94(2-3):201–215.

von Bargen, N. and Waff, H. (1986). Permeabilities, interfacial areas and curvatures of partially molten systems: results of numerical computations of equilibrium microstructures. *Journal of Geophysical Research*, 91:9261–9276.

Wildenschild, D. and Sheppard, A. P. (2013). X-ray Imaging and Analysis Techniques for Quantifying Pore-Scale Structure and Processes in Subsurface Porous Medium Systems. *Advances in Water Resources*, 51:217–246.

Wildenschild, D., Vaz, C., Rivers, M., Rikard, D., and Christensen, B. (2002). Using x-ray computed tomography in hydrology: Systems, resolutions, and limitations. *Journal of Hydrology*, 267(3-4):285–297.

Wimert, J. T. and Hier-Majumder, S. (2012). A three-dimensional microgeodynamic model of melt geometry in the earth's deep interior. *Journal of Geophysical Research-Solid Earth*, 117(B04):B04203.

Youssef, S., Han, M., Bauer, D., Rosenberg, E., Bekri, S., Fleury, M., and Vizika, O. (2008). High resolution μ-ct combined to numerical models to assess electrical properties of bimodal carbonates. In *International Symposium of Core Analysts*, pages 1–12.

Youssef, S., Rosenberg, E., Gland, N., Kenter, J., Skalinski, M., and Vizika, O. (2007). High resolution CT and pore-network models to assess petrophyscial properties of homogeneous and heterogeneous carbonates. *PE/EAGE Reservoir Characterization and Simulation Conference*, page 12.